Molybdenum Disulphide (MoS_2) Nanosheet Inks Evaluated for Printed Electronics and Application to Thin-Film Transistors

by

Leon Mintz

A thesis

presented to the University of Waterloo

in fulfilment of the

thesis requirements for the degree of

Master of Applied Science

in

Electrical & Computer Engineering (Nanotechnology)

Waterloo, Ontario, Canada, 2017

Author's declaration

I hereby declare that I am the sole author of this thesis. This is a true copy of the thesis, including any required final revisions, as accepted by my examiners.

I understand that my thesis may be made electronically available to the public.

Abstract

Inkjet printing is a versatile deposition technique that has been used for the fabrication of electronic circuits, from simple conductive tracks to complete 3D logic circuits. The emergence of solution-processable 2D layered materials pushes the performance boundaries of printed devices. The use of 2D functional materials combined with the growing knowledge in the field of inkjet printing processing has great potential for competing with traditional fabrication methods in terms of performance and cost. Molybdenum disulphide (MoS_2) is the most researched 2D semiconductor owing to its tunable bandgap, high mobility and photo-responsivity and mechanical flexibility. Solution-processable MoS_2 is needed for large-scale device fabrication. Unlike large MoS_2 sheets, nano-scale sheets can be easily stabilized in suspension and used in various deposition methods. However, nanosheet MoS_2 suspensions were used so far to fabricate two-terminal devices, with limited or no results for thin-film transistors.

In this research, a significant first step was taken in studying the behaviour of MoS_2 nanosheet suspensions through the introduction of ethyl cellulose as a stabilizing agent and the modification of substrate temperature and surface energy via hydrophobic coatings of the target substrates for improved printability and film formation. For the first time, it was shown that the ring-stain effect can be directly exploited for the fabrication of circular devices using inkjet printing. Minimal suspension concentration of 3.7 $\frac{mg}{L}$ was evaluated for the first time by a continuum percolation simulation using real particle size distribution. Stability of MoS_2 nanosheets under thermal treatment was studied for the first time and a decomposition temperature of 200°C in air and 300°C is inert atmosphere was determined. It was shown that thick films exhibit bulk conductivity but no field-effect was observed.

In conclusion, the minimal concentration evaluation and the results of the thermal stability study imposed limitations on process development, which were addressed during device fabrication. Top-contact device architecture was shown to be superior to bottom-contact device architecture. The absence of an observable field-effect was attributed to poor inter-sheet charge transport.

Acknowledgements

I would like to express my gratitude to my supervisor, Professor William Wong, for his support, advice, patience, and most of all for his desire to teach and for sharing his invaluable perspective on success and failure in research. Thank you so much Professor Wong for the unique opportunities you granted and advised me through – thank you for guiding me through the far from straightforward challenge of conducting scientific research.

I would like to thank my colleagues at the Advanced Flexible Electronics Technology (AFET) group for the joyful time we spent together, for their illuminating advice, their willingness to help, and for responding to the text messages they received in the middle of the night. Special thanks to Lina Voloshin and Melissa Chow for welcoming me into the printing team and for training me in operating the printer – it was priceless. Thanks to Pranav Gavirneni, Ali Tari, Mohsen Asad and Qing Li for their willingness and time they spent helping me.

I would like to express my gratitude and appreciation to all the daily and nightly dwellers of the Giga-to-Nanoelectronics (G2N) Lab in the past and present for the training and support they provided during my research. Special thanks to Dr. Czang-Ho Lee and Richard Barber for their infinite patience, for sharing their valued experience with me and for their open door, through which I walked many times.

This research would not have been complete without the help of Nicholas Lanigan, who introduced me to DLS and TGA, and provided great help with ink synthesis, and Dilara Yilman, who enlightened me with the power of freeze-drying and spray-coating.

To my partner Annie, thank you for reading every word, written and non-written.

Last but not least, special thanks to all my Kismet[1] companions.

I dedicate this thesis to my family, near and far, for their unconditional support that motivated and encouraged me. Amba and apple cake will always have a special meaning for me.

[1] *n.* fate; fortune.

Table of Contents

List of Figures

List of Tables

List of Abbreviations

CRE Coffee-ring effect

CVD Chemical-vapour deposition

DLS Dynamic light scattering

DMF Dimethylformamide

DMSO Dimethyl sulfoxide

EC Ethyl cellulose

HMDS Hexamethyldisilazane

IJP Inkjet printing

MoS_2 Molybdenum disulfide

MSJ Metal-semiconductor junction

NMP N-methyl-2-pyrrolidone

SB Schottky barrier

SiO_2 Silicon oxide

TFT Thin-film transistor

TGA Thermogravimetric analysis

THF Tetrahydrofuran

TMDC Transition-metal dichalcogenide

"An experiment is never a failure solely because it fails to achieve predicted results. An experiment is a failure only when it also fails adequately to test the hypothesis in question, when the data it produces don't prove anything one way or another."

Robert M. Pirsig, "*Zen and the Art of Motorcycle Maintenance*"

Part I

Introduction

In this thesis, a significant first step was taken in studying the behaviour of molybdenum disulphide (MoS_2) nanosheet suspensions, which were used for device fabrication via drop-casting and inkjet printing. Aqueous suspensions of MoS_2 were formulated and modified for consistent droplet generation and film formation. The importance of studying the thermal stability of MoS_2 nanosheets for process development was demonstrated. Through the modification of physical properties of the MoS_2 suspensions, as well as the substrate surface energy, improved film formation was obtained in both drop-casted and inkjet printed devices. A mask design dedicated for electrical characterization of printed films was developed and bottom-contact and top-contact thin-film transistor (TFT) structures were studied.

The base hypothesis of this work was that a percolating network of MoS_2 nanosheets can be deposited using printing and exhibit semiconducting behaviour across micrometer scale, similar to the semiconducting behaviour of a single crystal microscale sheet. This research shows that the ring-stain effect can be directly exploited for the fabrication of circular devices using inkjet printing and that spray coating is a promising deposition method for large-area substrates, which eliminates the undesired ring-stain phenomena.

While conductive channels were successfully obtained, no field-effect switching behaviour in the presence of gate bias was observed. After many experiments, it became apparent that percolation networks of semiconducting nodes do not exhibit semiconducting properties at the film thicknesses studied. The onset of bulk conductivity demonstrated that semiconductivity of percolating nanosheets does not scale in the same sense that conducting percolating networks do. The absence of a field-effect was observed in both extremely thin films and thick films. An in-depth study of electrical properties as a function of film thickness is subject to future research.

The work described in this thesis is the first attempt of fabricating and characterizing nanosheet-based devices with microscale-long channels of percolating networks of sub-100 nm nanosheets. This report demonstrates that it is possible to coat large-area substrates with solution-processable MoS_2 and that printed MoS_2 films are continuous and conductive. Switching behaviour, however, was not observed.

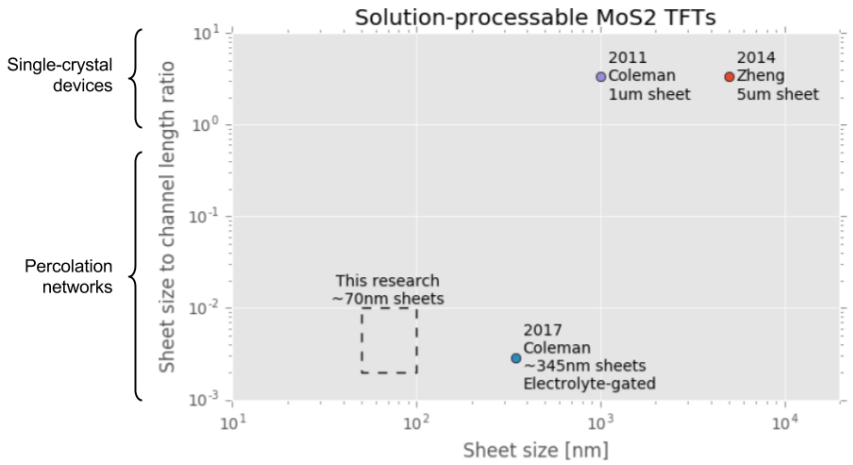

Figure 1: Focus of this research in terms of sheet dimensions. The references on the graph are all published works on solution-processable MoS_2 TFTs. The very recent publication by Coleman *et al.* [1] is focused on electrolyte-gated TFTs, which are fundamentally different that attempted in this research.

I.1 Thin-film transistors

Thin-film transistors (TFTs) are field-effect transistors (FETs) whose semiconductor, dielectric layer and metallic contacts can be deposited on various insulating substrates in a variety of architectures (Figure 2).

In such devices, the drain current I_D changes with the drain voltage V_D and the gate voltage V_G, depending on the operation mode of the device, namely linear and saturation, as follows:

$$I_D = \begin{cases} \frac{W}{L} C\mu \left(V_G - V_T - \frac{V_D}{2}\right) V_D, & V_D \leq V_G - V_T \quad \text{(linear)} \\ \frac{W}{2L} C\mu \left(V_G - V_T\right)^2 & V_D > V_G - V_T \quad \text{(saturation)} \end{cases} \tag{1}$$

where $\frac{W}{L}$ is the width-to-length ratio of the channel, C is the capacitance per unit area of the insulator, μ is the mobility of the semiconductor and V_T is the threshold voltage of the device, which depends on the semiconductor material and its interface with the insulator. In the linear regime, also known as the ohmic mode, the drain current increases linearly with the gate voltage, and in the saturation regime the drain current has a quadratic dependance on the gate voltage and is independent of the drain voltage. Therefore, the current flow from source to drain through the channel of the transistor can be turned on or off simply by changing the gate potential.

The semiconductor is the component on which the switching behaviour of a transistor is based and therefore its intrinsic properties and its interfaces with the gate insulator and metal contacts are the most important factors in transistor design. The large range of semiconducting materials that can be used for TFT fabrication differentiates them from conventional transistors that mostly rely on crystalline

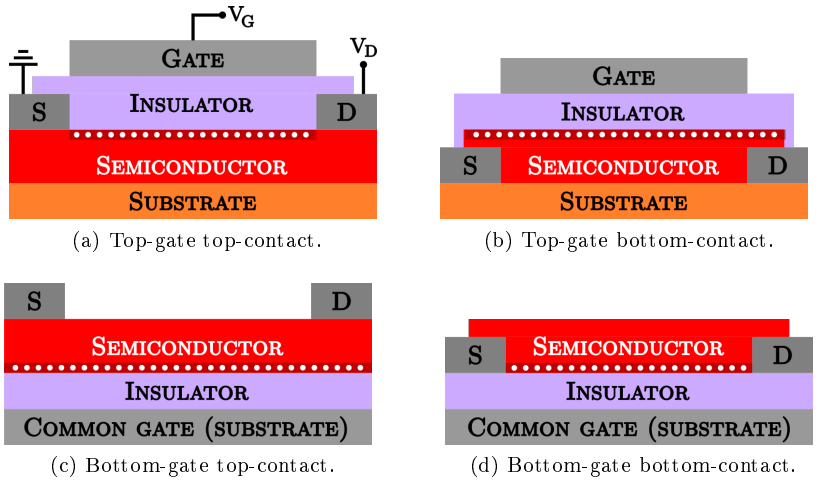

(a) Top-gate top-contact.

(b) Top-gate bottom-contact.

(c) Bottom-gate top-contact.

(d) Bottom-gate bottom-contact.

Figure 2: The four typical architectures of thin-film transistors. The white dots inside the semiconductor layer represent the conductive channel formed by applying a bias to the gate electrode; S and D represent the source and drain electrodes, respectively.

compounds from Group 12 to 16 (Si, SiC, Ge, GaAs, etc.).[2]

While traditional high-temperature vacuum processes with crystalline materials offer a remarkable solution for high packing density, high performance devices and low cost per transistor, they are not a good fit for large-area fabrications due to the size limit of the substrates and the high cost per unit area.

The most popular semiconducting material in commercial TFTs is amorphous silicon, which can be deposited at temperatures as low as $100-300\,^{\circ}\mathrm{C}$ [11,12]. However, amorphous silicon has a relatively low field-effect mobility and the deposition of amorphous silicon on temperature sensitive materials introduces strain due to mismatch in the thermal expansion coefficient [13]. Other semiconductors, with higher electronic performance, that are not limited to vacuum chamber deposition and that can be deposited at room temperature, are of interest [14]. In general, solution-processable materials agree with all of these requirements [15]. An emerging class of high-performance solution-processable materials is 2D layered materials [16,17].

[2]IUPAC notation; in CAS notation these groups are numbered IIB, IIIA, IVA, VA and VIA.

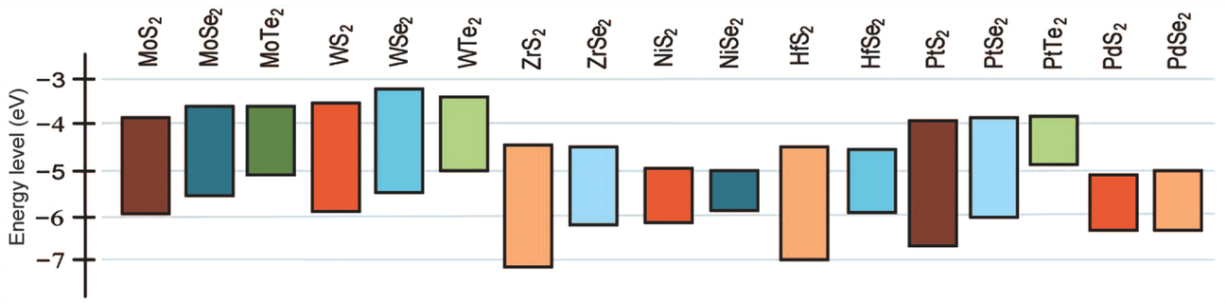

Figure 3: Bandgap diagrams for various single layer TMDCs [2]. © 2015 WILEY-VCH Verlag GmbH & Co. KGaA, Weinheim.

I.2 2D layered materials

The two most popular layered material precursors for device fabrication are graphite and transition-metal dichalcogenides (TMDCs). TMDCs are layered 2D materials, similar to graphite, which can be thinned down to single layers, similar to graphene. TMDCs have the general formula MX_2 where M is a transition metal from group IV (Ti, Zr, etc.), V (V, Nb, etc.) or VI (Cr, Mo, etc.), and X is a chalcogen (S, Se or Te) [3]. Each layer in a TMDC structure consists of three hexagonally packed and covalently bonded sub-layers, namely a metal layer (M) sandwiched by two chalcogen layers (X). Layers are held together by weak Van der Waals forces and the ability to separate layered materials into single- or few-layer sheets can enable the fabrication of versatile 2D electronic devices with a potential for large-scale production. 2D layered materials can be used to make electrodes from semi-metals such as graphene, tungsten ditelluride (WTe_2) and titanium diselenide ($TiSe_2$); dielectric layers from insulators such as boron nitride (h-BN) and hafnium disulphide (HfS_2); and active channels from semiconductors such as molybdenum disulphide (MoS_2), tungsten disulphide (WS_2) and tungsten diselenide (WSe_2) (Figure 3).

This thesis focuses on molybdenum disulphide (MoS_2), the most researched TMDC and the second most researched 2D material after graphene.

I.2.1 Structure of MoS_2

MoS_2 is made of 2D layers of a hexagonally structured network of molybdenum (Mo) and sulphur (S) atoms, covalently bonded to each other. In each layer, every Mo atom is bonded to six S atoms and each S atom is bonded to three Mo atoms. The MoS_2 layers are stacked together due to a weak Van der Waals force between the sheets of 200 meV per unit-cell [3].

Unlike graphene, where the band gap is zero, in MoS_2, as the number of layers increases from 1 to 8 (bulk), the bandgap of MoS_2 changes from 1.8 eV (direct) to 1.3 eV (indirect). The presence of a band gap is crucial for fabricating active devices such as field-effect transistors and optical detectors. MoS_2 is

Table 1: MoS_2 structural polytypes and their properties ($a \sim 3.1-3.7$ Å; interlayer spacing is ~ 6.5 Å) [10] (Copyright © 2012, Rights Managed by Nature Publishing Group). 2H has been observed to transform to 1T after electron beam irradiation or Li intercalation; 1T has been observed to transform to 2H after a brief 200°C bake.

	2H-MoS_2	**1T-MoS_2**	**3R-MoS_2**
Layers per unit cell	2	1	3
Symmetry	hexagonal	tetragonal	rhombohedral
Metal coordination	trigonal prismatic (D3h)	octahedral (Oh)	trigonal prismatic (D3h)
Class	semiconducting	metallic	
Schematic	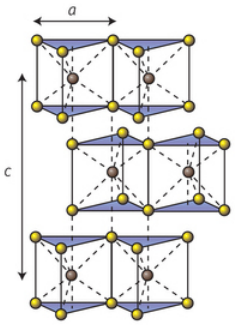	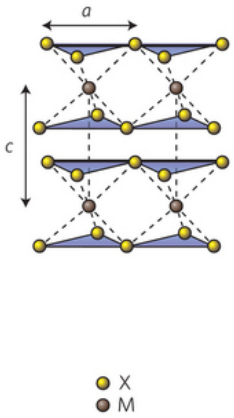	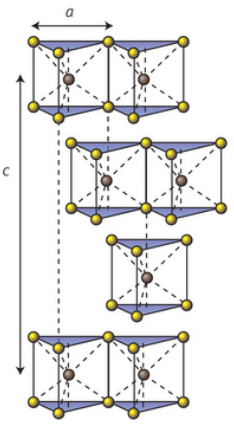

an n-type material with electron carrier concentration of $n_0 = 10^{12} - 10^{13}\,\mathrm{cm}^{-2}$ [18, 19].[3]

MoS_2 can take one of several structural polytypes (Table 1): 2H (hexagonal symmetry with 2 layers per unit-cell), 1T (tetragonal symmetry with 1 layer per unit-cell) and 3R (rhombohedral symmetry with 3 layers per unit-cell) but for electronic applications the semiconducting 2H-MoS_2 is the desired form.

The mechanism of transition between 2H and 1T phases is gliding of Mo or S planes relative to each other [20]. Chemically exfoliated MoS_2 via intercalation contains a mixture of 2H and 1T phases [21]. In-plane mechanical strain in monolayers and bilayer MoS_2, as well as reduced layer separation in bilayer MoS_2, are known to cause metallic transition. The 1T phase can be relaxed to 2H phase via annealing at temperatures of up to 300°C [22].

I.2.2 Structural characterization

Molecular vibrations can provide structural information about the measured sample. The most direct way to probe vibrational states in molecules is via photonic excitation, such as infrared (IR) spectroscopy or Raman spectroscopy. MoS_2 has both IR- and Raman-active modes (Figure 4). Raman spectroscopy is the

[3] Using an interlayer spacing of 6.5 Å, this is equivalent to $\sim 10^{19} - 10^{20}\,\mathrm{cm}^{-3}$, however, in-plane charge transport is more efficient than out-of-plane charge transport, such that cm^{-2} is the more correct unit to use for layered materials.

standard method for characterizing MoS_2 due to the strong Raman shift exhibited by MoS_2 and because Raman spectroscopy allows convenient in-situ characterization without any sample preparation.

To measure a sample, a 633 nm laser beam is typically focused with a microscope to a spot size of a few micrometers. The laser light is inelastically scattered by the sample, emerging with a lower frequency equivalent to the vibrational energy quanta retained by the molecules in the sample [23]. The shift in the frequencies of the emerging photons correspond to the vibrational modes of the system (Figure 4). The intensities of the various shifts comprises the Raman spectrum. The frequency shift Δw, more commonly called the Raman shift, is measured in wavenumbers,

$$\Delta w = \frac{1}{\lambda_{\text{exc}}} - \frac{1}{\lambda_{\text{meas}}}, \tag{2}$$

where λ_{exc} is the excitation wavelength and λ_{meas} is the measured wavelength of the scattered emission. Vibrational modes have wavenumbers in the range 300-3000 cm^{-1} and the widely used characteristic peaks of MoS_2 are approximately 380-385 cm^{-1} (for E^1_{2g}) and 403-407 cm^{-1} (for A_{1g}), as presented in Table 2.

It was also shown theoretically and experimentally that the position of specifically the Raman-active E^1_{2g} and A_{1g} are highly sensitive to the sheet thickness [3]. The Raman shift frequency of these modes depends on the sheet thickness and exhibit an opposite trend as a function of number of layers (Table 2). The exact values depend on the Raman laser excitation frequency. In this thesis, Raman spectroscopy with excitation frequency of 633 nm is used to confirm the presence of MoS_2 as well as determining its thickness.

The characteristic Raman peaks are also useful for confirming MoS_2 integrity after harsh processing, such as annealing at high temperature (Sections II.2.2, II.2.4). In some publications, Raman mappings of areas over $100\,\mu m^2$ are presented as evidence for MoS_2 presence, film homogeneity or for film density (porosity) calculations [1]. In such mappings, the Raman shift intensity spectrum is integrated along the Raman-active region to capture the characteristic peaks for every rastered point on the sample [4].

I.2.3 Mechanical exfoliation of MoS_2

Various methods have been successfully used for the synthesis of MoS_2, such as exfoliation via alkali metal intercalation [24], exfoliation in organic solvents, physical vapour deposition, hydrothermal synthesis, electrochemical synthesis, sulphurisation of molybdenum oxides, and thermolysis of precursors containing Mo and S [25]. However, mechanical exfoliation (Figure 5) using the scotch-tape method is the easiest and the most popular method for obtaining high-quality, thin, microscale sheets on arbitrary substrates; and, it is still the best approach for studying fundamental optoelectronic properties of MoS_2.

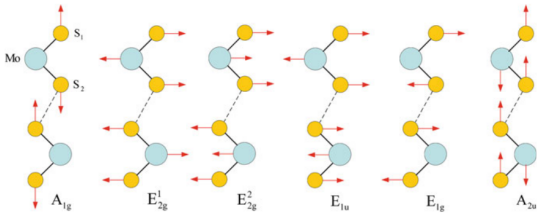

Figure 4: Raman active (A_{1g}, E^1_{2g}, E^2_{2g}, E_{1g}) and infrared active (E_{1u}, E_{2u}) vibration modes in MoS_2 [3]. Copyright © 2014, Springer International Publishing Switzerland.

Table 2: Raman shift (cm^{-1}) of in-plane E^1_{2g} and out-of-plane A_{1g} vibrations, as a function of number of layers in crystalline MoS_2 (633 nm laser) [3].

Thickness	E^1_{2g}	A_{1g}	Δw
1L	385.0	403.8	18.8
2L	383.8	404.8	21.0
3L	383.3	405.0	21.7
4L	382.9	406.0	23.1
Bulk	381.5	406.6	25.1

A mobility of $200\,cm^2V^{-1}cm^{-1}$ and on/off ratio of 10^8 were demonstrated with a mechanically exfoliated monolayer MoS_2 device using hafnium oxide gate dielectric [26]. Such high performing devices are suitable for a wide range of applications.

However, the yield of large mechanically exfoliated sheets is low and their positioning is random, which imposes significant challenges on large-scale fabrication. Moreover, achievable sheet size reduces with the thickness of the sheet, with typical mechanically exfoliated mono- or few-layer sheet areas in the range of $25 - 200\,\mu m^2$ – an area that could be sufficient for fabricating only a few devices side to side at most. A synthesis method that is based on liquid-phase exfoliated nanosheets, a material that is significantly easier to synthesize and deposit, is described in Section I.2.5.

I.2.4 Optical identification of MoS_2 sheets

MoS_2 sheets on silicon oxide (SiO_2) substrate exhibit a range of colours (Figure 5c), depending on the sheet thickness, which facilitates their quick identification. The optical contrast[4] of MoS_2 nanolayers on SiO_2 substrate depends on the substrate thickness and the wavelength of illuminating light [28]; hence, it is helpful to use specific oxide thickness for maximal contrast (75 nm and 250 nm oxide thickness produce the highest contrast across a large wavelength range). This property of MoS_2 is advantageous for rapid process development, which would otherwise require identification of MoS_2 using AFM or Raman.

The visibility of MoS_2 in SiO_2 is not limited to microscale mechanically exfoliated sheets; even miniscule amounts of MoS_2 nanosheets cause an optically detectable change in the colouring of the substrate.

[4]Contrast is a dimensionless quantity. Benameur *et al.* [28] defined it in this case as the relative intensity of reflected light from MoS_2, compared to a bare substrate, $C = \frac{R(n=1)-R(n_{MoS_2})}{R(n=1)}$.

(a) Picture of bulk MoS_2. Credit: Materialscientist at English Wikipedia [CC BY-SA 3.0 or GFDL], via Wikimedia Commons.

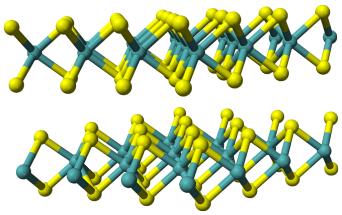

(b) Ball-and-stick model of MoS_2. Credit: By Ben Mills (Own work) [Public domain], via Wikimedia Commons.

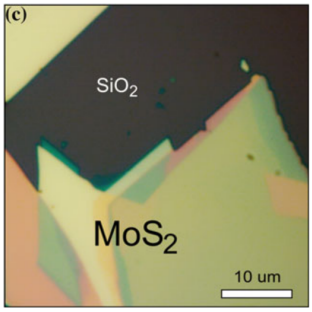

(c) Visibility of mechanically exfoliated MoS_2 on SiO_2 with various thicknesses [3]. Copyright © 2014, Springer International Publishing Switzerland.

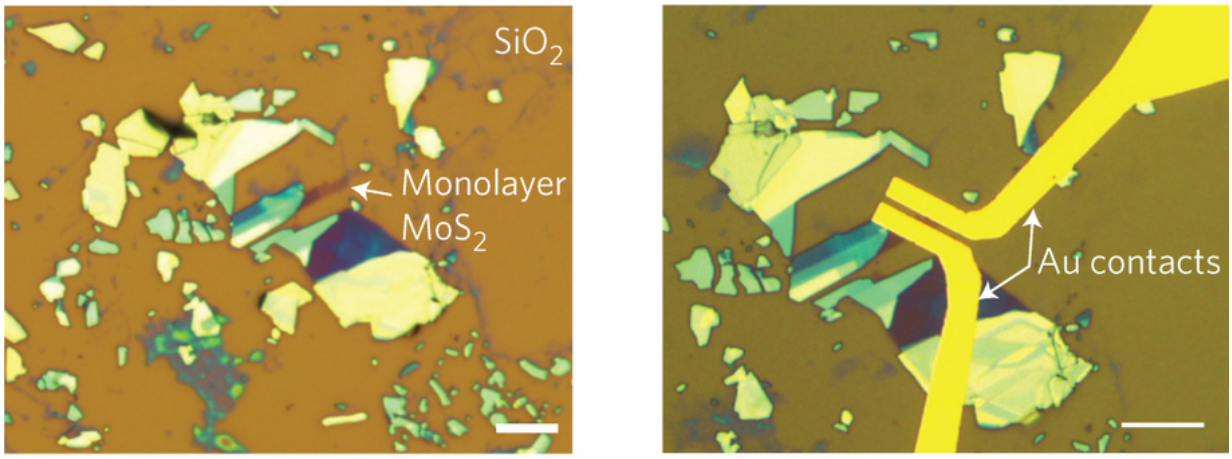

(d) Mechanically exfoliated MoS_2 sheets (left) and deposited gold electrodes (right) on the only monolayer sheet found in that assortment (scale bars are 10 μm) [27]. Copyright © 2013, Rights Managed by Nature Publishing Group.

Figure 5: MoS_2 (a) bulk, (b) exfoliated sheet, and (c) a 3D model of a bilayer.

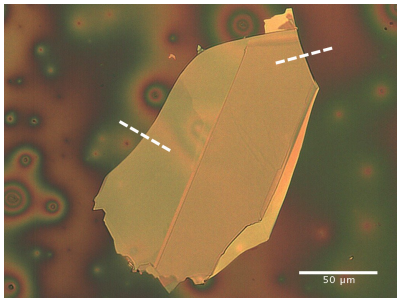

(a) Optical micrograph of the exfoliated sheet. A thickness of around 60 nm (left side) and 80 nm (right side) was determined using AFM along the white dashed lines in the picture. Scale bar is 50 μm.

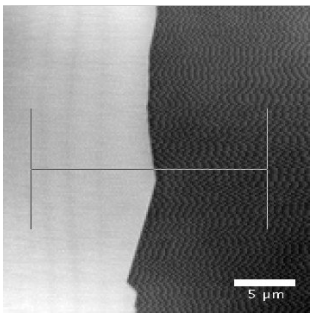

(b) AFM image showing the PDMS/SiO_2 substrate (right side, dark) and the MoS_2 sheet edge (left side, bright). A height profile was taken along the horizontal line, show in (c), averaging the profile across 10 μm wide strip (vertical lines in the image). Scale bar is 5 μm.

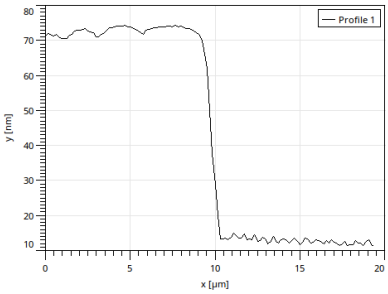

(c) Height profile of the MoS_2 sheet edge along the section shown in (b). The sheet thickness is around 60 μm.

Figure 6: Mechanically exfoliated MoS_2 sheets on PDMS/SiO_2.

I.2.5 Synthesis of suspensions of layered materials

Layered materials exhibit desirable electro-optical properties only in the form of single-layer to few-layer sheets. Among the various methods of obtaining single- and few-layer sheets, such as mechanical cleavage exfoliation (MCE) [26], chemical-vapour deposition (CVD) [29, 30], sulphurisation [31], pyrolysis [25], hydrothermal growth [32] and liquid-phase exfoliation (LPE) [4,10,25], only LPE approach has the advantage of yielding a readily solution-processable MoS_2, which can be subsequently used for low-temperature large-area processing [4, 10]. The LPE approach has in fact become the method of choice for synthesizing MoS_2 for ink formulation for print processing [1, 33–35].

The basic approach in LPE is ultrasonic agitation of a precursor (such as an MoS_2 micropowder) in organic solvents, but it is difficult to obtain large sheets using strictly organic solvents and sonication, and only low aspect-ratio nanoscale sheets can be consistently exfoliated in this method. The basic sonication approach is usually augmented with additional steps for increasing the aspect ratio and reducing the thickness of exfoliated sheets.

In general, liquid phase exfoliation involves several of the following steps: pre-expansion (to initially increase the inter-layer separation), intercalation (to reduce the inter-layer adhesion by introducing guest ions), sonication (to force layer separation), centrifugation or filtration (to isolate the stable suspension from the sediment), solvent exchange (to change the dispersing medium) and stabilization (to prevent agglomeration and sedimentation) (Figure 7).

Coleman *et al.* [4] found optimal solvent parameters for dispersing 2D nanosheets produced by liquid phase exfoliation. They initially sonicated commercial powders in various common solvents, followed by centrifugation. The supernatant is kept. They found that maximal material retention is obtained in solvents with surface tension close to $40\,\mathrm{mN \cdot m^{-1}}$. Using Hansen solubility parameter theory, they concluded that efficient solvents are those that minimize the energy of exfoliation. Interestingly, the top five solvents were all pyrrolidones.[5] N-methyl pyrrolidone (NMP) was one of the best solvent for MoS_2, being able to retain $0.3\,\mathrm{mg \cdot mL^{-1}}$ of MoS_2 in suspension,[6] as well as having other convenient physical properties such as low viscosity. In this method, the MoS_2 maintains its initial semiconducting 2H phase, unlike in processes involving intercalation where some of the MoS_2 transitions into the metallic 1T phase. An average sheet thickness of 3-12 nm was reported, but the particle size distribution was not provided. Several 500 nm wide sheets were presented but they appear to be at the tail of the size distribution. They reported a field-effect only for one single-sheet device, which was patterned using e-beam lithography. The

[5] Namely, N-vinyl-pyrrolidone (NVP), N-octyl-pyrrolidone (N8P), N-dodecyl-pyrrolidone (N12P), cyclohexyl-pyrrolidinone (CHP) and N-methyl pyrrolidone (NMP).

[6] That is two orders of magnitude higher than the commercial MoS_2 suspension from Graphene Supermarket used throughout this thesis.

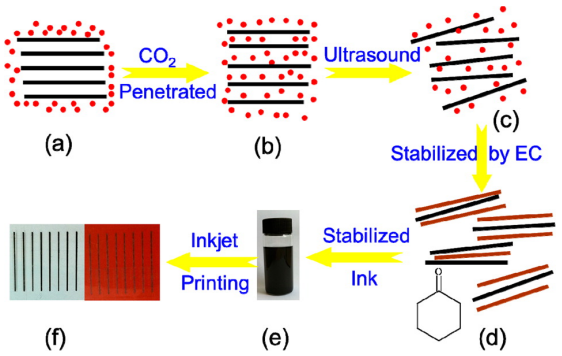

(a) **Schematic illustration of the preparation process of pristine graphene ink and its printed electrodes.** (a) Layered graphite was immersed in supercritical CO_2. (b) CO_2 molecules penetrated and intercalated in the interlayer of graphite, (c) forming single- or few-layer-thick graphene sheets. (d) Graphene sheets were stabilized by EC in cyclohexanone and (e) formed stable graphene ink. (f) Graphene electrodes were printed on PET and PI substrates [37]. Copyright © 2014 American Chemical Society.

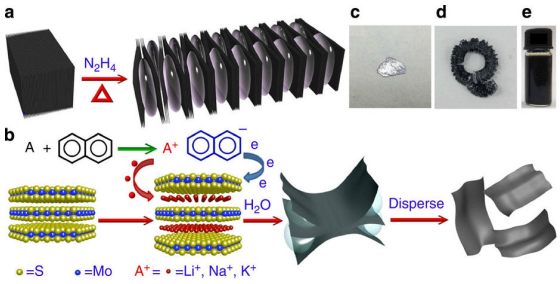

(b) **Schematic illustration of the preparation process of MoS_2 ink.** (a) Bulk MoS_2 is pre-exfoliated by the decomposition products of N_2H_4. (b) Pre-exfoliated MoS_2 reacts with $A^+C_{10}H_8^-$ to form an intercalation sample, and then exfoliates to single-layer sheets in water. (c) Photograph of bulk single-crystal MoS_2, (d) photograph of pre-exfoliated MoS_2, (e) photograph of Na-exfoliated single-layer MoS_2 dispersion in water [24]. Copyright © 2014, Rights Managed by Nature Publishing Group.

Figure 7: Select methods for preparation of graphene and MoS_2 inkjet inks via liquid-phase exfoliation.

sheet exhibited n-type behaviour with mobility of $0.01\,\mathrm{cm^2V^{-1}s^{-1}}$.

Recently, the same group used NMP to exfoliate various semiconducting TMDCs, followed by separation by sheet size via centrifugation and solvent exchange to isopropanol [1].

Yao *et al.* [33] obtained a stable MoS_2 nanosheet suspension with a concentration of $26.7\,\mathrm{mg\cdot mL^{-1}}$ after 3 hours of mortar grinding of MoS_2 micropowder in NMP, followed by 2 hours of sonication in 45 vol% ethanol/water solution. The resistance of the printed film changed irreversibly upon exposure to NH_3 gas.

Thin, large aspect ratio sheets were successfully obtained by expansion-intercalation methods (Figure 7) [24,36], which are currently one of the promising approaches for solution-processable microscale ultrathin sheets. Zheng *et al.* [24] used hydrazine to expand the inter-layer distance of bulk MoS_2 in a hydrothermal reaction, followed by sodium intercalation, sonication and centrifugation. This way they were able to obtain few-layer MoS_2 sheets with lateral sizes of $1-10\,\mu$m and they reported field-effect mobilities of $1-8\,\mathrm{cm^2\cdot V^{-1}s^{-1}}$ for a single layer sheet and $20-80\,\mathrm{cm^2\cdot V^{-1}s^{-1}}$ for a few-layer sheet (Table 3). Thanks to the high flexibility of MoS_2 sheets, they were able to use a nozzle as small as $10\,\mu$m for inkjet-printing their suspension. The deposited film consisted of continuously overlapping sheets but they did not report any devices fabricated from networks of overlapping sheets.

Another challenge is dispersion stability. Stable dispersions of layered materials can be achieved by functionalizing the edge of the sheets [36], but for the functional groups to be effective in dispersing the sheets, the edge-to-area ratio must be large, which limits the size to nanoscale dimensions. Therefore,

Table 3: Select ink formulations and properties of inkjet printable 2D layered materials.

	Graphene [37]	**Graphene** [36]	**MoS_2** [34]	**MoS_2** [24]
Exfoliation method	CO_2 intercalation	lithium and naphthalene intercalation in THF	Sonication in DMF; centrifugation	sodium naphthalenide intercalation
Sheet thickness	0.4-0.9 nm (<5 layers)	not given	5-7 nm (<6 layers)	<1 nm (1 layer)
Sheet lateral size	25 nm	not given	40-100 nm	10-20 μm
Function	Metallic contact	Metallic contact	Resistor	Semiconductor
Solvent	4:1 Cyclohexanone–ethylene-glycole	1:3 isopropanol (IPA) - n-butanol (n-BuOH)	3:1 terpineol - ethanol	2:1 ethanol-water
Concentration	$1\,\mathrm{mg}\cdot\mathrm{mL}^{-1}$	$1.4\,\mathrm{mg}\cdot\mathrm{mL}^{-1}$	$5.3\,\mu\mathrm{g}\cdot\mathrm{mL}^{-1}$	$20\,\mu\mathrm{g}\cdot\mathrm{mL}^{-1}$
Stabilizer	0.1% w/v ethyl-cellulose	$5\,\mathrm{mg}\cdot\mathrm{mL}^{-1}$ Plasdone S-630[a]	Ethyl cellulose	none
Substrate treatment	HMDS	Printing at 50°C	Printing at 40°C	Printing at 60°C
Film thickness	150 nm	800 nm	50 nm	single/few layer
Post treatment	Anneal: 300 °C, 30 min	none	Anneal: 450°C for 1 hr	none
Conductivity / mobility	$9.24\cdot10^3\,\mathrm{S}\cdot\mathrm{m}^{-1}$, $\sim 1\,\mathrm{k}\Omega\,\square^{-1}$	$1-2\,\mathrm{k}\Omega\,\square^{-1}$	$8.9\cdot10^{-5}\,\mathrm{S}\cdot\mathrm{m}^{-1}$	$1-8\,\frac{\mathrm{cm}^2}{\mathrm{Vs}}$ (1L), $20-80\,\frac{\mathrm{cm}^2}{\mathrm{Vs}}$ (FL)[a]

[a] Surface active polymer: 60:40 copolymer of N-vinyl-2-pyrrolidone and vinyl acetate, Ashland Inc., USA.
[b] 1L and FL stand for single-layer and few-layer, respectively.

edge functionalization is not suitable for large sheets. As reported by Coleman *et al.* [4], only solvents with particular properties, described by the Hansen solubility theory, are able to minimize the energy of exfoliation. Several examples of ink formulation and processing are presented in Table 3.

Since only a limited set of solvents is able to keep large MoS_2 sheets stable in suspension, the solvent choice for ink formulation is limited, and their physical properties may impede inkjet printing. The viscosity of NMP, for example, is too low ($\sim 1.65\,\mathrm{mPa}\cdot\mathrm{s}$) and therefore cannot be printed, and its boiling point is too high (203 °C), which means that printed droplets must be annealed to obtain a dry film. On the other hand, the use of convenient, low boiling point solvents such as isopropanol would require either preparing fresh batches of ink by solvent exchange prior to printing, or using suspensions with small enough nanosheets. Larger sheets are desirable since this way the number of inter-sheet charge transport events along a conductive path is minimized.

Coleman *et al.* [4] used MoS_2 micropowder from Sigma to exfoliate thin sheets. The range of MoS_2 sheet sizes that they obtained was 50-1000 nm with multilayers or clusters (3-12 nm) that have aggregated during deposition. They reported size distributions of <L>=170 nm, <W>=90 nm, <N>=3.3 layers. After collecting the sheets into thick circular pellets (Figure 9), the observed conductivity was $3.6\cdot10^{-5}\,\mathrm{S}\cdot\mathrm{m}^{-1}$

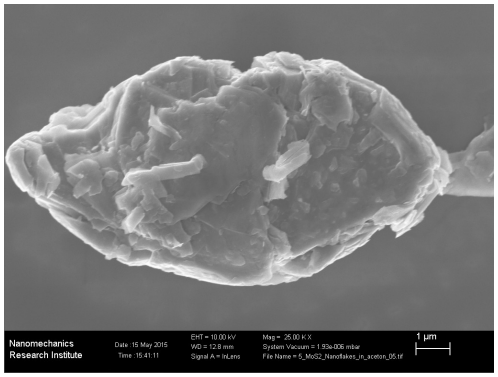

Figure 8: Typical grain in MoS_2 micropowder (Sigma Aldrich).

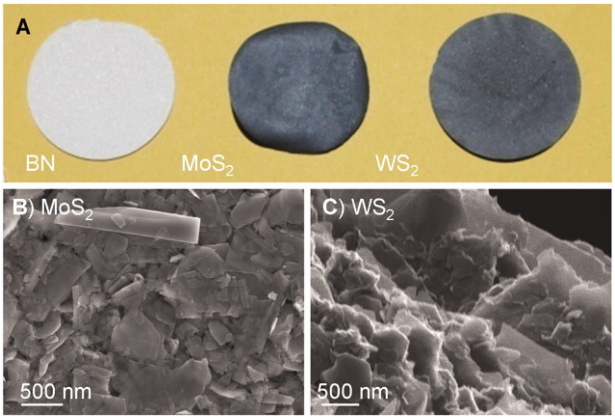

Figure 9: (A) liquid-exfoliated 50 μm-thick pellets ("free standing films") of BN, MoS_2 and WS_2 [4]; (B) SEM and (C) HIM image of the surface of the MoS_2 and WS_2 films, respectively. Copyright © 2011, American Association for the Advancement of Science.

and a field effect was reported only for a single sheet (single crystal) with L=250 nm. They used sonication and centrifugation of micropowder MoS_2 in common solvents, NMP and IPA in particular.

Recently, the same group exfoliated MoS_2 nanosheets using NMP with a distribution of <N>=14 and <L>=346 nm [1]. They fabricated electrolyte-gated TFTs out of 2D layered nanosheet networks of conducting sheets (graphene), semiconducting sheets (MoS_2, among others), and insulating sheets (BN). Interestingly, the dry nanosheet network (before introducing an electrolyte) was able to transport a current of few nA under $V_d = 1\,\mathrm{V},\ V_g = 0\,\mathrm{V}$ across a 120 μm-long channel device. They did not report a field-effect for dry devices.

Another promising exfoliation method is based on electrostatic repulsion. Chen *et al.* [38] demonstrated MoS_2 exfoliation via sonication in the presence of imidazole, an organic salt. They were able to consistently obtain few-layer MoS_2 sheets with areas of $10 - 100\,\mu\mathrm{m}^2$ but no TFTs were reported, as the application they were targeting was supercapacitors.

This research focuses on fabricating devices from a percolating network of small nanosheets (lateral size $\lessapprox 100\,\mathrm{nm}$), which are significantly easier to produce and stabilize compared to larger sheets. In addition, films made from a large number of small nanosheets are expected to have a more consistent electronic performance compared to devices made of a single sheet because even minor variations in defects between single sheet devices could significantly alter the performance from device to device.

I.3 Inkjet printing

Manufacturing arbitrary shapes and compositions in a rapid prototyping approach is widely employed in many fields such as electronics [39–41], biomedical devices [42], combinatorial chemistry [43] and more. Similar to 3D printing of macro-scale features, which successfully addresses a growing number of aspects of rapid prototyping (such as structural rigidity, chemical tolerance and electric conduction), inkjet printing addresses increasingly more aspects of prototyping in the micro-scale.

Inkjet printing is a promising method for controlling the deposition of thin-films in large-area applications. While vacuum deposition (e.g. chemical-vapour deposition) offers superior control over the deposited thickness, defect density, and overall performance, it is not practical for large-area fabrication and for temperature-sensitive materials. Inkjet printing is operated in air and therefore the deposition area is not limited by vacuum chamber size, as is the case with various vacuum deposition methods. In addition, since inkjet printing is an additive deposition method, the number of processing steps and the material waste are reduced compared to traditional cleanroom processes [44].

Inkjet printing is a versatile deposition method for a broad range of substances and is "substrate-agnostic" in the sense that the process of applying a substance onto a substrate is indifferent to the substrate used, such that successful deposition depends entirely on the interface interactions of the materials involved. Inkjet printing is a mature deposition technology that was demonstrated in the past several decades for graphical printing, and it is an emerging technology for digital fabrication that was demonstrated for numerous substances, including metals, ceramics, proteins, living cells, pharmaceuticals and polymers, to name a few, and for various applications such as conductive traces for printed circuits, thin-film transistors (TFTs) for sensors, organic light-emitting diodes (OLEDs) for large-area low-cost displays, nanocapsules for precise drug delivery, hydrogel microarrays for biomedical applications, and more [39, 40, 42, 45, 46].

Inkjet printing is a promising method for thin-film transistor fabrication from solution-processable materials. Many aspects of device fabrication have been studied and optimized in the past decade, namely stable ink formulation, precise feature deposition, narrow channel fabrication, insulator deposition and 3D circuit integration. The major challenge of exfoliating large lateral dimensions sheets of 2D layered materials was recently addressed [24] and a high-mobility device with a 20 μm single crystal MoS_2 channel was demonstrated. For the first time, a printed device outperformed amorphous silicon by a factor of almost 100 (Section I.3.3).

Generally, inkjet printing is advantageous for low-end high-volume applications. In particular, inkjet printing is an emerging technology for fabricating thin-film transistors (TFTs) for large-area flexible and transparent applications such as bendable displays.

Inkjet printing 2D materials for TFTs encompasses several major challenges: obtaining thin sheets with large lateral dimensions, maintaining a stable suspension of the sheets, controlling the arrangement of the sheets in the printed patterns and maintaining high quality interfaces between the 2D materials and other device components.

Electronic functional inks include conductive inks and semiconducting inks. Popular inkjet printable *conductive* inks are based on precious metals (silver, gold) and are therefore expensive, in addition to being insoluble in most common solvents and prone to oxidation immediately after printing [47]. The vast majority of inkjet printable *semiconducting* inks are organic compounds, which have relatively low field-effect mobility ($\sim 1\,\mathrm{cm^2V^{-1}s^{-1}}$). On the other hand, a handful of low-cost 2D layered materials that exhibit high performance, such as graphene and TMDCs, can be used as conductors and semiconductors in inkjet printed devices.

Inkjet printing successfully addresses low-cost fabrication demands, and single crystal MoS_2 devices successfully address high performance. Single crystal MoS_2 devices showed mobilities as high as $700\,\mathrm{cm^2 \cdot V^{-1}s^{-1}}$ [18], but for practical TFTs a sheet as large as $5 - 10\,\mu$m is needed. Such large sheets are very difficult to produce with single (or few) layer thickness. Nanosheets, however, have been produced by numerous studies with various sizes of around 300 nm in large quantities and concentrations [1, 4]. However, while single crystal MoS_2 devices have been continuously demonstrated since 2011 [26], the first publication on MoS_2 nanosheet-based TFTs appeared only in April 2017 [1] and its operation relied on electrolyte-gating.

There are numerous challenges involved in fabricating devices from a percolation network of nanosheets: exfoliation (or synthesis) of large single/few-layer MoS_2 sheets, stabilizing the sheets in suspension, deposition of a uniform, percolating film, removal of contaminants from the dry film, interfacing with electrodes and dielectric materials, improving the inter-sheet conductance and prevention of oxidation. Some of these challenges are amplified as the average sheet size decreases.

Essentially, any solution with viscosity and surface tension within a fairly broad range can be printed using piezoelectric inkjet technology. The size and maximum resolution of the printed features depend on the physical properties of the ink (surface tension, viscosity), the nozzle size of the printhead and the spreading properties of the printed material, but the typical feature size and pitch are in the range of $30 - 300\,\mu$m.[7] After a drop of the solution has been successfully jetted from the printhead (Figure 10), both viscosity and surface tension still play an important role in the properties of the printed feature (Figure 11): a surface tension that is too low may cause splashing upon impact with the substrate, and a viscosity that is too low may cause satellite drops to break-off in-flight towards an off-centred direction.

[7] Recently, devices with channel length of $2\,\mu$m were obtained via surface energy modifications, but the pitch of such devices still depends on the size of printed droplets [41, 48].

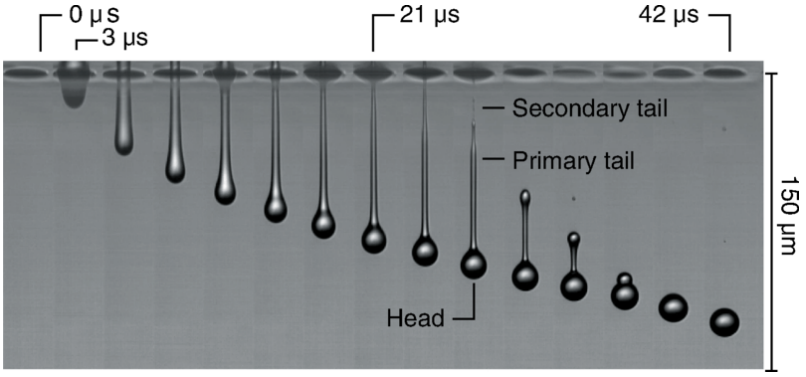

Figure 10: 3 μs-delay time-series of a 23 μm diameter droplet ejected from a nozzle (a sequence of 15 individual images joint into a single image) [5]. © 2014 American Physical Society

I.3.1 Printability

Various rheological properties, such as density, surface tension and viscosity, have a strong effect on the printing process. The morphological properties of the ink constituents, such as sheet dimensions, can also contribute to drying dynamics, printing instability and nozzle clogging [47].

The main restrictions on printability of materials originates in the mechanism of drop formation. For a material to be printable, it must have appropriate dynamic viscosity η, surface tension γ and density ρ, such that the energy transferred to the liquid would be able to form and exert a drop (Figure 10).

These limitations have been studied and expressed in terms of several dimensionless numbers, namely the Reynolds number, $\mathrm{Re} = \frac{\rho v d}{\eta}$, and the Weber number, $\mathrm{We} = \frac{\rho v^2 d}{\gamma}$, which both depend on the drop velocity v and its characteristic length d (drop diameter, in this case), and the Ohnesorge number, $\mathrm{Oh} = \frac{\sqrt{\mathrm{We}}}{\mathrm{Re}} = \frac{\eta}{\sqrt{\rho \gamma d}}$, which eliminates the velocity dependence [6]. A simplified limitation for printability can be expressed in terms of a so-called "Z-number", $1 < Z \equiv \mathrm{Oh}^{-1} < 10$, where low Z values correspond to high energy dissipation by the liquid (high viscosity), and high Z values correspond to formation of multiple satellite drops (Figure 11). However, a modification in the ejection system by Choi *et al.* [49] was recently reported to significantly improve the printability range to $0.23 < Z < 84.77$ – their custom printhead ejected droplets using a flexible membrane and a fully pneumatic actuator, such that the physical properties of the fluid had a lesser role in the jetting process.

In general, surface tension and viscosity dictate the drop formation of Newtonian fluids, such that the minimum required surface tension and maximum viscosity of a Newtonian fluid to be printable is about $\gamma_{\min} \sim 30\,\mathrm{mN \cdot m^{-1}}$ and $\eta_{\max} = 100\,\mathrm{cP}$, respectively [50]. Commercial products, such as the Dimatix DMP 2800 , recommend formulating inks with $\gamma \sim 30\,\mathrm{mN \cdot m^{-1}}$ and $\eta \sim 11\,\mathrm{cP}$ [51]. Too low viscosity results in lack of acoustic damping and the formation of satellite drops.

In order to maintain a consistent printing quality and resolution, it is necessary to obtain stable jetting

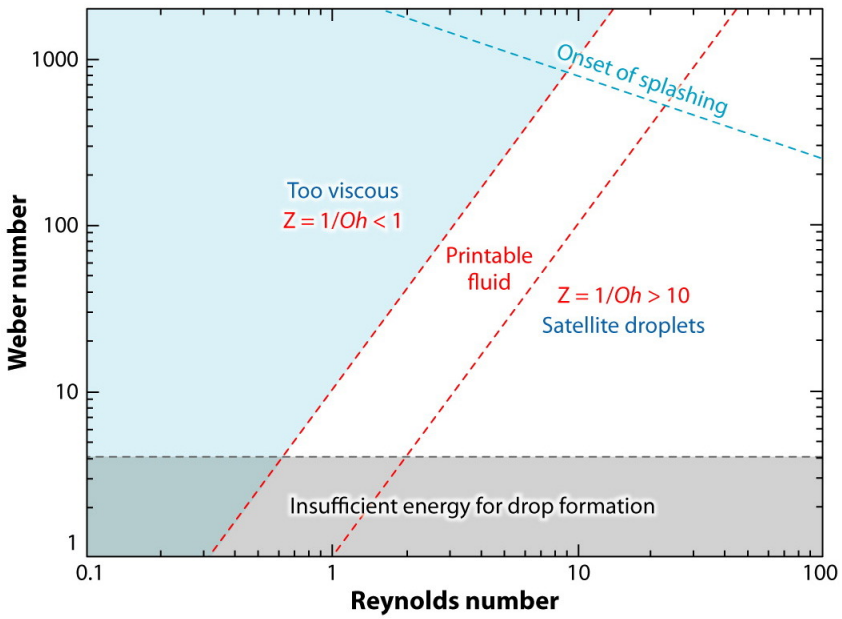

Figure 11: Region of printable liquids in terms of Weber number and Reynolds number [6]. Copyright © 2010, Annual Reviews

without satellite drops or jet deflection.

I.3.2 Parameters controlling the formation of printed features

I.3.2.1 Droplet geometry

In drop-casting and inkjet printing the droplets are of the size $1-5\,\mathrm{mm}$ and $20-100\,\mu\mathrm{m}$, respectively. Since the capillary length $\kappa^{-1}=\sqrt{\frac{\gamma}{\rho g}}$ is several orders of magnitude larger than the size of typical droplets, surface tension effects dominate the shape of the droplet, and gravity can be neglected [52]. Therefore, the shape of the droplet both in-flight and after equilibration on the substrate can be approximated by spherical sections. In-flight, the droplet shape is assumed to be spherical and on the substrate it is assumed to be a spherical cap. With such approximations, the volume Ω of a spherical cap can be expressed as a function of its base diameter $2l$ and contact angle θ [52] (Figure 12):

$$\Omega\left(\theta,l\right)=\frac{\pi}{3}l^{3}\frac{\left(2+\cos\theta\right)\left(1-\cos\theta\right)^{2}}{\sin^{3}\theta} \tag{3}$$

Using this expression, measuring the contact angle θ (Table 4) would allow to evaluate the volume needed to be deposited to uniformly cover the channel area of a device (Section III.2). Another common term in droplet geometry is the contact line, which is the perimeter of the circular contact area between the droplet and the substrate, equal in length to $2\pi l$.

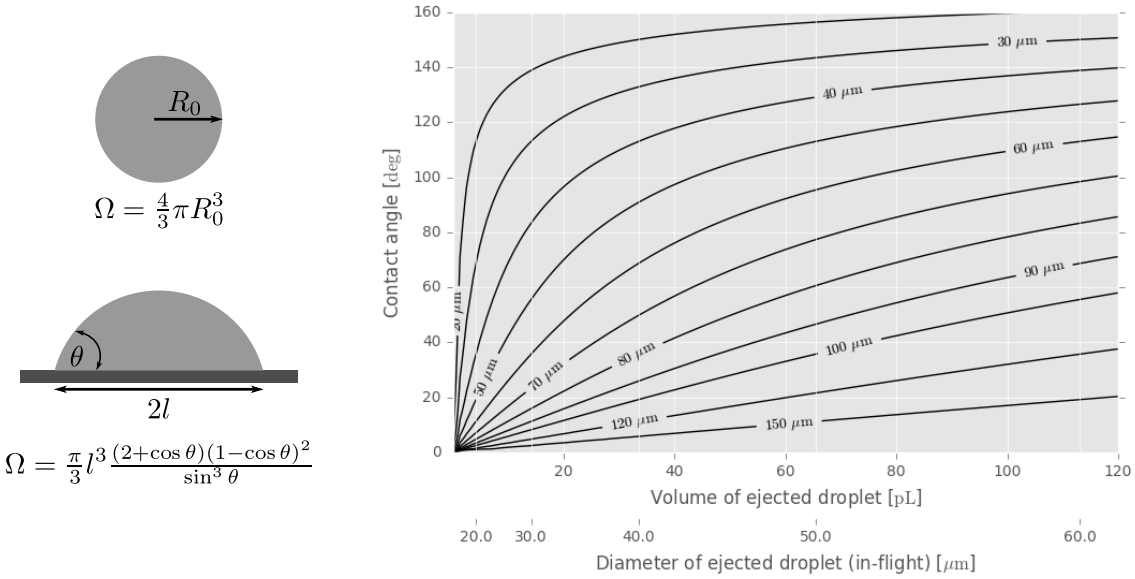

(a) Definitions.

(b) Base diameter of spherical cap as a function of ejected volume and contact angle.

Figure 12: Droplet geometry.

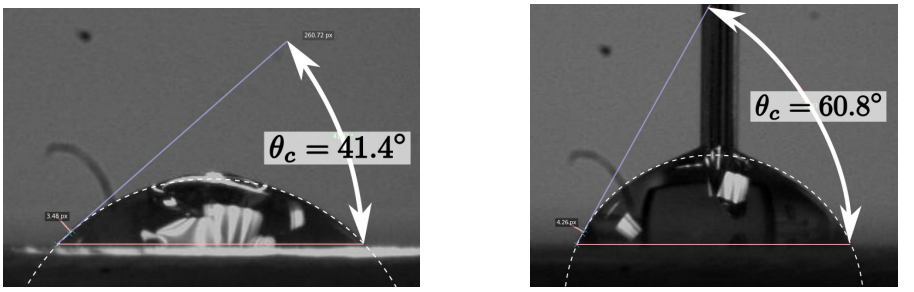

(a) Apparent contact angle of GS-MDS-NF on HMDS-treated substrate.

(b) Receding contact angle of DI water on HMDS-treated substrate.

Figure 13: Contact angle measurements.

Table 4: Measured contact angles ($\theta_{rec}/\theta_{app}/\theta_{adv}$), in degrees. Numbers in brackets are approximations (averages). A single entry indicates an apparent contact angle. High difference between the advancing and the receding angles indicates possible droplet pinning during evaporation.

	Treatment	DI water	EtOH	45% EtOH	GS-MDS-NF
SiO_2	N_2-cleaned	40	-	-	-
SiO_2	sol.-clean	31	0	0	0
SiO_2	O_2-cleaned	-/23/38	0	0	0
SiO_2	O_2+HMDS	61/(72)/83	0	32	41
SiNx	sol.-clean	26/53/61	0	-/30/49	27
SiNx	O_2-cleaned	13/19/33	0	0	0
Cr	sol.-clean	24/36/54	0	0	19
Au	N-cleaned	38/60/88	0	18	0/(20)/41

I.3.2.2 Ink-substrate compatibility

The resolution of printed features depends on the spreading properties of a given ink on a given substrate. In general, extensive spreading and slow drying decrease the printing resolution [36]. Contact angle measurements provide such information (Figure 13). In order to obtain a continuous film from a low concentration suspension of MoS_2 it is desirable to have high contact angles. Droplets with a smaller base diameter confine the deposited material to a smaller area, which increases percolation probability at lower deposited volumes. Measured contact angles of typical dispersing medium of MoS_2 inks is given in Table 4. The high spreading on bare SiO_2 requires treating the surface with a hydrophobic layer, such as hexamethyldisilazane (HMDS). Substrate treatment can be avoided by using spray deposition, where a high pressure stream of air accelerates solvent evaporation such that no spreading of the solvent takes place.

I.3.2.3 The "ring-stain" effect

The "ring-stain" effect (commonly known as the "coffee-ring" effect) is the name of a drying phenomena when higher concentration of dried deposited material is accumulated near the drop edge (the contact line) compared to the centre of the drop. A ring-stain may form during the evaporation of the fluid due to a radial convection of the fluid towards the drop edge. Ink viscosity, droplet-substrate interface tension, droplet surface tension and evaporation rate all play a role in the extent of the ring-stain effect. In the case of of water-based solutions used in this research, it is the weak inward Marangoni flow [53] and the relatively long evaporation times [54] that contribute to the ring-stain effect.

Several ways were suggested for reducing the ring-stain effect, such as using a solvent mixture of high and low boiling points [55], varying the drop spacing and substrate temperature [47,56], adding surfactants to the solution [53, 57], or modifying the shape of the suspended particles to exploit shape-dependent capillary interactions without modification of particle or solvent chemistry [58].

A different way to approach the ring-stain effect is to directly exploit its physics for the fabrication of devices with circular symmetry. A set of concentric electrodes can be used to pin droplets to the channel area in between the electrodes, giving the suspended material sufficient time to be transported towards the contact line and deposited there, ideally forming a continuous channel (Figure 25a and Section III.4.3).

I.3.3 Ink formulation for jet printing

Inks are not always straightforward to formulate. The main component of an ink formulation is the solvent, which is selected based on the constituents to be dissolved. Sometimes a co-solvent is added to increase

solubility in inks with multiple constituents and to reduce the ring-effect upon drying. If the resulting viscosity or surface tension are still not within printability regions, a thickening agent, such polyethylene glycol, is added [59].

When suspended particles are involved, such as graphene sheets, it is common to introduce a stabilizing agent such as ethyl cellulose. A common rule-of-thumb is that dispersed particles in the ink should be smaller than $^1/_{20}$-$^1/_{50}$ of the nozzle diameter to avoid clogging [50, 60], effectively limiting the maximum diameter of dispersed particles to $\sim 1\,\mu$m. When the suspended sheets are flexible, much larger ratios are possible [24].

One of the challenges with formulating inks of 2D layered materials is that the solvents that are used for efficient exfoliation do not have appropriate physical properties for inkjet printing [34,35]. Most published exfoliation procedures involve toxic solvents such as N-methyl-2-pyrrolidone (NMP), dimethylformamide (DMF) or dimethyl sulfoxide (DMSO) [1,4,24,33–35], which must be modified or replaced before printing. Coleman *et al.* [4] were the first to suggest NMP as an exfoliation solvent and ethanol as a printing solvent for MoS_2 nanosheets.

Yao *et al.* [33] used vacuum drying and annealing to remove NMP, followed by re-dispersion in 45 vol% ethanol/water solution. The viscosity and surface tension of the MoS_2 suspension were modified by adding 33 wt.% glycerol. In addition, the printhead was heated to 40°C to optimize printing performance.

Li *et al.* [34, 35] used distillation to exchange the exfoliation solvent (DMF) with a printing solvent (terpineol) while increasing suspension concentration, a process they demonstrated for graphene and MoS_2. After sonication in DMF, the nanosheet suspension was stabilized using ethyl cellulose (EC) to prevent restacking of the sheets, which can be easily removed via annealing down to insignificant amounts of residual contamination. In addition to improving suspension stability, the authors reported that the presence of EC improved the uniformity of the dried film. However, in order to eliminate EC residues, baking the sample at 400°C is required, which is relatively high. After solvent exchange to terpineol (viscosity of 40 cP), the suspension was modified by adding 25 vol.% ethanol to optimize printing performance (viscosity of 10 cP).

Zheng *et al.* [24] used tetrahydrofuran (THF) as the intercalation medium and water as the exfoliation medium, followed by drying the exfoliated MoS_2 sheets into a powder. The powder was then redispersed in a 66 vol.% ethanol in water solution prior to printing. The authors reported that the MoS_2 sheets were flexible enough such that $20\,\mu$m large sheets could pass through a $10\,\mu$m nozzle.

McManus *et al.* [61] used water as the intercalation and exfoliation medium. The MoS_2 nanosheet suspension was modified for printing as follows: Triton X-100, a polyethylene glycol-based surfactant, was used to reduce the surface tension; xanthan gum and propylene glycol were used to increase viscosity and

disrupt the capillary flow, which in turn reduced the ring-stain effect.

I.3.4 Substrate treatment

The size of the smallest feature in inkjet printed devices is limited by the minimal achievable droplet diameter and the positional accuracy of the system.[8] One way to overcome this difficulty is via substrate treatment. Modification of the substrate surface prior to printing could have a desirable effect on the confinement of printed features and therefore on the achievable resolution. For example, pre-treatment of the substrate surface with hexamethyldisilazane (HMDS) reduces the wettability of the surface (increases its hydrophobicity) and confines deposited droplets to a smaller contact area. It was observed that such a substrate treatment is also responsible for reducing the ring-stain effect in several reported cases [37, 47]. Similarly, but employing an opposite effect, a hydrophilic, water-soluble poly(vinyl alcohol) (PVA) layer that was spin-coated on a PET substrate was able to pin the contact line of droplets of water-based PEDOT:PSS solution simply by dissolution of the PVA under the contact area [41]. As a result, the conducting polymer's contact line was pinned during the drying process, which prevented the printed droplets from spreading. This facilitated the control of the channel length in their all-inkjet printed TFTs. A line width of $\sim 100\,\mu$m without a ring-stain effect was obtained by maintaining a droplet printing pitch of $50\,\mu$m. The confinement was so effective that the printed electrodes could be consistently separated by a distance as small as $2\,\mu$m, an unprecedented achievement for a printed channel length [41].

Another surface treatment approach for short-channel printed devices is patterning narrow hydrophobic lines. Li *et al.* [48] have recently achieved $3.5\,\mu$m channel length devices by plasma-assisted narrowing down of printed hydrophobic lines, which were used to effectively separate between later-printed source and drain contacts.

It is also common to print on heated substrates to increase the evaporation rate for obtaining well-defined features. On the other hand, increased substrate temperature may increase the turbulence inside the droplet, which in turn could lead to unpredictable drying patterns of the suspended material.

I.3.5 Deposition equipment

Most common graphical desktop printers employ the bubble-jet technology for droplet formation, which uses heating cycles to squeeze ink out of the reservoir. Since elevated heat may be harmful for functional inks, both industry and the research environment adopted the piezoelectric inkjet technology, where an acoustic wave is used instead of heating cycles. A wide range of printing systems is now commercially

[8] The emerging electrohydrodynamic jet printing method shows great promise for printing nanoscale features, however the range of compatible solvents is still very limited and there is no commercial printer available yet [62].

available [51, 63–65].

An important characteristic of a printer's printhead is the number of nozzles, which is directly related to the overall throughput. Using multiple nozzles reduces the printing time, which can be lengthy if a large number of printing passes is required, and multiple printheads are used in an alternating fashion when rapid deposition of multiple ingredients is required.

The printer of choice for this work was CeraDrop L-Serie, an "all-in-one" multi-ejector head, built into a fume hood [63].

Part II

Materials characterization

The properties of materials and their interfaces, as well as their modification, lie at the heart of processing for device fabrication. The major concern in device fabrication is being able to control a functional material for obtaining desirable properties. In TFTs, the major concern is developing a process for forming high quality, thin functional films, in which conductivity could be modulated using a gate bias. In order to achieve this, gaining familiarity with the properties of the materials used is paramount. As this research is focused on films of nanosheet MoS_2, characterization of MoS_2 nanosheet suspensions was carried out.

The properties of MoS_2 sheets depend on their thickness and lateral size. For example, gate switching is expected to be more efficient for thinner films, as thinner films prevent bulk conductivity, and the total channel resistance is expected to be lower with larger sheets, because less inter-sheet transport events would be required from source to drain electrodes. Therefore the thickness and lateral size of the sheets need to be measured (Sections II.1.2, II.2.4). In addition, measuring the concentration of the MoS_2 nanosheets in suspension (Section II.1) is required to obtain estimates for the volume needed to be deposited for forming a continuous channel (Section III.2).

Another aspect in processing MoS_2 nanosheets is their thermal stability. As MoS_2 nanosheets can undergo oxidation at low temperatures (150-200°C) [66], a study of the thermal stability of MoS_2 nanosheets is therefore needed to elucidate the challenges that stand before process development (Section II.2).

The only commercially available MoS_2 suspension during this research was a product by Graphene Supermarket (data sheet in Appendix A), which used an ethanol-water ($EtOH:H_2O$) mixture as the dispersing medium. This suspension was used by Bessonov *et al.* [66] for fabricating memresistive devices.[9]

In addition to the commercial MoS_2 suspension, custom MoS_2 suspension was synthesized in-house using sodium intercalation,[10] as described by Zheng *et al.* [24] (but without a hydrazine pre-expansion step). Sodium and naphthalene were stirred in nitrogen atmosphere in anhydrous tetrahydrofuran (THF) for several hours, cooled by ice-water bath, until the sodium was fully dissolved. MoS_2 micro-powder (Sigma) was added to the solution and stirred for several hours. The product, intercalated MoS_2, was thoroughly washed in THF, followed by sonication in distilled water. The product was filtered to remove non-exfoliated or aggregated MoS_2. This process yielded a water-based MoS_2 suspension at a much higher concentration than the commercially available product.

[9] According to Graphene Supermarket's webpage, and to the best of my knowledge, the publication by Bessonov *et al.* is the only documented report using this product to date.

[10] This synthesis was done with the help of Nicholas Lanigan and Prof. Xiaosong Wang.

Energy-dispersive X-ray spectroscopy (EDX) revealed that both suspensions had sodium residues (Section II.2.2). Use of alkali metals for intercalation exfoliation is known to alter the hexagonal structure of MoS_2 [22]. In particular, intercalating species are known to cause a metallic transition (2H to 1T) in MoS_2 such that an annealing step of up to 300°C may be required to relax the sheets to the semiconducting 2H form [67]. Based on the findings of the thermal stability study (Section II.2.4), a 300°C anneal of nanosheet MoS_2 would have to take place in inert atmosphere. Again, this thermal instability shows the critical importance of proper materials characterization for device fabrication.

II.1 MoS_2 ink characteristics

II.1.1 Determining concentration via UV-vis spectroscopy

In colloidal suspensions, the concentration and size of the dispersed solids play a role in the drying dynamics of deposited droplets (Section III.3; [57]). Filtration can be used to impose an upper limit on the particle size distribution, which also would modify the concentration of the nanosheets. Knowing the exact concentration of the suspension in use allows determining the minimum volume needed to be deposited to form a percolating network of nanosheets (Section III.2), as well as the approximate density of the deposited film.

Determining the concentration of nanoflakes in suspension is not straightforward because various steps in the process reduce the initial concentration (e.g. centrifugation and filtration), such that after this process is completed, the MoS_2 concentration is unknown and needs to be determined. In the case of high concentration suspensions, the concentration can be determined by extracting the solid content in the suspension (e.g. via filtration, drying or freeze drying). However, the nanosheet MoS_2 suspensions that were used in this research had a too low concentration that made the extraction of a measurable amount of solid content impractical. Absorption spectroscopy can be used to overcome this difficulty.

Optical absorption spectroscopy using UV-*vis*-NIR is useful for determining the ink concentration from the Beer-Lambert relation $A = \alpha l c$, where l [m] is the light path length, c $\left[\mathrm{g \cdot L^{-1}}\right]$ is the concentration of dispersed material and α $\left[\mathrm{L \cdot g^{-1} m^{-1}}\right]$ is the absorption coefficient. For MoS_2, the absorption coefficient at 672 nm is $\alpha_{672\mathrm{nm}} = 3400\,\mathrm{L \cdot g^{-1} m^{-1}}$ [4].

Each sample measurement is automatically corrected with a background sample that consists of only the dispersing medium. This way, the measured sample absorption is corrected with the baseline contribution of the cuvette and the dispersing medium.

The cuvettes in use were 1.5 mL methylmethacrylate, designed for 280-800 nm, with 10 mm optical length, such that the conversion between absorption and concentration is as follows:

$$c = \frac{A}{\alpha l} = \frac{A}{3400 \cdot 0.01} = \frac{A}{34}\ \left[\frac{\mathrm{g}}{\mathrm{L}}\right] \tag{4}$$

To obtain accurate results, a proper background sample must be used. A sample of the commercial MoS_2 suspension that was filtered three times through a $0.2\,\mu$m filter had no MoS_2 peaks, confirming that the $0.2\,\mu$m filter was effective in separating the MoS_2 out of the suspension down to below measurable values.

For extracting concentration from UV-vis spectra, the triple-filtered suspension was used as the back-

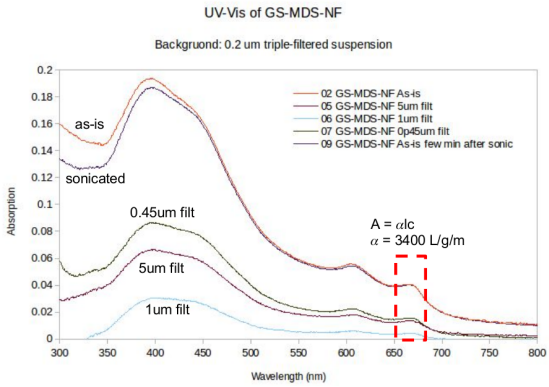

(a) Absorption spectra of the commercial MoS_2 ink in the range 800-300 nm.

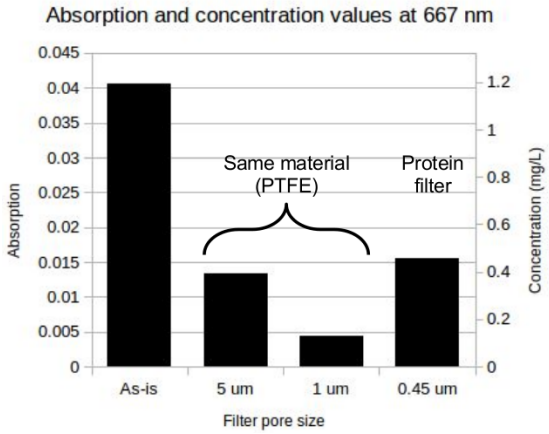

(b) Absorption at 667 nm and the corresponding concentration from Beer-Lambert law. All samples had a peak at 667 nm, which can be attributed to a systematic shift from the expected 672 nm.

Figure 14: UV-vis results for the commercial MoS_2 ink by Graphene Supermarket, correlating pore size filter used for filtration to final MoS_2 concentration. The background was a triple-filtered ink sample through $0.2\,\mu$m pore size.

ground. It appears that the actual concentration of the original suspension is only around $1.2\,\mathrm{mg}\cdot\mathrm{L}^{-1}$, in contrast to the reported $18\,\mathrm{mg}\cdot\mathrm{L}^{-1}$(Figure 14). Alarmingly, the type of filter used had an influence on the filtered concentration, as using a low pore size ($0.45\,\mu$m) protein filter[11] resulted in a higher concentration than using filters with higher pore sizes ($1-5\,\mu$m) PTFE filters. This can be attributed to the different materials and vendors that the filters were acquired from. This finding is important to take into consideration when comparing films from filtered suspensions.

Interestingly, the manufacturer of the commercial ink reported that the MoS_2 is suspended in 45 vol.% EtOH:H_2O, but closer examination suggests that the composition is slightly different. The sweet odour of the solution is another indication for the different composition. A $0.2\,\mu$m triple-filtered suspension was measured for UV-vis absorption with 45 vol.% EtOH:H_2O solution as the background. A significant difference in absorption profile was observed (Figure 15), suggesting that there is a compositional difference between the actual suspending medium and 45 vol.% EtOH:H_2O, which should be taken into account in the ink formulation.

A similar procedure for the in-house Na-exfoliated MoS_2 resulted in a concentration of approximately 10 times higher than the commercial MoS_2 suspension.

[11] PALL AcroDisc Syringe Filter $0.45\,\mu$m Supor Membrane Low Protein Binding Non-Pyrogenic.

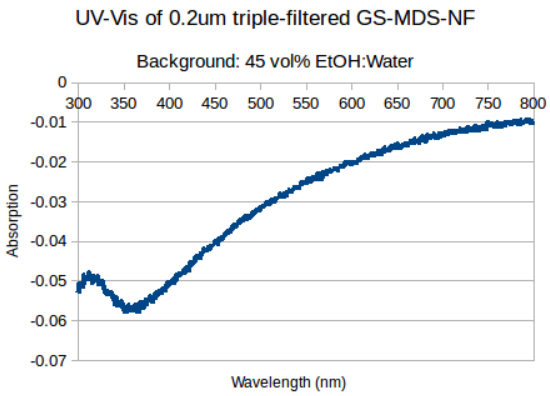

Figure 15: Absorption spectra of the commercial MoS_2 ink, triple-filtered through 0.2 μm pore size, with 45 vol.% EtOH:H_2O solution as a background.

II.1.2 Particle size distribution

As mentioned previously, the performance of a nanosheet network is limited by inter-sheet transport [68]. Therefore, the number of sheets needed to bridge a channel gap have an impact on the overall device performance. The commercial ink from Graphene Supermarket has an advertized sheet size of 500 nm, suggesting that a 5 μm channel can be bridged by several tens of overlapping sheets at most. However, SEM images revealed that 500 nm sheets are extremely rare and cannot be counted upon for the formation of a continuous film. Measuring the particle size distribution would provide the needed statistics faster and over a larger sample size than collecting and processing AFM, SEM or Raman mapping images.

Dynamic light scattering (DLS) measures the light scattered due to the Brownian motion of the particles in suspension and can measure particles as small as 2 nm. The fluctuations in light intensity are correlated to the hydrodynamic radius of the particles via the Stokes-Einstein equation, which relates the diffusion constant D to the viscosity of the solvent η and the radius of the particles r:

$$D = \frac{k_B T}{6\pi\eta r} \tag{5}$$

This equation is applicable for low Reynolds number diffusion of spherical particles in a solvent.

One limitation of DLS is that it is based on the diffusion of particles in suspension, hence different particles with the same diffusion dynamics would exhibit the same hydrodynamic radius. Moreover, DLS results are biased towards large size particles due to the strong dependence on particle size ($\sim d^6$) of Rayleigh scattering, defined by

$$\frac{I}{I_0} = \frac{1+\cos^2\theta}{2R^2}\left(\frac{2\pi}{\lambda}\right)^4\left(\frac{d}{2}\right)^6\left(\frac{n^2-1}{n^2+2}\right)^2, \tag{6}$$

where I_0 is the incident intensity, I is the intensity of scattered light, θ is the scattering angle, R is the distance to the particle, λ is the wavelength of incident light, d is the diameter of particle (assumed to be spherical) and n is the refractive index of the particle.

Before measurement, the suspension is filtered to cutoff any dust content. A common rule-of-thumb for filtering DLS samples is using a filter with pore size three times larger than the size of the largest expected particles [69]. In the case of GS-MDS-NF, the reported particle sizes are 100-500 nm. Therefore, the use of $1\,\mu$m and $5\,\mu$m filters are of interest, as well as not using filtration, for comparison.

In most measured samples, the count rate was within good range and lower than the recommended maximum of 2 Mcps (million counts per second). Only the $1\,\mu$m-filtered sample had a count rate that was too low to obtain a reliable measurement, which is in agreement with the low absorption peak of $1\,\mu$m-filtered samples shown in the previous section. Measured particle size distributions are reported in Figure 16. The number percent shows a clear bias towards sub-100 nm particles, which indicates that the vast majority of MoS_2 nanosheets in suspension is significantly smaller than the advertised size of 100-500 nm. This observation is supported by AFM profiles (Figure 17) and by the fact that virtually no sedimentation was collected after high speed centrifugation of the suspension (around 12000 RCF[12]), indicating that the suspension is mostly comprised of extremely small nanosheets [70, 71]. While larger size sheets are indeed present in suspension (intensity percent distribution is centred around 100 nm; not shown), their number percent is too low to be the primary constituents of a percolation network. Since most of the nanosheets are extremely small, their temperature sensitivity is expected to differ from bulk material, which may impose a limit on the maximum annealing temperature and therefore also on the maximal boiling point of the ink constituents (solvents, stabilizers, surfactants). For this reason the effect of annealing was studied and is presented in Section II.2.

[12]Relative centrifugal force, RCF, is calculated as follows: $\mathrm{RCF} = \frac{a_r}{g} = \frac{\omega^2 r}{g} = \left(\frac{\pi}{30} N_{\mathrm{RPM}}\right)^2 \frac{r}{g}$, where N_{RPM} is the rotor speed in revolutions per second, r is the rotational radius and g is the gravitational acceleration.

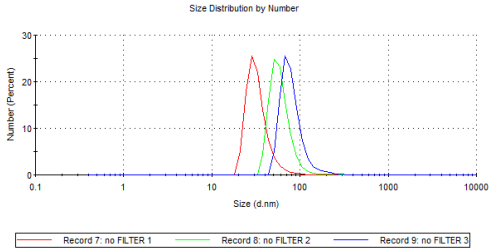

(a) GS-MDS-NF, no filter. Result quality: Good, PdI: 0.424, count rate: 397 kcps.

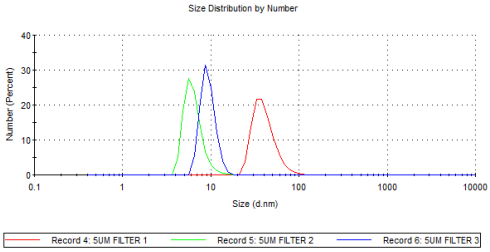

(b) GS-MDS-NF, 5 μm filter. Result quality: Good, PdI: 0.371, count rate: 114 kcps.

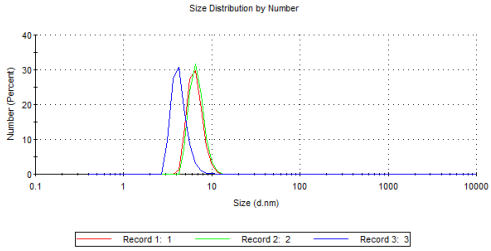

(c) GS-MDS-NF, 1 μm filter. Result quality: poor, PdI: 0.403, count rate: 38 kcps.

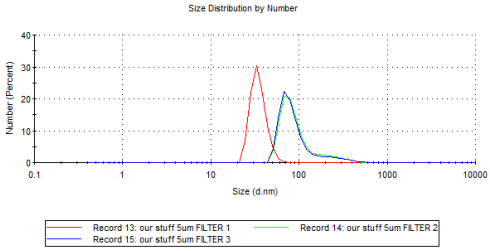

(d) In-house Na-exfoliated, 5 μm filter. Result quality: Good, PdI: 0.270, Count rate: 143 kcps. Particles appear to aggregate during measurement.

Figure 16: DLS analysis of MoS_2 nanosheets, using using Malvern Zetasizer Nano. Every measurement was repeated three times (red, green, blue curves). Most sheets are 10-100 nm large.

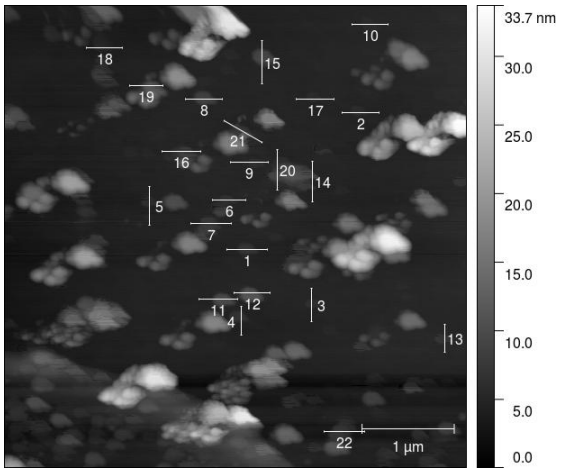

(a) AFM image showing multiple aggregates of MoS_2 nanosheets. Profiles of the larger single sheets were measured.

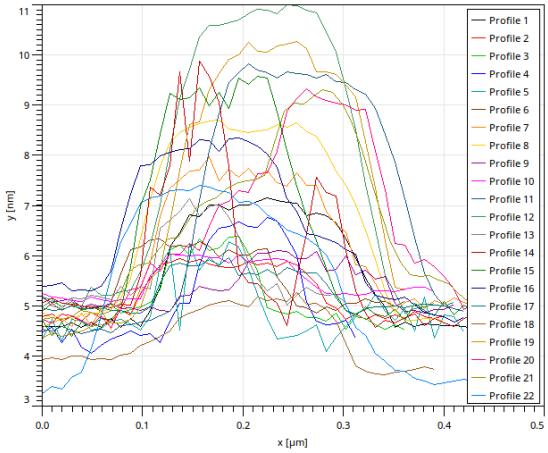

(b) Profiles of single sheets found in (a). All lateral dimensions are smaller than 200 nm and all thicknesses are between 1-6 nm, corresponding to 1-9 layers.

Figure 17: AFM image of spray-deposited MoS_2 nanosheet suspension, with corresponding profiles.

II.2 Thermal stability

Annealing is an important processing step in device fabrication for reducing contact resistance, relieving strain in the film, and in the case of MoS_2 nanosheet suspensions, eliminating contaminants (e.g. stabilizers, surfactants) and potentially improving the interface between adjacent sheets.

Bulk MoS_2 has a decomposition temperature of 1185 °C or higher [72], and single-sheet devices based on mechanically exfoliated MoS_2 have shown thermal stability up to 1100 °C [26]. Nanoscale MoS_2 sheets, on the other hand, are expected to be more sensitive to temperature due to both their high surface area to volume ratio and their extremely small thickness [73].

Bessonov *et al.* [66] used the Langmuir-Blodgett (LB) method to deposit a film of MoS_2 sheets, where each LB film thickness was 20-30 nm and 10-20 LB layers were needed to achieve conformal coating. The top of the MoS_2 layer was then oxidized in air at 150-200°C for 3-10h to obtain a $MoOx/MoS_2$ interface ($x<3$). While partial oxidation of the thick MoS_2 film in the vertically-stacked device architecture in the study of Bessonov *et al.* is desirable, in the case of TFTs such a low oxidation temperature can be detrimental to charge transport due to the low thickness of the films involved.

Thermogravimetric analysis (TGA) (Section II.2.1) records the weight of a sample while annealing at a prescribed temperature profile. TGA is useful for determining decomposition temperature, as well as the onset of oxidation. While pure structural changes in the sample cannot be observed by TGA, the release or uptake of materials to or from the environment are detectable with μg sensitivity. In the case of MoS_2, release of sulphur or uptake of oxygen at elevated temperatures are expected [66]. In this experiment, sulphur loss was indeed confirmed using EDX (Section II.2.2).

The low temperature oxidation (and decomposition) of MoS_2 nanosheets was indeed observed using thermal gravimetric analysis (Section II.2.1) and Raman spectroscopy (Section II.2.4), emphasizing the importance of material characterization for device fabrication.

II.2.1 Thermogravimetric analysis (TGA)

For processing purposes, TGA is useful for determining the critical annealing temperature. A deposited MoS_2 film is expected to lose mass when non-volatile residues from the suspension burn, and when the film itself undergoes decomposition. The film decomposition temperature should obviously be higher than the temperature required to burn any unwanted residues. In the case of MoS_2, changes in mass can be expected to occur due to partial release of sulphur, or oxidation, if annealed in air. If these processes could be localized (e.g. photonic curing through a shadow mask), sulphur depletion could potentially improve the metallic properties of the film due to an increased Mo:S ratio and exhibit lower contact resistance with

source and drain electrodes [74]; localized oxidation could be potentially used as a method to convert the top-most layer of the film to an insulating MoO_x layer for top gate or dual gate structures [66]. However, localized thermal decomposition is beyond the scope of this research. Sulphur loss and oxidation across the entire film would corrupt the semiconducting property of MoS_2.

To study the impact of high temperature annealing on MoS_2 nanosheet films, two temperature profiles were used. For annealing in nitrogen, a temperature profile of 30–800°C with ramps of 10°C/min and isotherms every 100°C was used. For annealing in air, a similar temperature profile was used, but with more isothermal steps in the lower temperature range of 100-400°C (Figure 18). The sample used was the in-house sodium-exfoliated suspension, since the concentration of the commercial suspension is too low to meet the TGA minimum initial sample weight. As a reference, dry MoS_2 micropowder was tested as well.

In inert (nitrogen) environments, the MoS_2 micropowder lost less than 2% of its starting weight (Figure 18e), which can be attributed to trapped humidity and contaminations, while the MoS_2 nanosheets lost 30% of their starting weight, and would have lost more if the last isothermal step lasted longer. The first significant weight loss of the nanosheets sample, around 100°C, is attributed to water and other volatiles, while the second significant weight loss around 400-450°C is attributed to the loss of sulphur. Interestingly, at around 700°C, both the nanosheets and the micropowder samples show a positive weight change in nitrogen environment. The reason for this short period of mass gain is unclear and may be instrument-related, e.g. oxygen contamination (a reaction with nitrogen is unlikely due to the strong $N \equiv N$ bond). Above 750°C, both samples have an increased weight loss rate, suggesting that sulphur is released at an increasing rate. The loss of sulphur with increasing temperature was also confirmed using EDX analysis (Section II.2.2).

The nanosheet sample in air followed very closely the same trend as the sample in nitrogen up to about 300°C, at which point the sample in air started to gain mass. It is suggested that above 250°C a combined process of oxidation and loss of sulphur takes place, and that no oxidation takes place below 250°C due to the close resemblance to the nitrogen sample.

It is therefore evident that annealing should be limited to 400°C in inert atmosphere and to 250°C in ambient atmosphere, to prevent severe changes to the Mo:S ratio. According to DLS results (Section 16), the size of MoS_2 nanosheets in the commercial suspension is even smaller, thus it is expected to have even lower critical temperatures.

These results confirm that the thermal stability of nanosheet materials must be studied prior to annealing. TGA was proven as an effective method for studying thermal stability and should be incorporated in future process development for nanosheet materials.

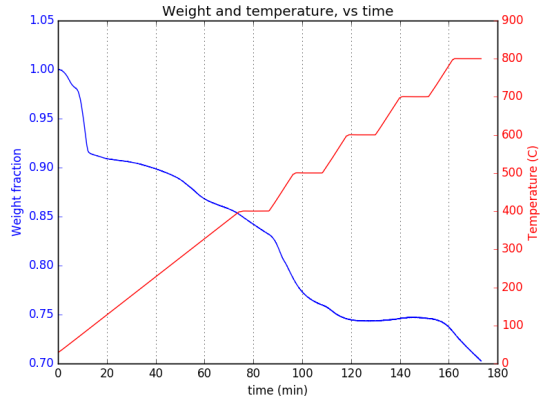

(a) Nanosheets in nitrogen. The first ramp is 5°C/min and all subsequent ramps are 10°C/min; all isothermal steps are 10 min long.

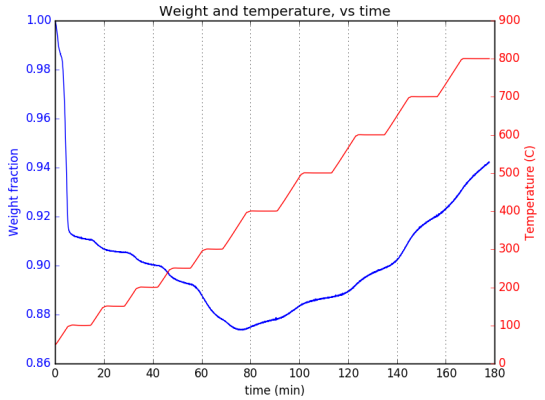

(b) Nanosheets in air. All ramps are 10°C/min; all isothermal steps up to 400°C are 5 min long, and above 400°C are 10 min long.

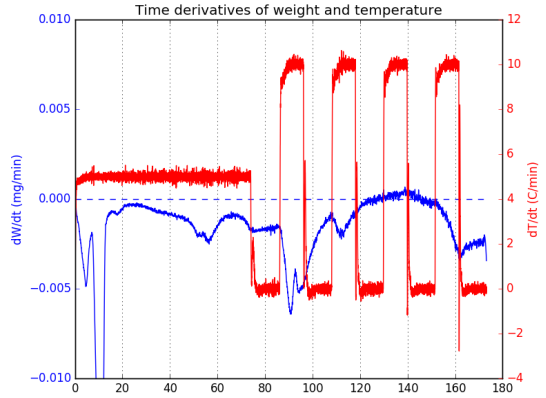

(c) Nanosheets in nitrogen. Time derivatives of plot (a). Weight change is positive between $t = 130 - 150\,\text{min}$ ($600 - 700\,^\circ\text{C}$).

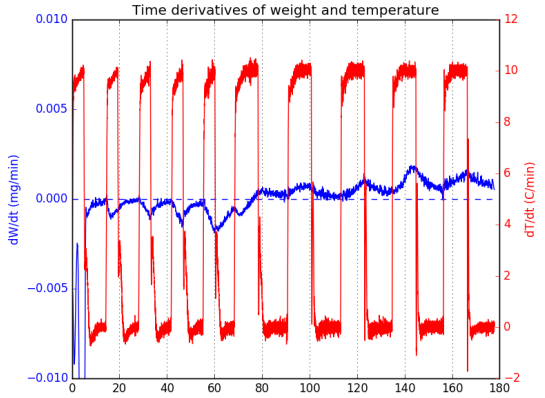

(d) Nanosheets in air. Time derivatives of plot (b). Weight change is positive after $t = 77\,\text{min}$ ($380\,^\circ\text{C}$).

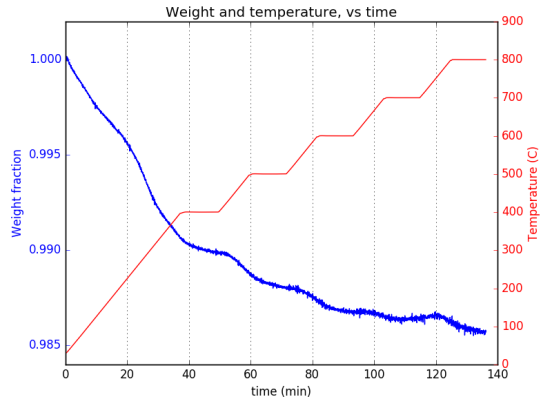

(e) Micropowder in nitrogen. All ramps are 10°C/min and all isothermal steps are 10 min long. Weight change is slightly positive between $t = 110 - 120\,\text{min}$ ($\sim 700\,^\circ\text{C}$).

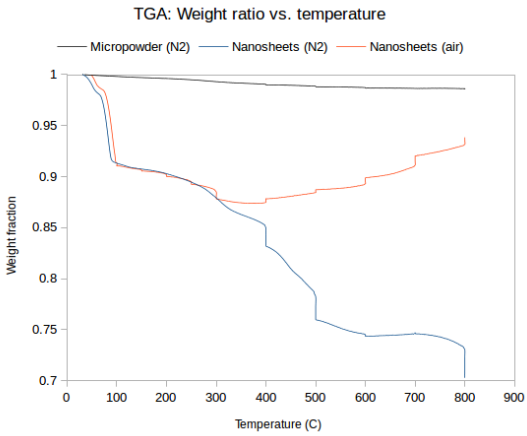

(f) A combined plot of weight ratio vs. temperature (note: temperature profile vs. time differs as per previous figures).

Figure 18: TGA analysis of MoS_2. Comparison between MoS_2 nanosheets (freeze dried own Na-exf MoS_2) in nitrogen (a, c) and in air (b, d), as well as MoS_2 micropowder in nitrogen (e), in a plot of weight fraction (blue) and temperature (red) vs. time. A combined plot of all three vs. temperature is given in (f).

II.2.2 Energy-dispersive X-ray spectroscopy (EDX) of baked MoS_2

The Mo:S ratio of MoS_2 films after baking needs to be measured to confirm changes in film composition, as was hypothesized from the results obtained by TGA analysis. EDX analysis provides the elemental composition of a sample by measuring the emission of the sample as a response to X-ray excitation. Two sets of drop-casted samples of the commercial MoS_2 suspension were put into a furnace: an as-received suspension and a 0.45 μm-filtered suspension, which was also stabilized by 0.1% v/w ethyl cellulose, as suggested in the literature [34]. The MoS_2 suspensions were drop-casted on HMDS-treated SiO_2/Si substrate. Drop volume was fixed to 10 μL using a micropipette, and the diameter of the droplets on the surface was around 5 mm. The droplets were dried at room temperature. Annealing at various temperatures lasted for 30 minutes under nitrogen flow.

From the optical micrographs (Figure 19) it appears that the substrate surface coverage is reduced and aggregation is increased as annealing temperature is increased. This can be attributed to the decomposition of MoS_2 at elevated temperatures, as suggested by the TGA analysis. In addition, filtering the suspension with a low pore size filter significantly reduced agglomeration, suggesting that there is a threshold for the sheet size under which agglomeration does not nucleate and grow.

Instead of the stoichiometric ratio Mo:S 1:2, EDX measurement of pristine MoS_2 nanosheet yields 1:4, underestimating Mo content. However, samples annealed at elevated temperatures show an even higher Mo:S ratios (Table 6), indicating that the overall trend supports the theory of S departure.

In samples with ethyl cellulose, a carbon peak is present at 450°C but not at 750°C. This observation suggests that ethyl cellulose residues do not fully decompose at annealing temperatures below ~500°C and that therefore using EC as a stabilizer should be minimal or completely avoided to eliminate contaminants in the film.

At the highest temperature, 750°C, several highly concentrated areas were slightly conductive, with $0.5 - 10\,\mathrm{M}\Omega$ across 1 mm (measured with DMM), suggesting an increased Mo:S ratio.

The observed reduction in Mo:S ratio is a sign of pyrolysis, which may result in areas of nanocrystalline Mo-S structures. In order to confirm such structures are theoretically feasible, a genetic algorithm approach for energy minimization was employed (Appendix B). Stable crystalline structures with various Mo:S ratios were found. The general trend shows increased stability with increased Mo:S ratio (Figure 20), suggesting that crystalline structures with reduced sulphur content are energetically favourable. This could explain the loss of sulphur observed in EDX measurements. In-depth exploration of such structures, both numerically and experimentally, is beyond the scope of this thesis.

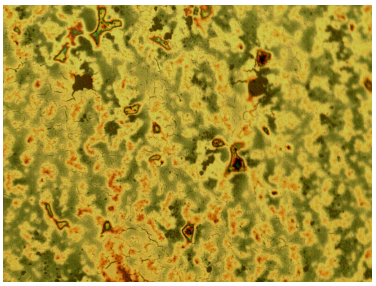

(a) 450°C, with EC.

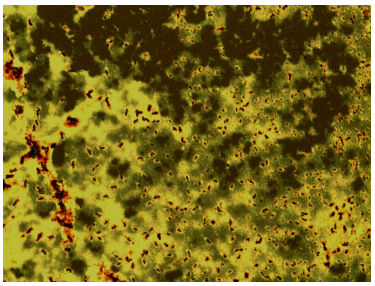

(b) 450°C, without EC.

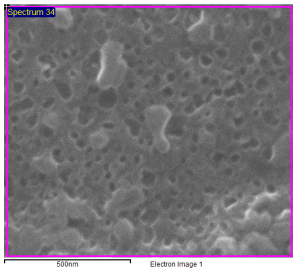

(c) 450°C, without EC; Mo:S 1:6.

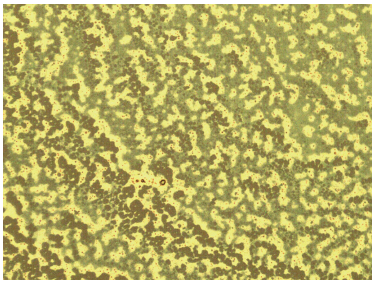

(d) 550°C, with EC.

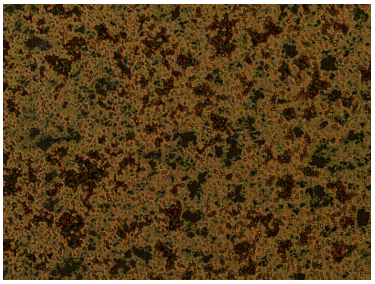

(e) 550°C, without EC.

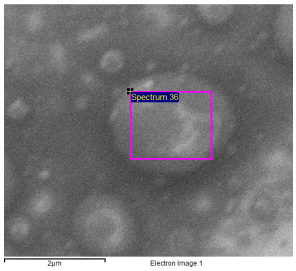

(f) 550°C, without EC; Mo:S 27:1.

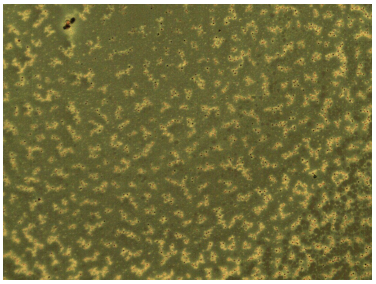

(g) 650°C, with EC.

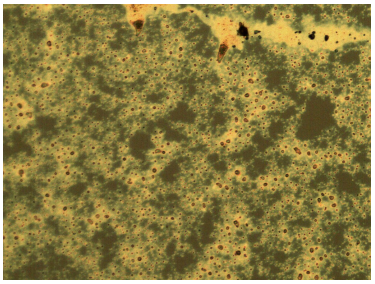

(h) 650°C, without EC.

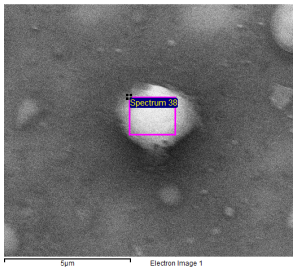

(i) 650°C, without EC; sulphur peak not recorded.

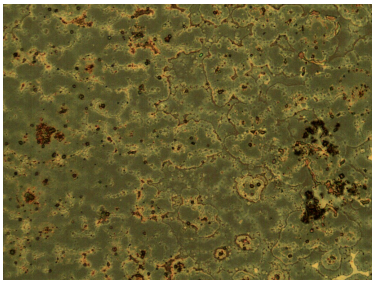

(j) 750°C, with EC; slightly conductive.

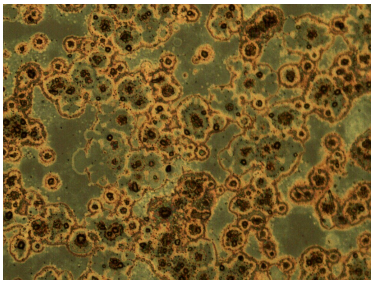

(k) 750°C, without EC; slightly conductive.

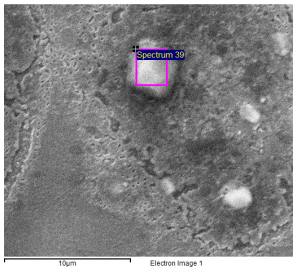

(l) 750°C, without EC; Mo:S 14:1.

Figure 19: Optical microscope (two left columns) and SEM/EDX (right column) images of baked MoS_2 samples under nitrogen flow. All optical micrographs are 1 mm side to side. SEM images are for the samples without ethyl cellulose (EC). The magenta frame represents the area rastered by EDX measurement (Table 5).

Table 5: Detailed EDX results for MoS_2 aggregates (without EC).

450°C

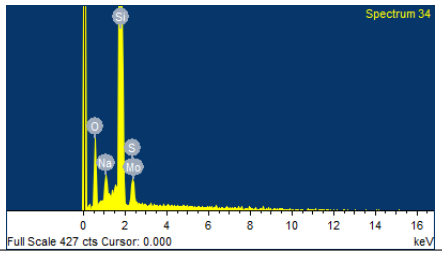

Element	Weight %	Atomic %
O K	17.11	26.72
Na K	1.00	1.08
Si K	79.49	70.73
S K	1.60	1.25
Mo L	0.81	0.21

550°C

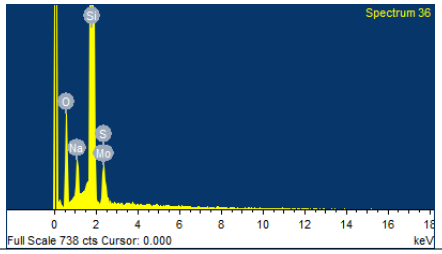

Element	Weight %	Atomic %
O K	19.51	30.93
Na K	1.40	1.55
Si K	72.94	65.86
S K	0.08	0.06
Mo L	6.07	1.60

650°C

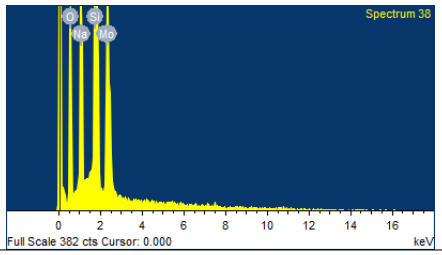

Element	Weight %	Atomic %
O K	27.18	43.13
Na K	6.90	7.62
Si K	49.77	44.98
Mo L	16.14	4.27

750°C

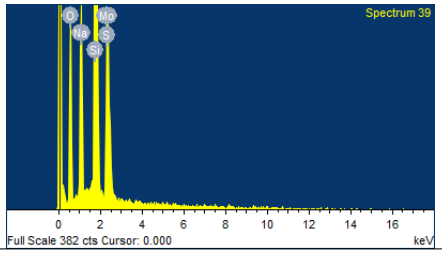

Element	Weight %	Atomic %
O K	29.18	46.07
Na K	6.73	7.39
Si K	46.32	41.65
S K	0.42	0.33
Mo L	17.35	4.57

Table 6: Summary for EDX and Raman analysis of baked MoS_2 nanosheets (without EC). Here, "aggregates" stand for distinct solids of MoS_2, while "background" is a more uniformly-appearing layer formed by extremely small sheets.

Method	Morphology	Pristine	450°C	550°C	650°C	750°C
EDX Mo:S ratio	Background	1:4	1:6	no sulphur	no sulphur	no sulphur
	Aggregates		1:6	27:1	n/a	14:1
Raman peaks present	Background	yes	no	no	no	no
	Aggregates	yes	yes	yes	broad peaks	no, or E^1_{2g} only

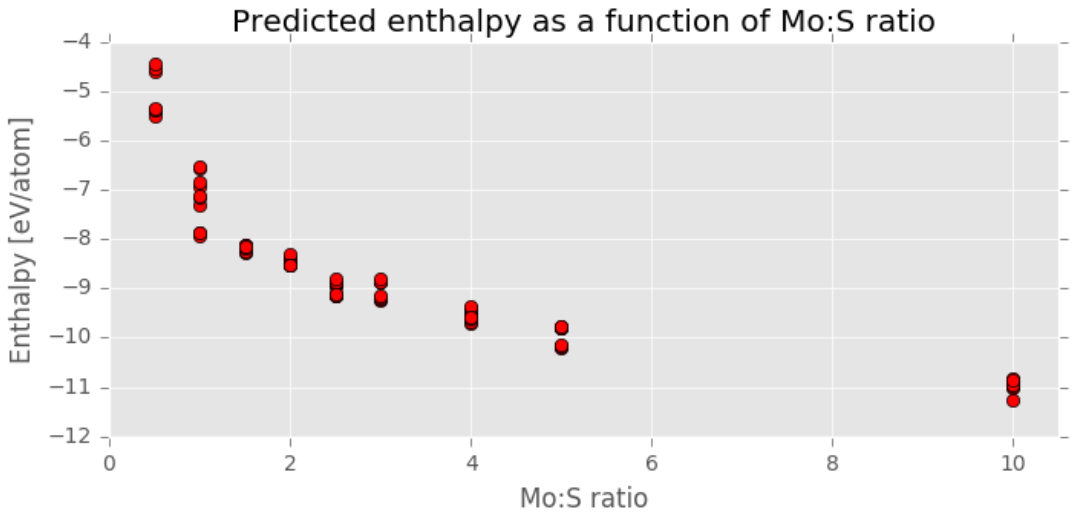

Figure 20: Unit cell enthalpy as a function of Mo:S ratio. Lower enthalpy indicates increased stability. The results were obtained by Virtual NanoLab's Crystal Structure Prediction genetic algorithm [7].

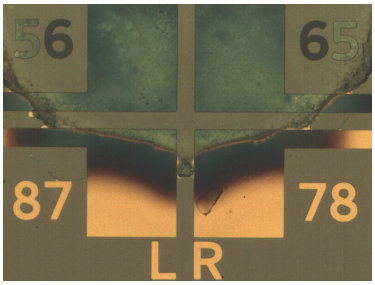

(a) change of surface colour of chromium in the area of deposition.

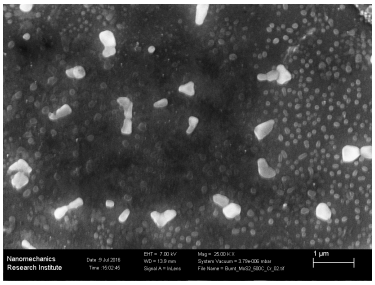

(b) on thermal oxide.

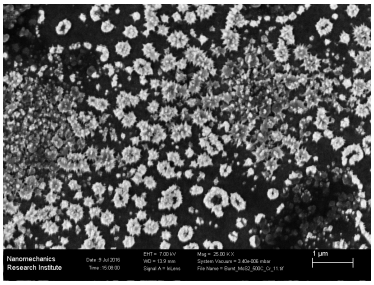

(c) on chromium ("spiky" spheres).

Figure 21: Optical (a) and SEM (b, c) images of drop-casted MoS_2 nanosheets on SiO_2 and Cr (chromium oxide, actually) annealed at 500°C in argon atmosphere for 30 min.

II.2.3 Annealing on chromium

In another annealing experiment of MoS_2 nanosheets at 500°C on chromium, the deposited MoS_2 film had a reaction with the chromium (Figure 21), both in nitrogen and in argon atmospheres. Using Raman spectroscopy it was revealed that no MoS_2 peaks could be found on top of the chromium; however, low-intensity, wide peaks were observed on the thermal oxide. This finding suggests that the MoS_2 nanosheets were partly decomposed on the thermal oxide, and fully decomposed or reacted on the chromium. Interestingly, the chromium substrate caused the MoS_2 to morph into "spiky" spheres, as was observed by SEM (Figure 21c). This finding limits the annealing temperature of devices with chromium contacts.

II.2.4 Effect of low-temperature annealing in air

The ability to anneal in air greatly simplifies processing complexity. In order to confirm that MoS_2 nanosheet film can be safely annealed in air at low temperatures, a study of the change in the intensity of the Raman peaks as a function of annealing temperature was carried out. The commercial MoS_2 nanosheet suspension was spray-coated on a $20\,mm^2$ SiO_2 substrate for 3 minutes at a flow rate of $1\,\mu L \cdot s^{-1}$ and annealed at temperatures of 75-400°C for 5 minutes. The use of spray coating ensures the same MoS_2 surface density is deposited on both the SiO_2 and Cr areas. Raman spectra in the range 350-430 cm^{-1} were collected at 5 random points for each annealing temperature for MoS_2 on SiO_2 and on Cr. The results are presented in Figure 22. As can be seen in the optical micrographs, the apparent film density significantly reduces even after a 150°C anneal, which can be attributed to volatile residues.

The relative intensity of the characteristic peaks after annealing in temperatures of 200°C and higher (Figure 22ca) suggest that the MoS_2 content is compromised at such temperatures. Similarly, a significant drop in peak area is observed at 300°C and higher (Figure 22cb). Interestingly, annealing at up to 200°C reduced the spread in peak intensity, peak area and the peak and area ratios (Figure 22cc), suggesting that annealing at 150-200°C may improve film uniformity. The difference in peak positions (less than 24 cm^{-1}) for temperatures under 250°C (Figure 22cd) suggests that the nanosheet film is mainly comprised of sheets with thickness of up to 5 layers (Table 2). Higher apparent peak position differences after higher annealing temperature are artifacts due to the distortion in characteristic peaks induced by MoS_2 degradation. A thickness of around 5 layers is in agreement with AFM measurements (Figure 17).

Comparison between MoS_2 on SiO_2 and Cr reveals that while the apparent initial and final film densities are similar on both surfaces, the characteristic peak intensity and peak ratio of MoS_2 nanosheets on Cr is significantly lower even at temperatures as low as 150°C. This observation suggests that a reaction between MoS_2 and Cr in air takes place at low temperatures.

In conclusion, the result of this study confirms that the sheet thickness is largely limited to 5 layers and suggests that annealing of MoS_2 nanosheet films in air may have a positive influence on film uniformity, but should be limited to 150°C. Therefore, if devices with a 150°C air-annealed film would exhibit metallic properties (1T phase), additional annealing step in an inert atmosphere at up to 300°C can be attempted to induce 1T to 2H relaxation. However, due to the smaller sheet size this transition may occur at lower temperatures. For bottom-contact devices with Cr electrodes, annealing should be limited to below 150°C. Further studies of MoS_2 thermal stability on additional metals are needed. Based on EDX and TGA analysis, MoS_2 at the metal-semiconductor interface in top-contact devices with Cr electrodes cannot be assumed thermally stable up to 500°C, even in the absence of air. Ideally, deposition of Cr should be done

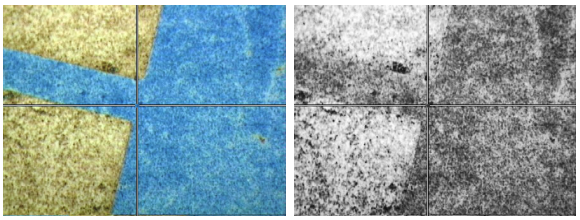

(a) After 5 min at 75°C (left: original; right: retouched).

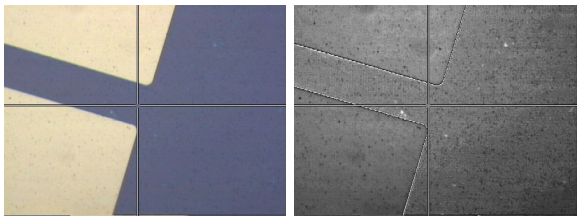

(b) After 5 min at 350°C (left: original; right: retouched).

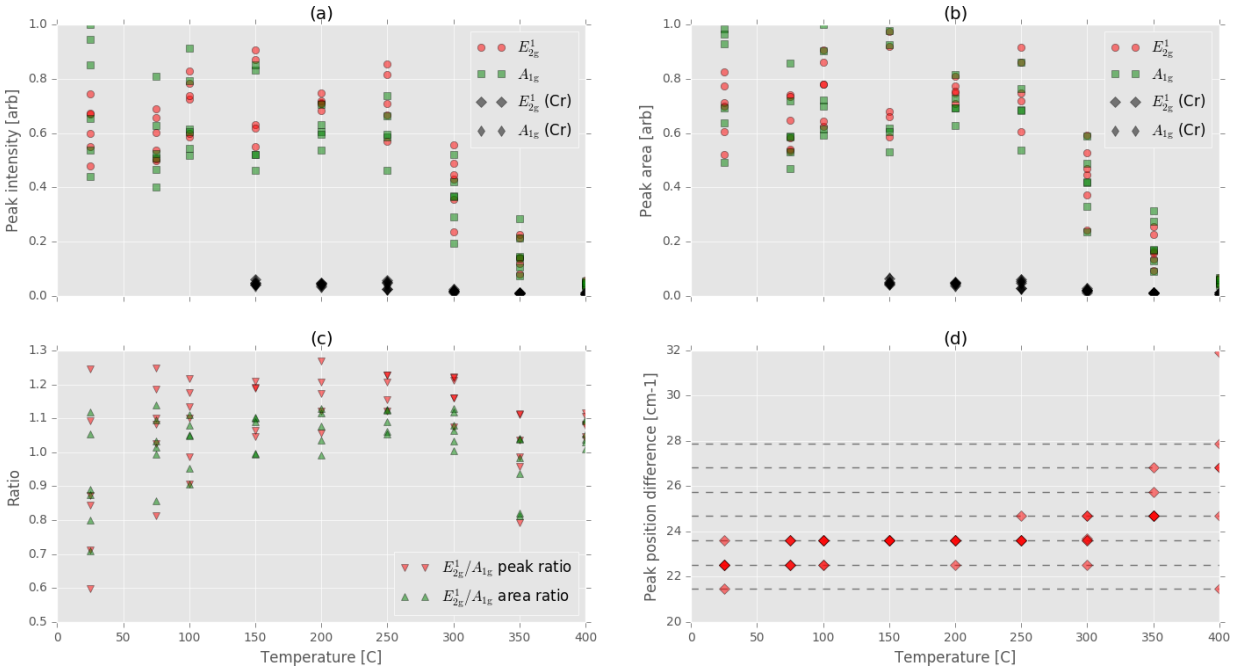

(c) Raman characterization of air-annealed MoS_2 nanosheet film. All data was collected from the same sample after various annealing temperatures. Soak time at target temperature was 5 min. Peak intensity and peak area of MoS_2 on Cr are shown for 150°C and higher, and are significantly lower than on SiO_2.

Figure 22: Optical micrographs and Raman characterization of spray coated MoS_2 nanosheets annealed in air on SiO_2 and Cr. Film morphology is better visualized in the retouched images.

after the MoS_2 annealing steps are completed. A potential approach for oxidation prevention in future research could be encapsulating a device prior to annealing.

Part III

Device fabrication

As mentioned above, the purpose of the MoS_2 film is to transport charge between the source and the drain electrodes in a thin-film transistor configuration. In order to do so, methods for the deposition of continuous MoS_2 films were developed (Sections III.3-III.4).

Fabrication of electronic devices with 2D materials using mechanical cleavage exfoliation is limited to extremely low yield and suffers from inconsistent sheet sizes and thicknesses, as well as unpredictable patterning. Obtaining single (or few) layer sheets is therefore desirable *prior* to deposition. This can be achieved using liquid-phase exfoliation, and solution-processable MoS_2 is therefore key for fabricating large-area electronic devices. However, current liquid-phase exfoliated sheets are nanoscale in size and are too small to bridge a typical channel gap between two electrodes ($1 - 10\,\mu$m). As semiconducting nanosheets have high intrinsic mobilities, in films of nanosheet networks spanned across large areas, inter-sheet charge transport processes are the limiting factor [1, 68]. The mechanism dominating inter-sheet electronic transport in nanosheet films is unknown, but an observed decrease in conductivity with decreased temperature suggests thermally activated inter-sheet hopping [1]. An ideal deposition method would allow packing the sheets in tightly packed tiles. Therefore, it is necessary to develop deposition techniques for obtaining a continuous film of percolating sheets in desired locations, ideally with high uniformity. This can be achieved: using drop-casting (Section III.3), which is convenient for fast prototyping; using inkjet printing (Section III.4), which is ideal for patterning small scale features; or using spray deposition (Section IV.2.3), which is convenient for large-area deposition using small droplets but the degree of control over the process is limited. All three approaches allow fabrication across a large area using liquid suspensions.

Mechanically exfoliated sheets were shown to have exceptional optoelectronic, electrochemical and mechanical properties. While numerous publications demonstrated the fabrication of mechanically exfoliated graphene-based [75] and MoS_2-based [76] TFTs, there was no record to be found of TFTs fabricated from graphene or MoS_2 *nanosheet* suspensions. To the best of my knowledge, a field effect was not yet observed in percolating nanosheet films,[13] and there is currently no theoretical prediction for the presence or absence of semiconductivity in percolation networks, large or small. On the other hand, printing *electrodes* using 2D layered materials is quite common [36, 37, 47]. Therefore, developing better recipes for ink formulation and device processing is crucial to the study of these materials.

[13] As mentioned earlier, a field-effect was recently demonstrated for MoS_2 nanosheet films, but only with electrolyte gating and large sheet sizes (lateral size larger than 300 nm).

III.1 Device architecture considerations

Among the four typical TFT architectures (Figure 2), the use of bottom gate architecture is most advantageous. Since nanosheet MoS_2 films are delicate, subsequent processing steps after MoS_2 deposition, which are required in top gate architectures, could potentially harm the physical or chemical integrity of the film. MoS_2 deposition on bottom gate architectures is either the last or the second last step, which ensures minimal unnecessary alteration between deposition and measurement.

In a bottom gate architecture, a highly doped silicon wafer can function as a common gate and the precisely-grown thermal oxide can function as the gate dielectric, on top of which electrodes are deposited, followed by MoS_2 deposition (bottom contact), or vice versa (top contact). To achieve small and consistent channel lengths, standard lithography processes were used for patterning bottom contact electrodes. For top contact devices, a shadow mask with $50\,\mu$m feature size was used to avoid lithography steps on the MoS_2 film. Special mask layouts were designed to address these different needs (Section III.1.4).

High performance MoS_2 devices are obtained with low Schottky barrier contacts (Section III.1.1), efficient Coulombic screening via high dielectric constant bottom and top gating materials (Section III.1.2), and an optimal thickness of MoS_2 (Section III.1.3) [3]. These considerations are reviewed in the following sections.

III.1.1 Selection of electrode material

The Schottky energy barrier (SB) Φ for charge transport across a metal-semiconductor junction (MSJ) has an impact on the contact resistance of the device. Based on the Schottky-Mott model, the barrier height for electrons Φ_e and holes Φ_h is given as follows:

$$\Phi_e = E_{WF} - E_{EA} \qquad \Phi_h = E_{IE} - E_{WF} \tag{7}$$

where WF, EA and IE are the work function of the metal and the electron affinity and the ionization energy of the semiconductor, respectively (Figure 23a). However, the intrinsic WF, EA and IE quantities of the isolated materials vary upon MSJ formation.

In order to minimize the Schottky barrier (SB) at the metal-semiconductor junction (MSJ), a proper choice of material for the electrodes is needed. While in the ideal Schottky-Mott case $|{}^{d\Phi}/_{dE_{WF}}| = 1$, in reality it was shown experimentally by Das *et al.* [18] that for junctions between common metals and MoS_2, $|{}^{d\Phi}/_{dE_{WF}}| \approx 0.1$, i.e. the Schottky barrier Φ is almost insensitive to the work function of the metal due to Fermi level pinning of the metal to a certain energy level in the semiconductor band gap [77]. Several

models have been suggested to explain Fermi level pinning in 2D semiconductors: metals-induced gap states, interface charge redistribution and interface defects introduced during processing [77, 78].

Liu *et al.* [77] showed that the Fermi level pinning is weak for 2D metal-2D semiconductor junctions and that the Schottky barrier height can be tuned by using different 2D metals, which follow the Schottky-Mott model with $|{}^{\mathrm{d}\Phi}/_{\mathrm{d}E_{\mathrm{WF}}}| \approx 1$. In particular, their calculations for monolayer materials suggest that N-doped graphene and H-NbS_2 are promising electrodes for low Φ_e and Φ_h contacts with MoS_2, respectively (Figure 23b). However, deviations from those calculations in experiments and other practical difficulties have been observed with 2D metals [77], impeding their use in practical applications: sufficient doping levels of graphene for the use of low Φ_e electrode have not yet been achieved; while bulk NbS_2 is metallic, few-layer NbS_2 is semiconducting, possibly due to surface defects; work function differences of tens of meV were observed between monolayer sheets and few-layer sheets, suggesting that the performance of a polydisperse nanosheet suspension would deviate in an unpredictable way from current theory; the use of 2D metals would require encapsulation to prevent oxidation in an ambient atmosphere; a 3D metal would need to be deposited on the 2D metal to connect to external circuitry.

The issues identified suggest that for practical reasons 3D metal electrodes with sufficiently low Φ to MoS_2, such as aluminium (Figure 23b), would be a more straightforward approach. Das *et al.* [18] showed experimentally that scandium contacts provide the best carrier injection with MoS_2, followed by titanium, both with $\Phi_e < 0.05\,\mathrm{eV}$. The vast majority of published works on MoS_2 report either Cr/Au or Ti/Au metal pairs for source/drain electrodes. The chromium or titanium function as an adhesion layer for the gold, as well as an ohmic contact due to the low workfunction-electron affinity mismatch between the metal and MoS_2, and the gold layer functions as a stable, non oxidizing metal. While Das *et al.* did not report results for chromium or aluminium, the trend-line they obtained for Φ_e vs. E_{WF} suggests that potentially $\Phi_e \approx 0.11\,\mathrm{eV}$ for chromium and $\Phi_e \approx 0.08\,\mathrm{eV}$ for aluminium.

In this work, Cr and Cr/Au have been used as bottom electrodes and Cr and Al have been used as top electrodes. Cr and Al are common metals that offer adequate performance and are convenient to process. The use of gold is more restrictive as most silicon labs prohibit its use in vacuum processes. However, as MoS_2 reacts with Cr at elevated temperatures (Section II.2.3), this limits the use of Cr in bottom contact devices to low temperature annealing processes only.

III.1.2 Selection of substrate material

As described earlier, high contrast of MoS_2 can be achieved on 100 nm SiO_2/Si wafers, which are commercially available. The high dielectric strength of SiO_2 and its high thermal stability, together with a

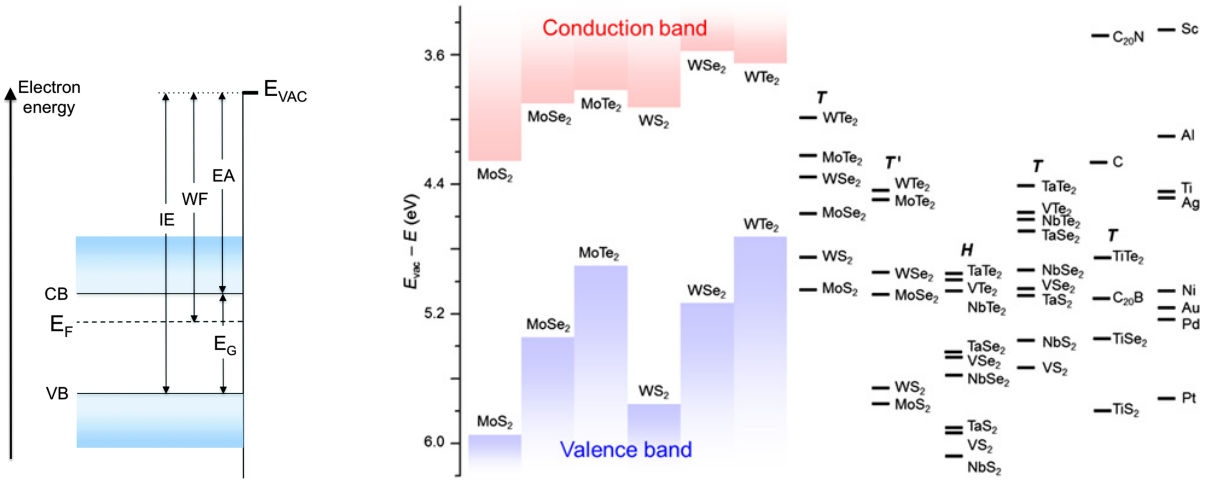

(a) Energy diagram of a surface region of a semiconductor (flat bands condition), including ionization energy (IE), electron affinity (EA) and work function (WF); CB and VB stand for conduction band and valance band, respectively. Reproduced from [79] with permission from The Royal Society of Chemistry.

(b) Calculated band alignment diagram between 2D semiconductors, 2D metals and common 3D metals [77] (Copyright © 2016, The Authors). On the left side, the EA and IE are shown for monolayer 2D semiconductors; on the right side, the WF of for common 3D metals and monolayer 2D metals for different phases (T, T', H) are shown (WF of Cr, 4.6 eV, and Al, 4.06-4.26 eV, are not shown). C_nX stands for X-doped graphene C/X ratio of n:1.

Figure 23: Terminology of band diagrams (a) and Band alignment diagram for MoS_2 and other relevant materials (b).

highly doped Si back gate, make SiO_2/Si an ideal substrate for prototyping bottom gate MoS_2 devices. Moreover, Bao *et al.* [80] showed that MoS_2 sheets on SiO_2/Si substrates are unipolar n-type, suggesting that a good semiconductor-insulator interface is attainable with SiO_2.

SiNx/Si substrate was tested too, as its surface energy does not require pre-treatment prior to deposition (Table 4), and as MoS_2 has good visibility on SiNx. However, the usability of SiNx is limited to low temperature processing due to its thermal stability limitation. If a 300°C anneal of the MoS_2 film would be required for metal-to-semiconductor relaxation, the insulating nitride layer may be compromised. Therefore, a SiNx substrate can be used for prototyping as-deposited films but not for supporting thermal processing of the films.

III.1.3 Channel thickness considerations

The thickness of the MoS_2 layer has an important role in switching behaviour. Bao *et al.* [80] showed that mechanically exfoliated MoS_2 on PMMA/SiO_2/Si substrate exhibit n-type unipolar behaviour for 1.5 nm thick sheet, ambipolar behaviour for 6.5 nm and 47 nm thick sheets, and bulk conductance with no off-state for 80 nm thick sheet. In order to avoid bulk conductivity in fabricated devices it would be necessary to

form continuous films with low enough thickness. Based on the observation made by Bao *et al.* , $\sim 50\,\mathrm{nm}$ would be a first order approximation of the maximal thickness to aim for. However, the study of Bao *et al.* focused on single-crystal MoS_2 devices, while here the films are comprised of percolating nanosheets with approximate sheet thickness of 5 layers. Therefore, the film thickness limit for nanosheet films may vary.

The primary parameter controlling the deposited film thickness was the number of subsequent depositions. In devices exploiting the ring-stain effect, both the number of depositions and the thickness of the ring-stain influenced on the film thickness. It was expected to see an increasing response (current) with increasing thickness but no such response was observed even for the thickest films deposited (Section III.3.3).

III.1.4 Mask design

In order to measure the electrical properties of deposited films, electrodes must be patterned. Inkjet-printing is a convenient mask-less deposition method for large channel, top-contact silver electrodes. For depositing metals other than silver and for obtaining consistent and well-defined arrays of channels shorter than $50\,\mu\mathrm{m}$, vacuum deposition is more convenient, especially for the initial phase of device fabrication.[14]

Vacuum deposition of metals involves the use of shadow masks or photomasks for patterning. Mask layouts were designed for transmission line method (TLM) measurements of contact resistance and for 4-point probe measurements of film sheet resistance (also known as 4-terminal sensing, or 4T).

For the contact resistance measurement via TLM, metal pads of various channel lengths L are patterned and the measured resistance R_{tot} is plotted against L. Extrapolating to $L = 0$ gives the total contact resistance $2R_{\mathrm{c}}$ and the slope gives the sheet resistance R_s:

$$R_{\mathrm{tot}} = R_{\mathrm{ch}} + 2R_{\mathrm{c}} = \frac{\rho}{t}\frac{L}{W} + 2R_{\mathrm{c}} = R_s\frac{L}{W} + 2R_{\mathrm{c}} \tag{8}$$

$$R_{\mathrm{tot}} \xrightarrow[\text{extrap.}]{L\to 0} 2R_c \qquad \frac{\partial R_{\mathrm{tot}}}{\partial L} = \frac{R_s}{W} \tag{9}$$

where W is the channel width (which is kept constant) and t and ρ are the film thickness and resistivity, respectively.

For an accurate measurement of sheet resistance, a co-linear 4-point probe measurement can be used [81]. Four probes separated by an equal distance from each other are patterned, a current I is sourced through the outer probes and the voltage V across the two inner probes is measured. The sheet resistance

[14] The majority of this research involved prototyping on bottom contact devices, for which vacuum deposition is more advantageous.

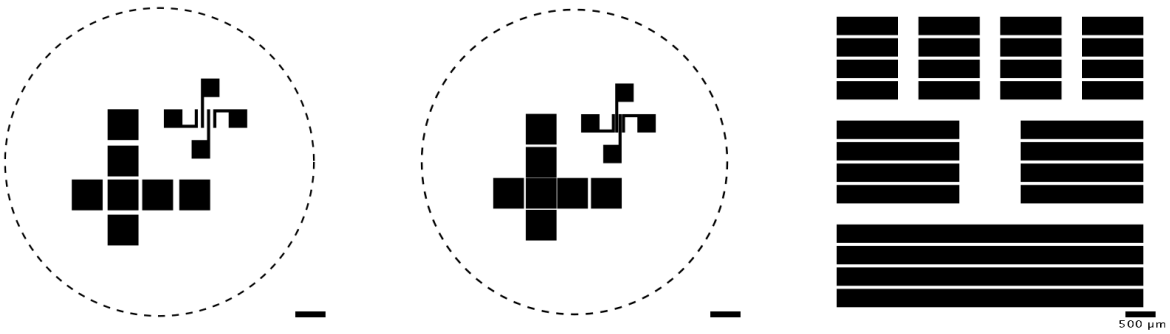

(a) Shadow mask layout of TLM and 4T patterns. Channel lengths are $50-100\,\mu$m.

(b) Lithography mask layout of TLM and 4T patterns. Channel lengths are $5-50\,\mu$m.

(c) Lithography mask of an array of devices with increased W/L ratio. Channel widths are $1-5$ mm. In this image, the channel length is $50\,\mu$m (the complete mask includes channel lengths of $5-50\,\mu$m).

Figure 24: Mask layouts for top/bottom contact device architecture for electrical characterization of deposited films using rectangular devices. All scale bars are $500\,\mu$m wide. The dashed circular contours in (a) and (b) represent a 5 mm diameter drop-casted droplet.

is then calculated as follows:[15]

$$R_s = \frac{\rho}{t} = \pi \frac{V}{I} \left[\ln \frac{\sinh\left(\frac{t}{s}\right)}{\sinh\left(\frac{t}{2s}\right)} \right]^{-1} \xrightarrow{t \ll s} \frac{V}{I} \frac{\pi}{\ln 2}. \tag{10}$$

III.1.4.1 Shadow mask for top contact electrodes

A shadow mask was designed with TLM channel width and lengths of $500\,\mu$m and $50-100\,\mu$m, respectively, and 4T separation length of $50\,\mu$m (Figure 24a). The mask was laser-cut in a 0.3 mm thick steel plate, 3 inch in diameter,[16] for the primary purpose of e-beam evaporation of top contact electrodes on drop-casted or spin-coated films (Section III.3). For drop-casted films, the patterns were designed to have sufficient clearance from the ring-stain of a 10 pL water droplet (ring-stain diameter of around 5 mm on SiO_2), as well as sufficient margin for alignment error.

III.1.4.2 Lithography mask

Various electrode patterns were designed for characterizing thin films with channel lengths of down to $5\,\mu$m, which is substantially smaller than the feature size limit of shadow masks. TLM and 4T patterns similar to the shadow mask but with smaller channel length were designed to minimize inter-sheet transport events

[15] 4-point probe measurement is used for accurate measurement of resistance below 100 ohms. It was only later discovered that the resistance of nanosheet MoS_2 is much higher.

[16] The mask was fabricated by KJ Laser Micromachining, Toronto.

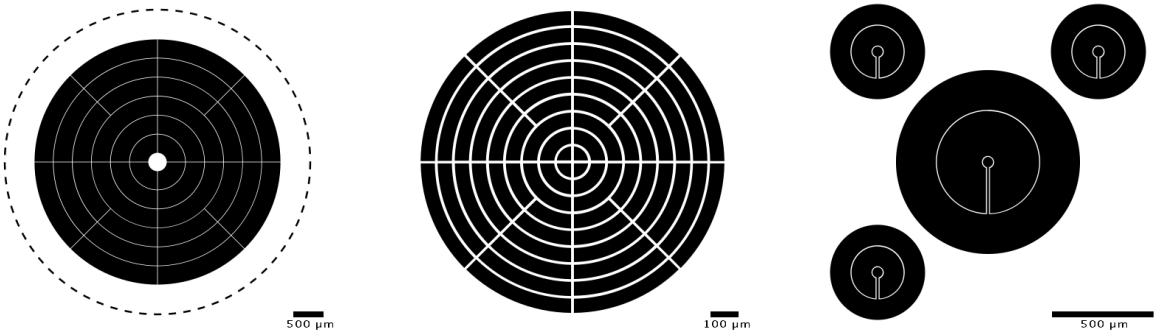

(a) 10 μm channel length concentric patterns (the mask layout also includes 5 μm channel length patterns). The dashed circular contour represent a 5 mm diameter drop-casted droplet.

(b) 10 μm channel length concentric patterns (the mask layout also includes 5 μm channel length patterns) for large inkjet printed volumes. The entire pattern is 1 mm side to side.

(c) 5 μm channel length circular patterns for small inkjet printed volumes, with convenient probing access.

Figure 25: Lithography mask layouts for bottom contact device architecture for electrical characterization of deposited films using circular devices, exploiting the ring-stain effect.

and thus reduce the channel resistance (Figure 24b).

Initial measurements showed that the channel resistance was very high. Therefore, arrays of mm-wide channel width electrodes were designed to reduce the channel resistance (Figure 24c). The wide channel patterns actually offer higher flexibility for printed devices because the actual channel width is determined by the printing process. Channel widths as small as a single droplet diameter are possible, if needed (Section III.4).

Finally, circular devices were designed to exploit the ring-stain effect for device fabrication (Section III.4.3). The contact line of drop-casted (Figure 25a) or printed (Figures 25b, 25c) droplets is pinned precisely at the channel gap due to surface energy differences between the metal and insulator. During the drying of the droplet, suspended sheets are transported towards the contact line, which forms a continuous film between the electrodes. To the best of my knowledge, this is the first report of circular devices designed to exploit the ring-stain effect.

III.2 Evaluation of the minimal concentration and volume for obtaining continuous films

In order to obtain a continuous film, a critical mass of nanosheets needs to be deposited onto a confined area. In the case of drop-casting or inkjet printing, the total deposited nanosheet mass depends on the droplet volume, the concentration of the suspension and the number of deposited layers (deposited after the drying of the previous layer). The resulting surface density of MoS_2 in the area confined by the droplet geometry also depends on the contact angle (Section I.3.2.1). A lower contact angle would result in a lower surface density than a higher contact angle for the same volume and concentration due to the longer base diameter. A hydrophobic coating, for example, would increase the surface density in the interior of a dried droplet because the same volume would now dry onto a smaller area.

However, a too high surface density, such as in the case of thicker films, could give rise to bulk conductivity in the film that the applied gate voltage would not be able to modulate. It is therefore important to calculate the minimal volume or concentration required to obtain continuous thin films. The calculation of two limits are presented here: (1) complete uniform coverage of the deposited area (Section III.2.1), and (2) the coverage at the onset of percolation (Section III.2.2). The results of these calculations are then used as a guideline for device fabrication (Sections III.3, III.4).

III.2.1 Uniform film approximation

In this approximation, the deposited film fully covers the target area with a single-sheet thick film. This approximation is equivalent to a structured grid of uniform square sheets perfectly aligned side-by-side across the whole area.

To evaluate mass-related quantities, the surface density ρ_{2D} of monolayer MoS_2 is needed. It can be extracted either from the theoretical unit-cell, where two Mo and four S atoms occupy a rectangular cell with side lengths $a = 5.47\,\text{Å}$, $b = 3.16\,\text{Å}$, yielding $\rho_{2D,uc} = 3.073\,\text{mg}\cdot\text{m}^{-2}$, or from the bulk density $\rho_{3D} = 5.06\,\frac{\text{g}}{\text{cm}^3}$ and the Van der Waals gap of MoS_2, $d_{vdW} = 650\,\text{pm}$, yielding $\rho_{2D,blk} = \rho_{3D}\cdot d_{vdW} = 3.289\,\text{mg}\cdot\text{m}^{-2}$. In this section the unit-cell-based value is used.

III.2.1.1 Perfect uniform film

In the case of a uniform film of monolayer MoS_2, assuming a droplet of volume V_d dries into a circular stain with diameter d_d (and corresponding area A_d), the minimal MoS_2 nanosheet concentration in suspension

must be:

$$c_{\min} = \frac{\rho_{2D} \cdot A_d}{V_d} = \rho_{2D} \frac{\pi}{4} \frac{d_d^2}{V_d}. \tag{11}$$

In typical drop-casting, $V_d = 10\,\mu$L and $d_d = 5\,$mm, such that $c_{\min} = 6.034\,\text{mg} \cdot \text{L}^{-1}$. A more conservative approximation, assuming average MoS_2 sheet thickness of 5 layers, would be $c_{\min} \sim 30\,\text{mg} \cdot \text{L}^{-1}$. Since the measured concentration of the commercial MoS_2 suspension is approximately $1\,\text{mg} \cdot \text{L}^{-1}$, around 30 subsequent depositions would be required to obtain a uniform film (assuming ideal, uniform film without ring-stain effect).

III.2.1.2 Perfect ring-stain

If, on the other hand, during the drying of the same droplet volume, all of the suspended MoS_2 is transported towards the contact line to form a uniform ring-stain of thickness $L = 40\,\mu$m (typical ring-stain thickness for $10\,\mu$L droplets), the minimal MoS_2 concentration to obtain a continuous film along the ring-stain alone reduces to:

$$c_{\min} = \frac{\rho_{2D} \cdot \frac{\pi}{4} \left[d_d - (d_d - 2L)\right]^2}{V_d} = \frac{\rho_{2D} \cdot \pi \left(d_d L - L^2\right)}{V_d} = 0.192\,\text{mg} \cdot \text{L}^{-1} \tag{12}$$

for monolayer MoS_2 and $c_{\min} \sim 1\,\text{mg} \cdot \text{L}^{-1}$ for 5 layer MoS_2. In this case, deposition of a single droplet would suffice. Additional values, for monolayer MoS_2, are given in Figure 26.

The minimal concentration for drop-casted devices in the two extreme cases of perfectly uniform film and perfect ring-stain are 30 and 1 $\text{mg} \cdot \text{L}^{-1}$, respectively. These values can be easily accommodated via subsequent drop-casting. Similar minimal concentrations are expected for inkjet printed devices as well, assuming the contact angle and the ring-stain thickness ratio remain identical in smaller droplets.

III.2.2 Continuum percolation of random size sheets

Percolation theory deals with the statistics of randomly connected clusters. The percolation threshold of a system is the point at which there is a probability of 50% that the connected clusters form a continuous path throughout the system. Unlike in the previous case study of uniform films, in this approximation, the deposited material needs to cover only a fraction of the target area, an area fraction that would guarantee a probability of at least 50% that a continuous path between the source and drain electrodes exists. In traditional percolation computations, such as for conductor-insulator composites, the percolation threshold is of interest for minimizing the volume fraction of the metal content in the composite. The

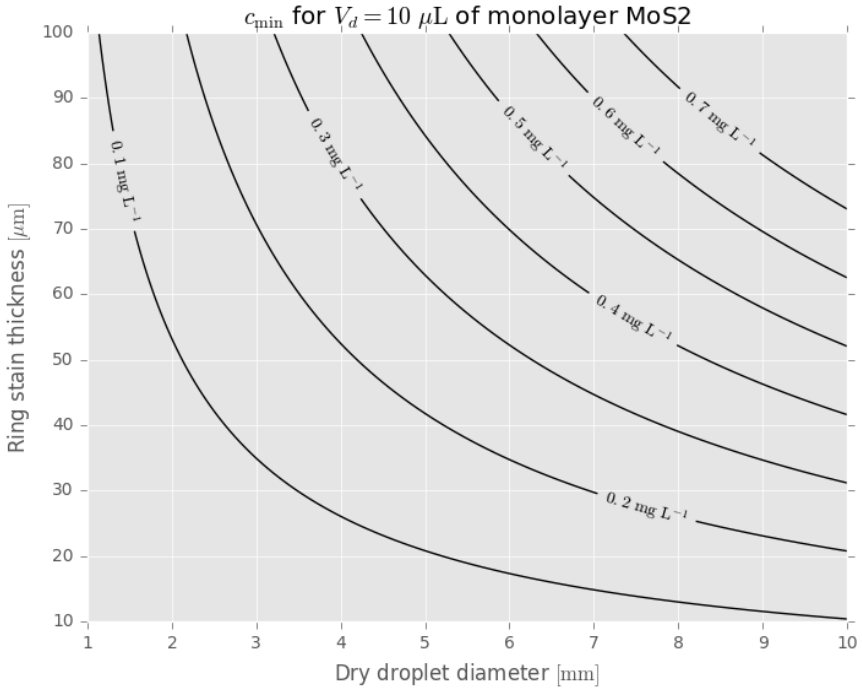

Figure 26: Minimal concentration of monolayer MoS_2 nanosheets in 10 μL droplet to obtain a uniform film, as a function of dry droplet diameter and ring-stain thickness. These ranges are typical for drop-casting using a micropipette.

study of percolation threshold here is applied to areal coverage, also known as continuum percolation, and is used for concentration evaluation.

Unlike in the previous case of a perfectly uniform film, in reality the channel gap does not have to be fully coated for conduction to occur. Moreover, the nanosheets are not uniformly tiled but rather have randomly overlapping areas. In order to determine the minimal concentration required to bridge a channel gap, it is necessary to calculate the percolation threshold for the areal coverage; that is, at what area fraction covered is a percolated network of nanosheets obtained.

III.2.2.1 Brief introduction to percolation theory

In metallic materials, the onset of conductivity is observed at the percolation threshold of the network connecting the two electrodes. A sharp increase in conductivity σ is observed when the volume fraction ϕ exceeds a critical value ϕ_c, given by the power-law relation

$$\sigma \approx \sigma_0 \left(\phi - \phi_c\right)^n \tag{13}$$

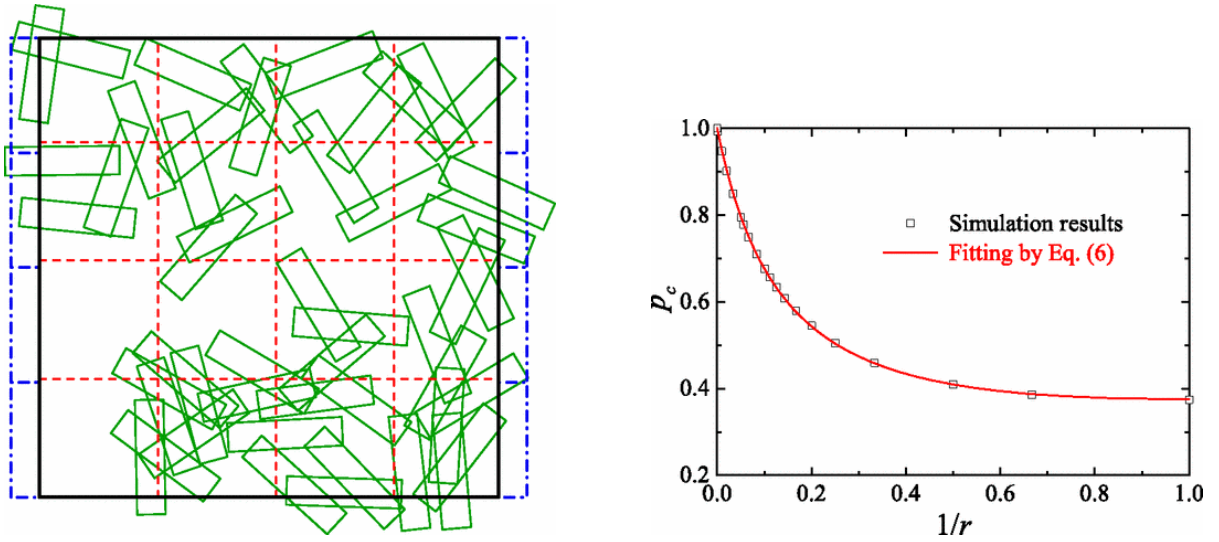

(a) An example of a percolation of homogeneous rectangle with aspect ratio $r = 4$.

(b) The critical *remaining* area fraction for homogeneous rectangle systems of various aspect ratios (for squares, $r = 1$).

Figure 27: Monte-Carlo simulations for a 2D system of percolating homogeneous rectangles [8]. ©2013 American Physical Society.

predicted by percolation theory, with $1.5 < n \lessapprox 11$ and $0 < \phi_c \lessapprox 0.5$, as found experimentally for transport phenomena in various three-dimensional systems [82].

Li *et al.* [34] showed that the conductivity of printed MoS_2 films follows the percolation power law $\sigma \sim (N - N_0)^n$ up to 15 printing passes, where σ is conductivity, N is the number of printing passes, $N_0 \approx 3.6$ and $n \approx 1.7$. After more than 15 passes, the conductivity did not depend on film thickness (Table 3).

In their work on continuum percolation of rectangles, Li and Östling [8] calculated percolation thresholds using Monte Carlo simulations and showed that the critical area fraction p_c is significantly smaller than 1 at percolation threshold (Figure 27b). It turns out that for homogeneous squares ($r = 1$) it would suffice to cover slightly more than 60% to achieve percolation.

The continuity of thin films of nanosheet materials are approximated here by a 2D percolation network. The use of a 2D system is sufficient because percolation in this case is solely determined by the areal coverage.[17] In reality, nanosheet suspensions are comprised of a broad particle size distribution. Theoretical and numerical results for bi-modal to tri-modal rectangle distributions were published [8], but there are no published results for a random distribution of rectangles, which may quantitatively differ from the simpler bi-modal and tri-modal cases. Using DLS results, it is possible to approximate the sheet size distribution

[17]Since the critical transport direction is lateral, from source to drain, even if the channel was formed by nanoflakes dispersed inside a supporting insulating matrix (e.g. a polymer), as long as its thickness is significantly smaller than the channel length and width ($t \ll L, W$), areal coverage would still be an accurate approximation.

and use it in Monte Carlo simulations to calculate the critical covered area fraction for a random particle size distribution.

III.2.2.2 Estimation of percolation threshold for a random particle size distribution

Numerical percolation studies are usually facilitated by geometrical equations to determine overlap with high computational efficiency [8]. In this research, due to time limitations, an image processing approach was taken as this was easier to implement.

For simplicity, the sheets were assumed to be rectangular and all random variables are assumed to be independent. In reality that is not necessarily the case. For example, the deposition location of large sheets in drop-casted films are more likely to be found around the ring-stain, and in the case of spray coating, a higher density is deposited near the centre of the spray. However, in the absence of a better model, this interdependence is neglected. Formation of aggregates due to internal flows during the drying of the droplet is also not accounted for.

A truncated normal distribution ϕ_{trunc} of the form:

$$\begin{cases} \phi(\xi) = \frac{1}{\sqrt{2\pi}} \exp\left(-\frac{1}{2}\xi^2\right) \\ \Phi(x) = \frac{1}{2}\left[1 + \operatorname{erf}\left(\frac{x}{\sqrt{2}}\right)\right] \end{cases} \Rightarrow \qquad \phi_{\text{trunc}}(x; \mu, \sigma, a, b) = \frac{\phi\left(\frac{x-\mu}{\sigma}\right)}{\sigma\left[\Phi\left(\frac{b-\mu}{\sigma}\right) - \Phi\left(\frac{a-\mu}{\sigma}\right)\right]} \tag{14}$$

was chosen for the side lengths of the rectangles representing the nanosheets, where $\phi(\xi)$ is the standard normal distribution and $\Phi(x)$ is its cumulative distribution function.

Based on the results from DLS measurements, a mean sheet size of $\mu = 70\,\mu\text{m}$ and standard deviation of $\sigma = 20\,\mu\text{m}$ are appropriate, with truncation at $a = 10\,\mu\text{m}$, $b = 130\,\mu\text{m}$. Therefore the side lengths of the rectangles are represented by:

$$l, w \sim \phi_{\text{trunc}}(\mu = 70\,\text{nm}, \sigma = 20\,\text{nm}, a = 10\,\text{nm}, b = 130\,\mu\text{m}) \tag{15}$$

and the orientation θ of each sheet on the substrate is represented by a uniform distribution (Unif):

$$\theta \sim \text{Unif}(0, \pi). \tag{16}$$

Similarly, the deposition location of each square is represented by its centre coordinates (x_c, y_c),

$$x_c \sim \text{Unif}(0, L), \quad y_c \sim \text{Unif}(0, W), \tag{17}$$

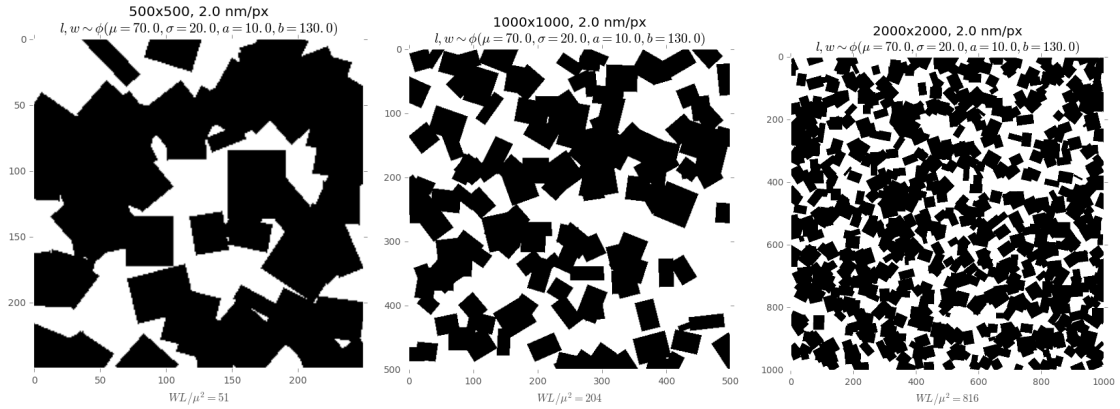

(a) Sample depositions at percolation threshold for various deposition areas.

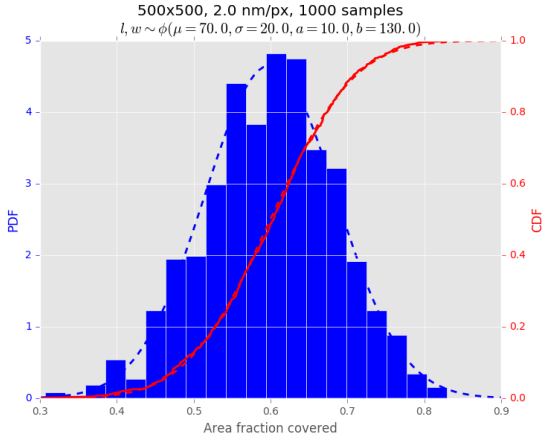

(b) Area fraction covered.

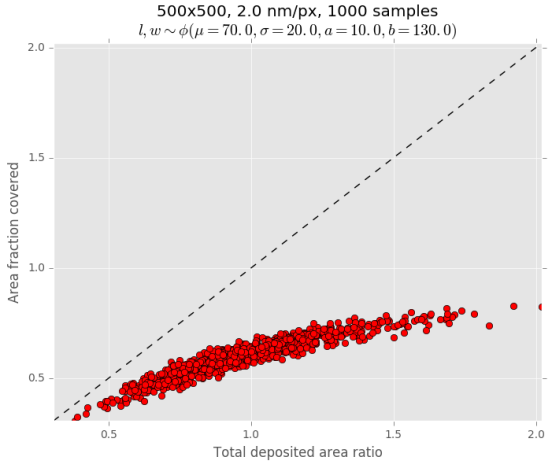

(c) Area fraction covered p_c vs. total deposited area ratio $\tilde{p}_c$. For $p_c = 0.6$, $\tilde{p}_c \approx 0.9$ and for $\tilde{p}_c = 0.6$ for $p_c \approx 0.48$.

Figure 28: Percolation threshold simulation results for a square domain of $500 \times 500\,\mathrm{nm}^2$.

where L and W are the length and width of the deposition area, respectively.

The algorithm was implemented in Python, using the NumPy [83], SciPy [84], PIL [85] and matplotlib [86] packages. In every iteration, a random rectangle $[l, w]$ was drawn on a canvas, followed by a continuity test from side to side. If a continuous path was found from side to side, indicating percolation is reached, the simulation was terminated. Every such calculation contributed a statistical data point (Figure 28). Figure 28b shows percolation statistics of a square domain, showing that the percolation threshold for the parameters used is achieved at slightly less than 60% surface coverage.

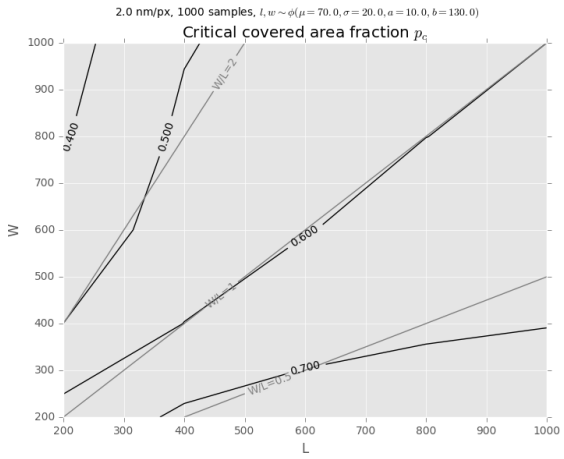

(a) The critical covered area fraction p_c as a function of W and L.

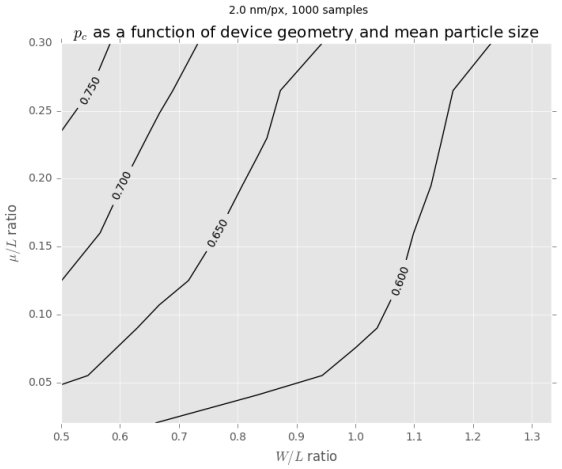

(b) The critical remaining area fraction p_c as a function of the mean particle size distribution μ (standard deviation of $\sigma = 20\,\text{nm}$ was kept constant) and the W/L ratio.

Figure 29: Influence of W/L ratio and particle size distribution.

III.2.2.3 Influence of W/L ratio and particle size distribution

The critical covered area fraction p_c was calculated for various combinations of length and widths (Figure 29a). As W/L increases (from bottom right to top left in the figure), the critical coverage ratio p_c decreases. This is in agreement with expectation because the minimal number of rectangles needed to reach percolation (bridge the channel gap) depends on L, not W, such that with a high W, less area in total needs to be covered at percolation.

In the case of $W/L = 1$, the percolation threshold $p_c \approx 0.6$ is approximately constant and independent of the absolute size of the system. In TFTs, however, geometries of $W/L > 1$ are typically used. The percolation threshold at the limit of $W/L = 1$ is therefore useful because of the constant value of $p_c \approx 0.6$, which can be used as the upper limit for the critical area coverage ratio in all practical devices.

To confirm that the critical covered area fraction $p_c = 0.6$ is a valid upper limit for various particle size distributions, it was calculated for various μ/L ratios, where μ is the mean particle size distribution (Figure 29b). For $W/L = 1$, the particle size needs to be $\mu/L \lessapprox 0.075$ to achieve percolation at $p_c = 0.6$ or lower. For the particle size distributions used in this research ($\mu \sim 100\,\text{nm}$), this ratio is maintained for all channel lengths used ($5 - 50\,\mu\text{m}$). Actual W/L ratios are at least 10 such that $p_c = 0.6$ is a very conservative value for approximating the minimal concentration required to achieve percolation.

Table 7: Summary of the minimal concentration evaluated for a 10 μL droplet of 5 mm diameter, using the methods described in this section. All values are in $\left[\frac{\text{mg}}{\text{L}}\right]$.

Thickness	Uniform film	Perfect ring-stain (40 μm thick)	Continuum percolation ($p_c = 0.6$)
1L	~ 6	~ 0.2	3.7
5L	~ 30	~ 1	18.4

III.2.2.4 Evaluation of minimal concentration and deposited volume

Based on the critical covered area fraction p_c it is possible to evaluate the minimal concentration c of the deposited suspension:

$$c = \frac{\tilde{p}_c A_d \rho_{2\text{D}}}{V_c} \tag{18}$$

where $\tilde{p}_c$ is the effective area fraction from Figure 28c, A_d is the rectangular area over which the volume V_c is deposited and $\rho_{2\text{D}}$ is the surface density of the suspended material. For practical $^W/_L$ ratios, $p_c\,(\tilde{p}_c = 0.6) = 0.48$ is still a conservative approximation (Figure 29a) and therefore, for simplicity, it is assumed that $\tilde{p}_c = p_c = 0.6$.

Typical values for the minimal concentration of drop-casted samples, as well as in comparison to the concentration evaluation methods described previously, are presented in Table 7.

However, when depositing a thin film using a suspension with a known concentration, it is more convenient to know the required volume to be deposited per unit area of the substrate to achieve the critical surface density:

$$V_c = \frac{p_c A_d \rho_{2\text{D}}}{c}. \tag{19}$$

Typical values for inkjet printing, drop casting and spray coating are given in Table 8. Using the commercial MoS_2 suspension that was shown to have a concentration of 1 $\frac{\text{mg}}{\text{L}}$ and sheet thickness of 5 layers, these calculations suggest that typically around 20 subsequent drop-castings or 3 minutes of spray coating are needed for obtaining a percolating network.

III.2.2.5 Resistance evaluation of structured networks comprised of square sheets

In order to evaluate the expected channel resistance, a structured network of resistors was used to model the total resistance of deposited films (Figure 30b). In the case of a perfect uniform film, every node is connected to all of its nearest-neighbours, and in the case of a partial area coverage, only some nodes are connected to some of its nearest-neighbours.

In the case where all resistors are identical (R), the current in the vertical direction is zero and the

Table 8: Typical deposition parameters for various deposition methods, using $p_c = 0.6$. A_d is the deposition area, c is the concentration of the MoS_2 suspension, NL is the number of layers of the MoS_2 sheets and V_c is the critical deposition volume.

(a) Typical values for the critical deposition volume for inkjet printing and drop casting. V_0 is the volume of a single droplet and N_d is the number of droplets required.

	Inkjet printing			
A_d; V_0	$10000\,\mu\text{m}^2$; 80 pL			
c $\left[\frac{\text{mg}}{\text{L}}\right]$	1		18	
NL	1	5	1	5
V_c [pL]	18500	92500	1030	5140
N_d	230	1160	13	65

	Drop casting			
A_d; V_0	$20\,\text{mm}^2$; $10\,\mu$L			
c $\left[\frac{\text{mg}}{\text{L}}\right]$	1		18	
NL	1	5	1	5
V_c [μL]	37	184	2	10
N_d	4	19	1	1

(b) Typical values for the critical deposition volume for spray coating. $\dot{V}_0$ is the volumetric flow rate and t_d is the required deposition time.

	Spray coating							
A_d; $\dot{V}_0$	$20\,\text{mm}^2$; 1 $\frac{\mu\text{L}}{\text{s}}$				$4500\,\text{mm}^2$; 10 $\frac{\mu\text{L}}{\text{s}}$			
c $\left[\frac{\text{mg}}{\text{L}}\right]$	1		18		1		18	
NL	1	5	1	5	1	5	1	5
V_c [mL]	0.04	0.18	0.002	0.01	8.3	41.5	0.5	2.3
t_d [min : sec]	0:37	3:05	0:02	0:10	13:50	69:08	0:46	3:50

total resistance of the network is given by:

$$\frac{1}{R_{\text{tot}}} = \sum_i^{N_i} \frac{1}{\sum_j^{N_j} R} = \sum_i^{N_i} \frac{1}{N_j R} = \frac{N_i}{N_j R} \quad \Rightarrow \quad R_{\text{tot}} = \frac{N_j}{N_i} R = \frac{L}{W} R \tag{20}$$

For devices fabricated using mask layouts described in Section III.1.4, typical L/W ratios are 0.1-0.2 for a shadow mask and 0.01-0.1 for a photomask. Therefore, in this limit of tiled squares, the overall channel resistance is approximately 1-10% of an inter-sheet resistance.

In reality, both the inter-sheet resistances and the contact resistance vary. In a study by Nirmalraj *et al.* [68] on inter-sheet resistance in graphene, contact resistances R_c of $\sim 250\,\Omega$ and $\sim 580\,\Omega$ were observed between a metal probe to Pd and Ti/Au electrodes, respectively, and inter-sheet resistances R in the range of$\sim 0.55 - 10\,\text{k}\Omega$ were observed between $\sim 25\,\mu\text{m}^2$-large sheets of thickness of $1 - 7.5\,\text{nm}$ (at 9 nm thick, the resistivity approached that of graphite). These ranges are equivalent to inter-sheet-to-contact resistance ratios of $R/R_c = 1 - 40$. They used top contacts and discovered that the inter-sheet resistance depends on the thickness of the top sheet, with higher resistance for thicker sheets (Figure 30a). For device geometries used here, in the extreme case of $L/W = 0.2$ and $R = 10\,\text{k}\Omega$, this model predicts a total channel resistance of $R_{\text{tot}} = 2\,\text{k}\Omega$, which is equivalent to a source-drain current of $I_{\text{d}} = 0.5\,\text{mA}$ under a bias of 1 V.

In order to better model a channel, random resistor values were used with a normal distribution of various means $\bar{R}$ and standard deviations $0.25\bar{R}$ (chosen arbitrarily; depends on the thickness distribution).

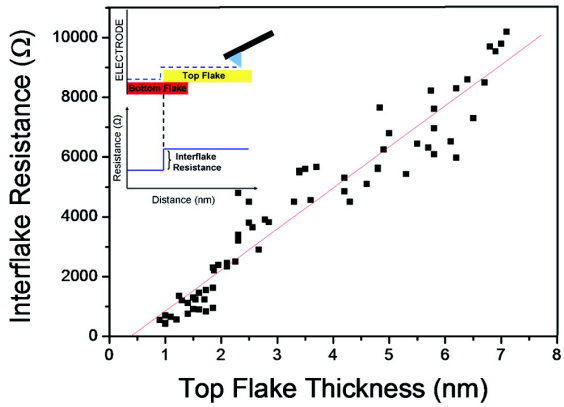

(a) Inter-sheet resistance in graphene, as a function of the top sheet thickness. Reprinted (adapted) with permission from [68]. Copyright © 2010 American Chemical Society.

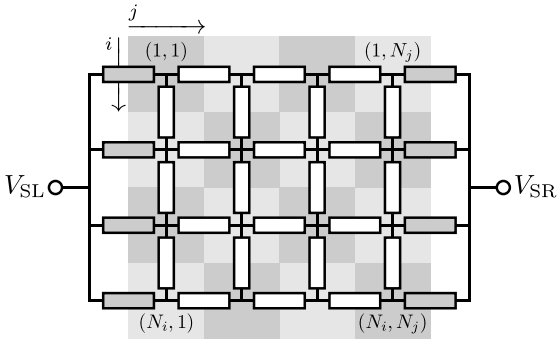

(b) Structured tiles of square sheets as a model of a uniform film, and a network of resistors as a model for inter-sheet transport. They grey resistors on the left and right boundaries of the network represent the contact resistance to the electrodes. The resistor network was solved using mesh analysis (Appendix C).

Figure 30: Experimental results for inter-sheet resistance (a) and a model used to evaluate the total resistance of a continuous channel of adjacent sheets (b).

The total resistance R_{tot} was normalized by the contact resistance R_c and the normalized total resistance ${}^{R_{\mathrm{tot}}}/_{R_c}$ is presented in Figure 31 as a function of ${}^{N_i}/_{N_j}$ (equivalent to ${}^{W}/_{L}$) and the normalized mean inter-sheet resistance ${}^{\bar{R}}/_{R_c}$. Normalizing by the contact resistance R_c is convenient as it is expected to be the lowest resistance in the system. Two cases were studied: (a) a fully continuous grid; (b) a grid with 40% "vacancies" (implemented by high resistance values, for simplicity), representing $p_c = 0.6$. For device geometries used here, in the extreme case of 40% vacancies ($p_c = 0.6$), ${}^{L}/_{W} = 0.2$ (or ${}^{W}/_{L} = 5$) and ${}^{\bar{R}}/_{R_c} = 40$, this model predicts a total channel resistance of ${}^{R_{\mathrm{tot}}}/_{R_c} \sim 40$. This value is still quite low and implies that the total resistance of a random graphene nano-sheet channel would be $\sim 10 - 24\,\mathrm{k\Omega}$, which is equivalent to a source-drain current of $I_{\mathrm{d}} = 40\,\mu\mathrm{A} - 0.1\,\mathrm{mA}$ under a bias of 1 V.

The contact resistance and the inter-sheet resistance in the case of MoS_2 nanosheets is expected to differ from graphene, but these results still hold because scaling all the resistances by a multiplicative factor would have no effect on the overall trend.

Assuming that R_{tot} of a film of MoS_2 nanosheets is limited to only a few orders of magnitude of R_c (similarly to graphene), it is expected to obtain measurable currents for all the device geometries in use (Section III.1.4). The contact resistance to a film of nanosheet MoS_2 could not be evaluated due to the poor performance of the fabricated devices, but values reported in literature can be used instead (Table 9). Using a sheet size of $\mu = 70\,\mathrm{nm}$, it is possible to evaluate the contact resistance R_c to a single sheet:

$$R_c = \frac{\rho_c}{\mu} < \frac{740 \cdot 10^{-3}}{70 \cdot 10^{-9}} = 10.6 \times 10^6\,\Omega = 10.6\,\mathrm{M\Omega}, \tag{21}$$

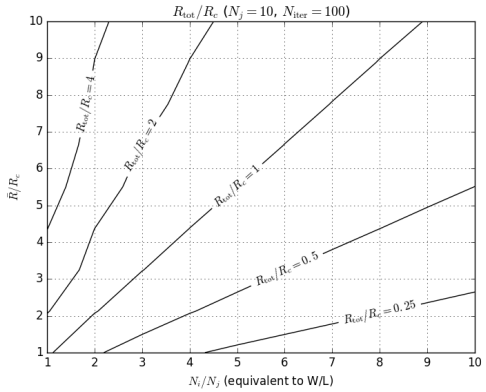

(a) Fully continuous grid.

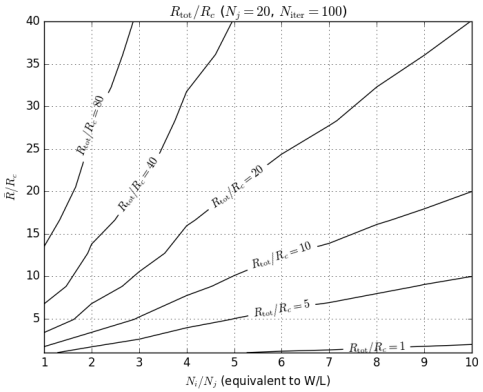

(b) A grid with 40% vacancies (implemented using $R = 10^{12}\,\Omega$ for a random set of 40% of resistors). The numerical anomaly at the bottom left disappears when N_j is 20 and higher.

Figure 31: The normalized total resistance $^{R_{tot}}/_{R_c}$ as a function of $^{N_i}/_{N_j}$ (equivalent to $^{W}/_{L}$) and the normalized mean inter-sheet resistance $^{\bar{R}}/_{R_c}$.

Table 9: Contact resistivity to MoS_2 few-layer sheets.

	MoS_2		
Metal	Thickness	Phase	Contact resistivity, ρ_c [$k\Omega \cdot \mu m$]
Ti [87]	1 layer	2H (not reported)	740
	2 layer		15.6
	5 layers		1.56
Au [88]	1-3 layers	2H	1.1
		1T	0.2

where ρ_c is the contact resistivity reported in literature. Therefore, assuming that R_{tot} of a film of MoS_2 nanosheets is limited to at most $40R_c$ (similarly to graphene), the max total measured resistance for the device geometries used is expected to be:

$$R_{tot} < 40R_c \simeq 420 \times 10^6\,\Omega = 420\,M\Omega, \tag{22}$$

which is equivalent to a source-drain current of $I_d > 2.4\,nA$ under a bias of 1 V.

It is noteworthy that the total channel resistance in this model depends largely on the $^{L}/_{W}$ ratio and does not depend on the absolute sheet dimensions, which may not be the case in reality for extremely small sheets due to quantum effects or the influence of end-groups on sheet properties. Indeed, while in theory the total resistance based on the above calculation is expected to be fractions of GΩ at most, in experiment very high resistance values, of at least two orders of magnitude higher, were measured even for thick films and high $^{W}/_{L}$-ratio devices (Section III.3.3). Similarly, current levels of 1-2 orders of magnitude lower than calculated here were reported in experimental results, even for full areal coverage [34].

Measuring the inter-sheet resistance of MoS_2 sheets should be addressed in future studies to better understand the origin of the extremely high channel resistance. In the absence of theoretical and experimental data, it is difficult to conclude if the high inter-sheet resistance is an intrinsic property of MoS_2 or simply a result of a poor-quality film.

III.3 Drop-casted devices

Drop-casting is a very convenient deposition method for small-scale prototyping, where droplets of 5 μL can be manually placed on a substrate using a micropipette. Drop-casting enables consistently depositing $\sim 20\,\mathrm{mm}^2$ of thin film per droplet, an area inside which several devices can be patterned for electrical characterization of the dry film (Section III.1.4).

The challenges encountered in obtaining continuous MoS_2 films via drop-casting are similar to inkjet printing and include the ring-stain effect, which causes more material to be deposited at the periphery of the deposited droplets, droplet migration due to surface energy differences, and increased MoS_2 agglomeration due to flow currents inside the drying droplet. Filtration and modifiers such as ethylene glycol and ethyl cellulose were tested for reducing agglomeration and improving film uniformity. Surface energy modification of the substrate was employed for increasing the contact angle between the droplet and the substrate, hence reducing the total area and increasing the average MoS_2 density in the deposited film. The influence of the number of droplets and the substrate temperature on film formation were tested, and finally, circular patterns were tested for exploiting the ring-stain effect.

III.3.1 Effect of particle size distribution on film uniformity

In order to determine the influence of particle size distribution, or rather, the particle size upper cutoff, on film uniformity, the MoS_2 nanosheet suspension was filtered with various pore size filters and drop-casted on HMDS-treated SiO_2 substrate. The suspension used was the in-house exfoliated sheets due to their higher initial particle size distribution, as determined by DLS measurement. Optical micrographs of dry 0.45, 1 and 5 μm filtered droplets are shown in Figure 32.

As discovered in the UV-vis analysis, the 0.45 μm filter ("protein filter") actually gives higher concentration than the PTFE 5 μm filter (the filters are from different vendors; Section II.1.1), and therefore a higher particle size distribution cutoff. Films of the highest particle size distribution (0.45 μm filter) contained areas of different film density with an obvious ring-stain effect and occasional large aggregates. The slightly lower particle size distribution (5 μm filtered sample) had periodic film discontinuities and overall poor coverage. Films of the lowest particles size distribution (1 μm filter) did not contain any aggregates but patterns of mild nonuniform film density were observed. These results were consistent in repeated experiments. It is therefore concluded that the tendency of colloidal suspensions of MoS_2 nanosheets to form aggregates is diminished with reduced sheet size distribution such that filtered suspensions result in less irregularities in the dry film.

Interestingly, based on the SEM image of the ring-stain of the 5 μm sample, it is clear that the MoS_2

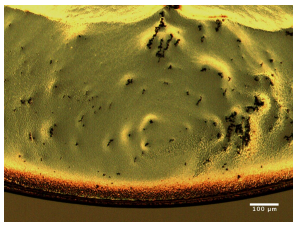

(a) 0.45 μm pore size filter (actually largest particle size distribution).

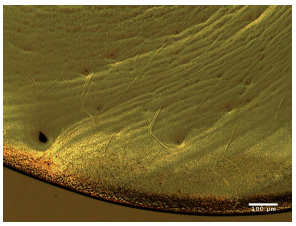

(b) 5 μm pore size filter.

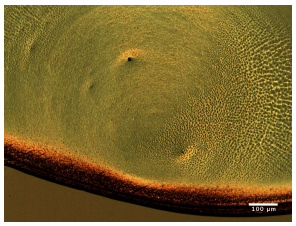

(c) 1 μm pore size filter.

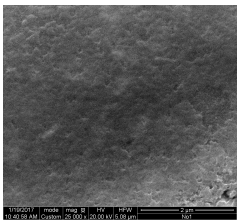

(d) SEM image inside ring-stain of (b).

Figure 32: Optical micrographs (a-c) and SEM (d) images of films formed by drop-casting in-house exfoliated MoS_2 nanosheet suspension filtered with various pore size filters on HMDS-treated SiO_2 substrate. Drops were casted on a 50°C hotplate to slightly reduce drying time. In the SEM image, individual sheets are indistinguishable inside the film, and the nanosheet films appear to be continuous, suggesting that agglomerated MoS_2 nanosheets may be used as a channel material in TFTs.

nanosheets form a thick, dense and continuous ring-shaped film along the perimeter. As shown later (Section III.4.3), the ring-stain shape can be exploited for device fabrication.

III.3.2 Effect of substrate temperature on film formation

In order to determine the influence of substrate temperature on film formation, droplets from the commercial suspension (GS-MDS-NF) were drop-casted on a substrate at various temperatures on HMDS-treated SiO_2 and SiNx substrates.

At first, two different temperatures of HMDS-treated SiO_2 substrates were studied: room temperature and 90°C. In addition, filtered suspensions were compared to unfiltered suspensions. Optical micrographs of the resulting films are presented in Figure 33.

From the results it is clear that a substrate at an elevated temperature increases the ring-stain effect, regardless of the particle size distribution. This effect can be attributed to the more violent flow inside the droplet at 90°C, bringing suspended MoS_2 close to the liquid-gas interface, where the MoS_2 is efficiently transported towards the contact line, as was suggested for colloidal sessile droplets [57]. Depositing 5 drops resulted in additional agglomeration with highly disordered deposition profile.

A single droplet of the commercial suspension resulted in a discontinuous film (Figure 33), compared to the in-house exfoliated MoS_2 that resulted in a more uniform coating (Figure 32). This difference can be attributed to the high MoS_2 concentration of the in-house suspension.

These observations suggests that a substrate temperature that is near the near-boiling point of the suspension[18] is not suitable for obtaining mm-scale uniform films from aqueous colloidal suspension, but

[18]The reported boiling point for 45 vol% (65 wt%) ethanol in water is 80-85°C but the deposited droplets on a 90°C substrates were not boiling. The suspended MoS_2 sheets may have increased the boiling point of the suspension. Moreover, as determined from UV-vis analysis, the dispersing medium of the commercial suspension differs from a reference 45 vol%

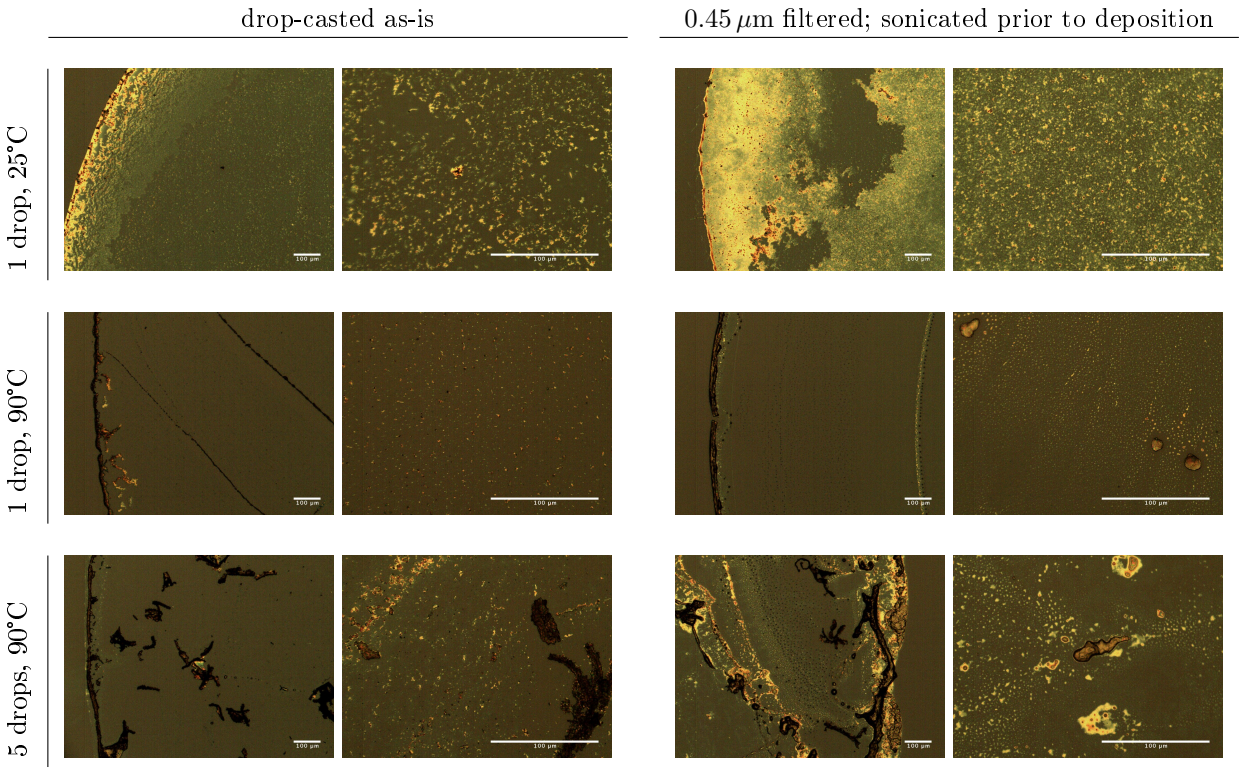

Figure 33: Optical micrographs of 10 μL droplets of GS-MDS-NF on HMDS-treated SiO_2/Si. A comparison between (i) droplets deposited as-is and after 0.45 μm filtering and sonication prior do deposition, and (ii) drying at room temperature and on a 90°C hotplate. All scale bars are 100 μm.

it can be used for the fabrication of circular devices that take advantage of the ring-stain. Raman spectra (Figure 34) confirmed that there is significantly less MoS_2 content outside the ring-stain, and that 90°C anneal in air does not alter the MoS_2 characteristic peaks, suggesting that 90°C anneal in air is a safe process step for nanosheet MoS_2.

The influence of substrate temperature was further studied on a SiNx substrate (without HMDS treatment), on which more uniform films are formed, compared to HMDS-treated SiO_2 or bare SiO_2. The influence of ethyl cellulose (EC), which is typically used as a suspension stabilizer, was also tested. Optical micrographs of the resulting films are presented in Figure 35. Overall, with the presence of EC the ring-stain is wider but the interior is more uniform compared to the original suspension (without EC). The best film uniformity was obtained with hotplate temperatures of 50°C and 80°C, with a slight advantage for 50°C.

These results are evidence of the major role of the colloidal properties of suspended particles in film uniformity and the formation of ring-stains. It was shown for colloidal suspensions of nanospheres that

suspension.

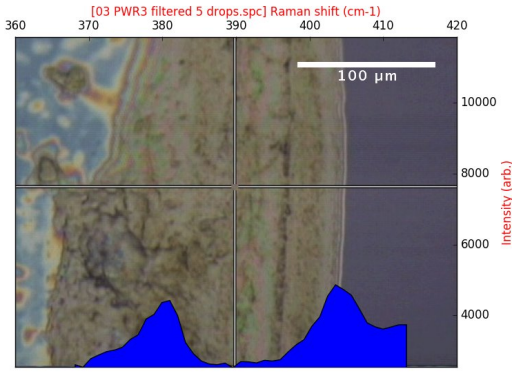

(a) Measurement taken at the ring-stain.

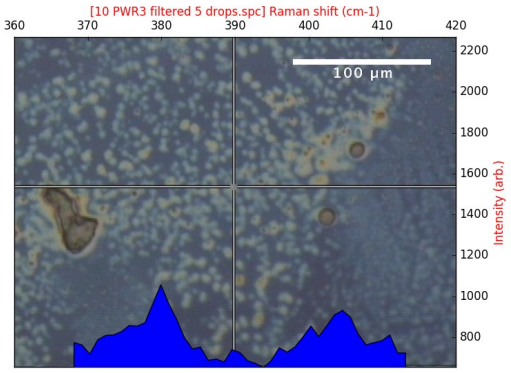

(b) Measurement taken away from the ring-stain.

Figure 34: Raman spectra (a) at the ring-stain and (b) at the droplet centre for the sample of 5 drops, 0.45 μm filtered and sonicated prior to deposition, dried on 90°C hotplate. In both cases the characteristic MoS_2 peaks are visible, but in the centre of the drop the peaks have lower intensity.

different evaporation profiles induce different deposits. An outwards flow develops when the evaporation rate is relatively constant along the fluid-air interface or slightly elevated near the contact line and results in a ring-stain [89]. On the other hand, an inwards flow develops if the evaporation rate is higher at the centre of the droplet and results in a more uniform deposit [89]. As a result, a pinned contact line would imply zero evaporation rate at the contact line, giving rise to a uniform deposit. However, a different model was recently proposed for describing ring-stain deposits even in a pinned contact line scenario, which involves mass transport along the liquid-air interface [57]. In addition to the evaporation rate profile, slight changes in the concentration of the nanospheres in suspension has a major role on the pattern of the dry deposit [90]. In summary, the predictions of current models are inconclusive since all the existing models for droplet evaporation involve many assumptions for simplifying the governing equations, such that only a part of the phenomenon can be captured. An in-depth study of the influence of colloidal properties on film uniformity is beyond the scope of this research and should be addressed in future studies.

III.3.3 Influence of number of drop-castings

Compared to SiO_2 substrate, single droplets deposited on silicon nitride (SiNx) exhibited a more uniform texture at the droplet centre as well as a sharp and neat ring-stain (Figure 36). Therefore, SiNx was chosen for testing top contact device performance for various film thicknesses, obtained by subsequent depositions of 1, 2, 5, 10 and 20 drops of 5 μL each (Table 8).

In all tested cases, a considerable ring-stain was formed and the interior of the droplet had a various degree of coverage. As expected, the area coverage improved with an increasing number of deposited

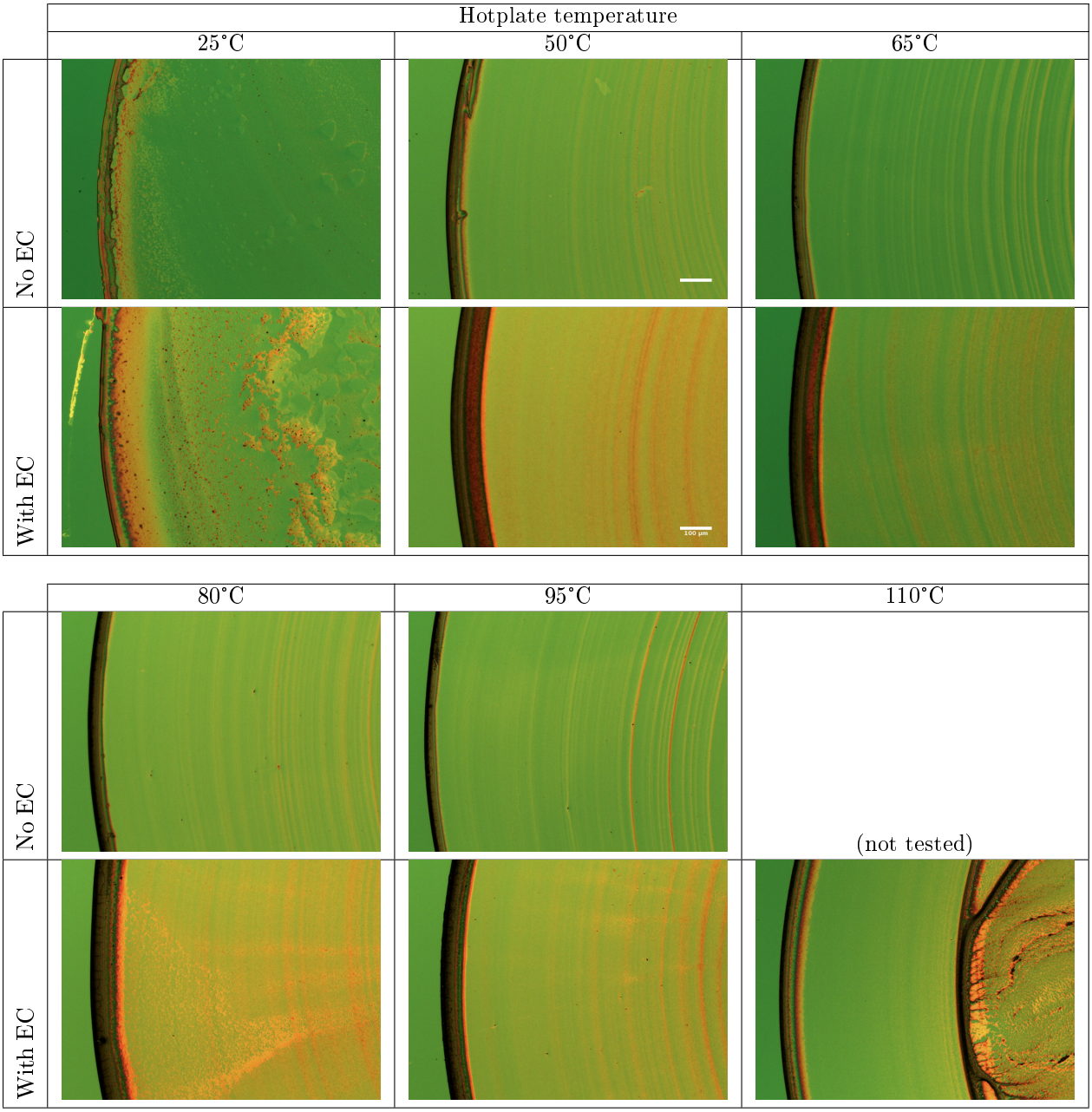

Figure 35: Optical micrographs of 5 μL single droplets of 0.45 μm filtered GS-MDS-NF on SiNx. A comparison between (i) various hotplate temperatures, and (ii) without and with ethyl cellulose. All scale bars are 100 μm and all images are the same scale.

droplets. With 5 deposited droplets, visible aggregates start to form but the coverage is non-uniform at all stages.

In order to test device performance, planar films are preferred. To avoid unnecessary contamination, the original suspension was used as-is (without ethyl cellulose). Film thicknesses of 1, 2, 3, 6, 9 and 12 drops were studied with Cr and Al top electrodes that were thermally evaporated via a shadow mask (Figure 37). While drop-casting, a mm-wide aggregate of material was formed inside the droplet interior. All aggregates were off-centre due to a mild incline of the drying surface. The off-centre aggregates kept growing with subsequent depositions, such that the height profile of the droplet interior was inconsistent. Notably, the metal top contact tended to peel off upon probe tip detach. This indicates poor adhesion between the drop-casted MoS_2 nanosheets to themselves and to the substrate. Moreover, the irregular MoS_2 film caused morphological irregularities and cracks in the metal electrodes.

Before measuring the electrical properties of the device, Raman spectroscopy was used to confirm the presence of MoS_2 in the channel area (Figure 38). Out of the 288 fabricated devices, 180 were measured, only 4 devices had a somewhat conductive channel, and none of the devices showed field effect. Channel conductance of Cr and Al devices were not consistent. This can be attributed to the irregular nanosheet film and to the relatively large channel lengths of $50 - 100\,\mu$m, which were the shortest viable channel lengths in the shadow mask process used.

Shorter channels were then used in order to reduce the total resistance. Since MoS_2 nanosheet films have low adherence to the substrate, depositing top contacts via lithography process would wash-off the MoS_2 film during the photoresist process. Therefore, bottom contact architecture was used. Bottom contact devices with $W = 5000\,\mu$m and $L = 5\,\mu$m were used for obtaining devices with increased channel conductivity (Figure 39b). MoS_2 nanosheet droplets were subsequently deposited in order to cover the whole channel length. Aggregates of MoS_2 were distributed unevenly across the metallized areas but nonetheless the channel gap was bridged with sufficient material, as can be concluded from measured resistances. On one exemplary device, currents of 1 and 6 μA were measured for drain voltages of 0.1 and 0.5 V, respectively, regardless of the gate voltage, which was swept in the range $\pm 10\,$V. This can be attributed to the onset of bulk conductivity due to a too thick film. The equivalent channel resistance in this case was $100\,\mathrm{k}\Omega$ but it is difficult to extract the current density or channel resistivity because the effective channel width is unknown due to the irregular deposition. Nonetheless, these measurements demonstrate that a channel gap can be bridged by a continuous path of nanosheet MoS_2 via drop-casting.

In addition to the absence of field effect due to bulk conductivity of thick MoS_2 films, bottom contact devices with such films were occasionally burnt. In several occasions, a part of the MoS_2 channel appeared to be boiling as long as a drain bias was applied (this was observed for drain voltages as low as 10 V).

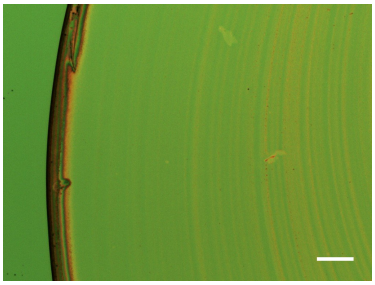

(a) 1 drop, no EC.

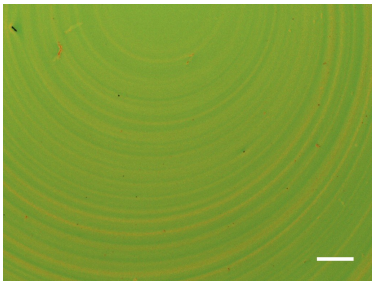

(b) 1 drop (droplet centre), no EC.

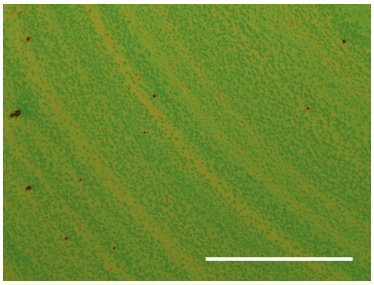

(c) 2 drops, no EC.

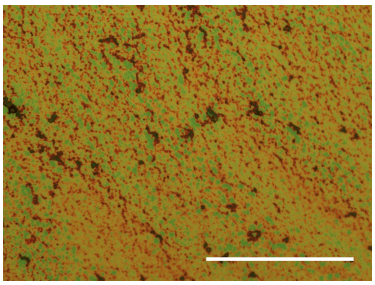

(d) 5 drops, no EC.

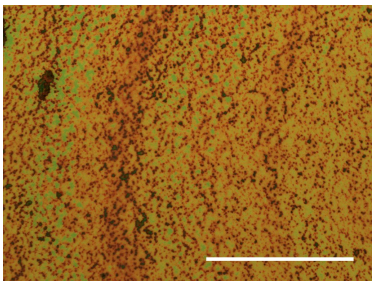

(e) 10 drops, no EC.

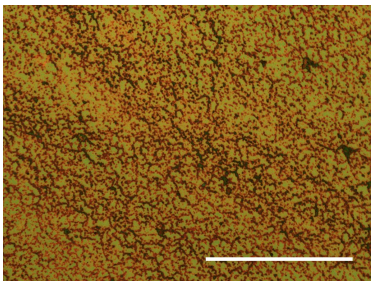

(f) 20 drops, no EC.

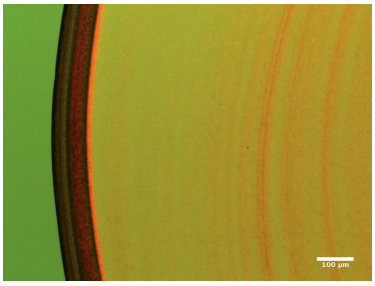

(g) 1 drop, with EC.

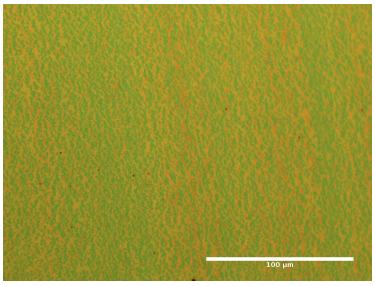

(h) 1 drop (droplet centre), with EC.

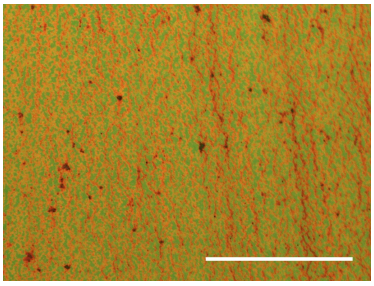

(i) 2 drops, with EC.

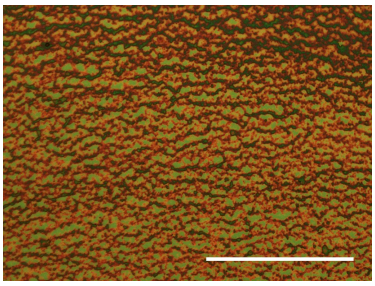

(j) 5 drops, with EC.

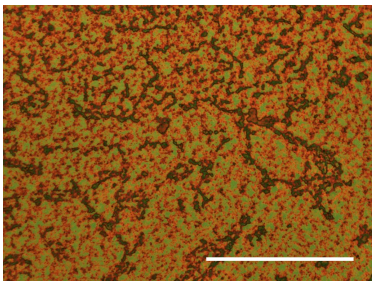

(k) 10 drops, with EC.

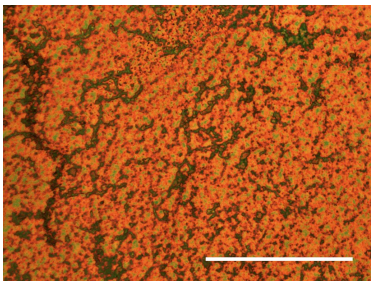

(l) 20 drops, with EC.

Figure 36: Scale bars 100um. MoS_2 on SiNx, sonicated and 0.45um filtered, hotplate at 50°C, without (a-f) and with (g-l) ethyl cellulose (EC). 2 min sonication (PWR 5) immediately prior to drop-casting. No HMDS.

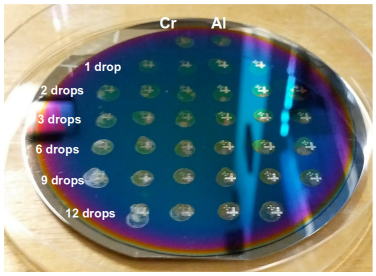

(a) Photograph of the final devices with Cr and Al electrodes on a 3" wafer.

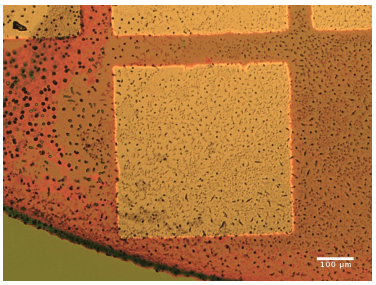

(b) Cr contacts on a single drop of MoS_2. Mild ring-stain, with apparently uniform and continuous droplet interior. No conduction through the channels and no field effect were detected.

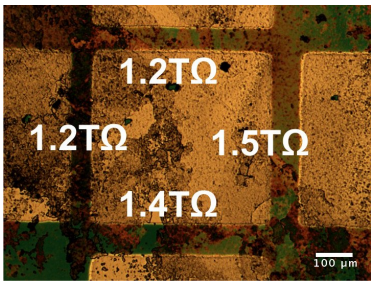

(c) Cr contacts on 12 drops of MoS_2. Measured channel resistance is labelled on the figure. Within 7 days the conductance degraded below noise level.

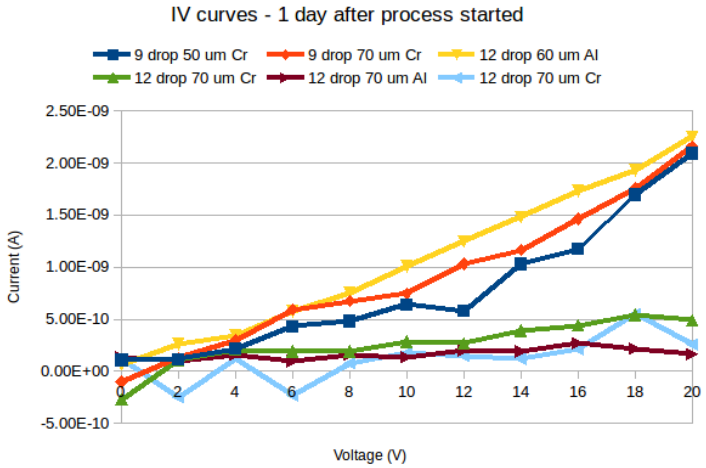

(d) Id-Vd curves were used to extract channel resistances. Out of all the measured devices only a few showed above-noise current. The lowest extracted resistance was $8 - 10\,G\Omega$. No field effect was observed. Keithley 4200-SCS was used for the measurements.

Figure 37: E-beamed Cr and Al top contact devices on multiple drops of MoS_2 on SiNx substrate.

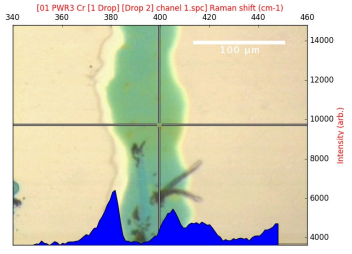

(a) 1 drop. Characteristic peaks are present, with $\Delta\nu = 23.6\,cm^{-1}$, equivalent to <Bulk in single crystal MoS_2.

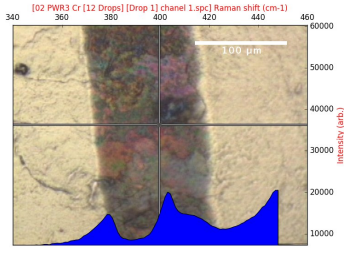

(b) 12 drops. Characteristic peaks are present, with $\Delta\nu = 24.6\,cm^{-1}$, equivalent to <Bulk in single crystal MoS_2. The much higher intensity here compared to 1 drop is due to the higher concentration of MoS_2.

Figure 38: Raman spectra of drop-casted GS-MDS-NF devices on SiNx.

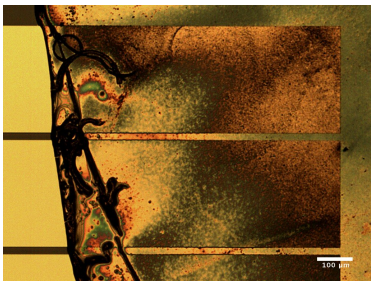

(a) Multiple drops of own Na-exf MoS_2 suspension partially covering an array of $L = 20\,\mu$m channel devices on $Cr/SiO_2/Si$, showing large-area coverage and thick deposited film.

(b) Multiple drops of GS-MDS-NF on Cr/SiNx bottom contact devices with $L = 5\,\mu$m and $W = 5000\,\mu$m.

Figure 39: Optical micrographs of drop-casted MoS_2 suspensions on wide-channel arrays. The large size of the droplets and the relatively slow evaporation result in non-uniform depositions across the electrodes.

Measurements of top contact devices in vacuum with similar drain voltages occasionally left burn marks on the contact pads. The reason for this can be attributed to local heating due to high resistance interfaces between the metal and the nanosheet film.

III.3.4 Surface treatment for improved film uniformity

One of the main difficulties encountered while fabricating drop-casted devices was film uniformity. In order to increase uniformity of drop-casted films, surface treatment with a hydrophobic coating was employed. The chosen coating was an electronic grade fluoropolymer [91]. The fluoropolymer was spin-coated to obtain a low thickness. Drop-casted droplets had higher contact angles compared to HMDS-treated and SiNx surfaces, resulting in smaller base diameter, which in turn resulted in higher surface concentration of MoS_2 (Figure 40). However, spin-coating introduced high peak-to-peak undulations in the fluoropolymer coating of up to 150 nm (Figure 40f), which is the same order of magnitude of the deposited Cr thickness (100 nm). In addition, the non-reactive fluoropolymer coating resulted in the deposited metal peeling off during probing. The application method of the fluoropolymer could have been optimized to reduce undulations but deposited electrodes would still easily peel off due to the low adhesion of the coating to both the substrate and the metal.

While the fabricated devices were not functional, surface treatment was demonstrated as an effective way to control deposited droplet geometry and film uniformity.

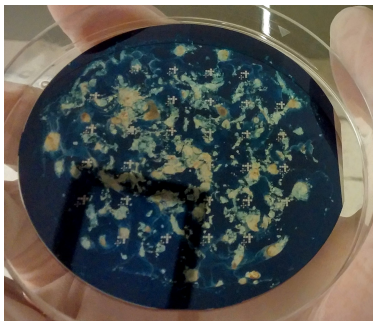

(a) Drop-casted MoS_2 on bare SiO_2. The low contact angle prevents patterning well-defined features.

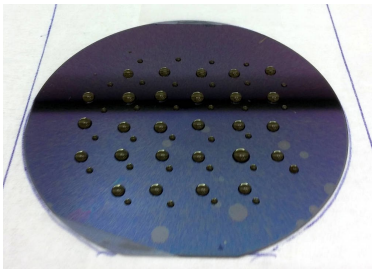

(b) Drop-casted MoS_2 on fluoropolymer-coated SiO_2. The high contact angle allows patterning well-defined features.

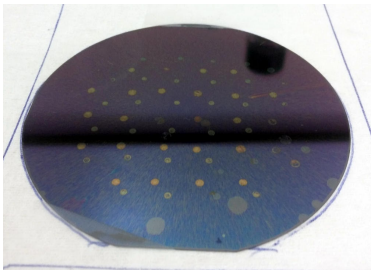

(c) Dry MoS_2 films of (b).

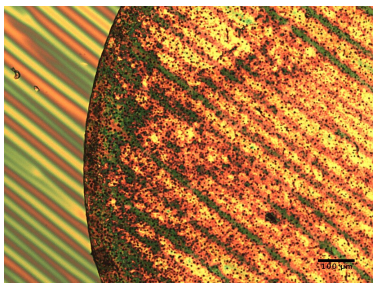

(d) drop-casted MoS_2 on fluoropolymer. The diagonal colourful lines are due to periodic fluoropolymer thickness variation after spin-coating.

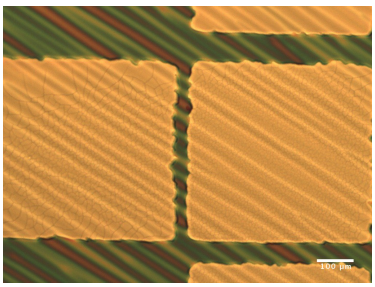

(e) Cr pads are deformed to to the varying fluoropolymer height profile.

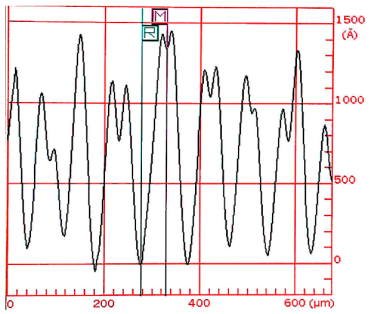

(f) Stylus profilometry of Cr on spin-coated fluoropolymer. The fluoropolymer undulations are in the same scale of the deposited Cr thickness (100 nm).

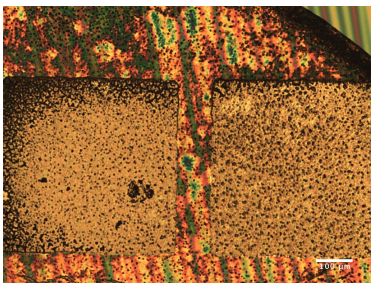

(g) Cr contacts on a drop-casted MoS_2 film on fluoropolymer. Cracks are visible at the edges of the electrodes.

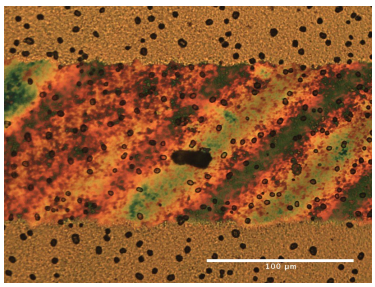

(h) Close up view of the channel region. The undulations of the fluoropolymer layer are clearly visible.

Figure 40: Cr top contact devices on fluoropolymer-treated SiO_2/Si 3" substrate. All scale bars are 100 μm.

III.4 Inkjet printed devices

The major challenges with drop-casted devices using suspensions that produce ring-stains are the shape and size of the ring-stain, and the resulting film thickness profile. In cases where a significant ring-stain is formed, the film in the droplet interior may be too sparse to transport charge between source and drain electrodes, while at the ring-stain the high thickness may give rise to bulk conductivity without an observable field effect. Inkjet printing can be used to address these issues.

Inkjet printing offers a precise placement of picolitre droplets, three orders of magnitude smaller than drop-casting, and in an automated process. Since the diameter of jetted droplets ($20 - 100\,\mu$m) is in the order of magnitude of typical channel lengths, even if a ring-stain is formed, it is confined to an area similar in size to the channel length. In addition, the low droplet volumes (pL) allow precise control of the amount of deposited material, such that bulk conductivity can potentially be reduced or avoided. Moreover, while subsequent drop-casting causes material redistribution on a large scale, as well as formation of large aggregates, in inkjet printing such phenomena can be limited in scale to fractions of a channel width (Figure 43).

The smaller scale, however, does not alleviate the difficulty of obtaining a semiconducting MoS_2 channel, which is needed for a device to switch in the presence of a gate bias. The most promising results to date were reported by Zhang *et al.* [24] who exfoliated and inkjet printed MoS_2 sheets with lateral dimensions of $20\,\mu$m. A single sheet with such dimensions is large enough to bridge the gap between source and drain electrodes and indeed, similar results to mechanically exfoliated MoS_2 were reported. The demonstrated mobility of $20 - 80\,\frac{\mathrm{cm}^2}{\mathrm{Vs}}$ for a printed device is remarkably high with a real potential in large-scale device fabrication via inkjet printing. However, their exfoliation method involved a hydrazine soak at elevated pressure and temperature, which complicated synthesis. Various authors have demonstrated inkjet printing of films of nanoscale sheets [1, 34] but most reports describe ohmic behaviour of their films with no field-effect or with very weak field-effect ($I_d \sim$ few nA).[19] McManus *et al.* [61] demonstrated a weak photocurrent response in printed 2-terminal devices of graphene-MoS_2-graphene vertically-stacked junctions, but they did not report results for 3-terminal devices. In April 2017, Coleman *et al.* [1] demonstrated switching devices using electrolyte gating of thick MoS_2 films in which all sheets were larger than 320 nm in lateral size; however, without an electrolyte they only achieved $I_d \sim$ few nA and no field-effect was reported. It is therefore evident that forming a functional channel is not a trivial task.

[19] Gate leakage in the range of $I_g \sim I_d$ can produce an apparent field-effect if I_g measurement is overlooked.

III.4.1 Surface energy considerations

Typical droplet volume in inkjet printing is 10-120 pL. In order to successfully bridge the channel gap between two electrodes with a printed film, it is important to take into consideration the difference in surface energy between the substrate and the electrodes, as well as the desired channel length. If the channel is too long, the printed droplet may not stay in place. Although this issue may possibly be overcome by subsequent printing at high frequency (thus increasing the effective volume of the droplet before it migrates away), it is useful to obtain understanding on the behaviour of single printed droplets on patterned substrates.

A convenient method for evaluating droplet-surface interaction is via surface energy minimization. Using the algorithm Matsui *et al.* [92] developed for simulating the equilibrium of microdroplets on flat surfaces, it is possible to simulate such interactions. The algorithm is seeking to minimize the total surface energy, given by:

$$E = \gamma_{\mathrm{LV}} \left(A_{\mathrm{LV}} - \sum_{k=1}^{M} A_{\mathrm{SL},k} \cos\theta_k \right), \tag{23}$$

where γ_{LV} is the surface tension of the droplet, A_{LV} and A_{SL} are the surface area of the droplet in contact with vapour and solid, respectively, and θ is the contact angle of the droplet on the solid. In the case of different M solids, an index $k = 1..M$ is used.[20] Therefore, the required inputs are surface tension of the droplet, contact angle with the substrate (e.g. SiO_2) and with the pattern (e.g. Cr) and the geometries of the pattern and the droplet.

The commercial MoS_2 suspension GS-MDS-NF is 45vol.% EtOH:H_2O, which is equivalent to a mole fraction of 0.2019. The surface tension at room temperature (298K) of the mixture, $31.85\,\mathrm{mN \cdot m^{-1}}$, was obtained by interpolating the data tables of Khattab *et al.* [93] for water-ethanol mixtures.

The typical case of wetting a channel gap between two electrodes is of interest and is therefore explored for two representing cases, the first is for a substrate with lower surface energy compared to the electrodes (similar to Cr on SiNx) and the second is for the opposite case (similar to Cr on SiO_2).

III.4.1.1 Substrates with lower surface energy compared to electrodes

When the surface energy of the electrodes is higher than the surface energy of the substrate, such as in the case of Cr on SiNx (Figure 39b), deposited suspension adheres better to the electrodes than to the substrate, resulting in increased material density on top of the electrodes and reduced material density in the channel gap. In some cases, the deposited droplets may rest entirely on the metal, leaving the channel bare. Simulated results for droplet splitting due to surface energy differences are given in Figure 41. The

[20] Evaporation is not taken into account.

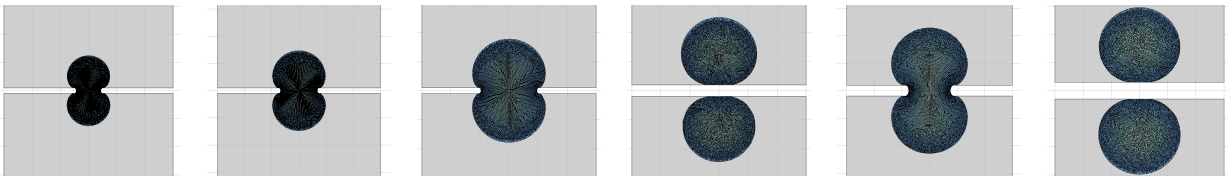

(a) 10μm, 50pL (b) 10μm, 100pL (c) 10μm, 200pL (d) 20μm, 200pL (e) 20μm, 300pL (f) 30μm, 300pL

Figure 41: Droplet splitting simulations for various channel lengths ($10 - 30\,\mu$m) and droplet volumes ($50 - 300\,$pL), with surface tension $\gamma = 73\,\mathrm{mN} \cdot \mathrm{m}^{-1}$, contact angle $\theta_c = 30°$ on the pattern and $\theta_c = 90°$ on the substrate. Grey patterns (pads) are 300 μm wide.

simulation results suggest that inkjet printing on low surface energy substrates has an upper limit for the channel length for a given deposited volume. With the parameters used in those simulations (similar to Cr on silane-treated substrates with deposited volume of up to 300 pL), inkjet printing is limited to devices with channel length of $L = 10\,\mu$m or lower. Moreover, the region of stability, i.e. the region of deposition where an off-centred droplet would split between the two electrodes and not migrate completely onto one of the electrodes depends on the deposited volume.

A possible solution to migration of low volume droplets is high frequency deposition, which may be used to ensure enough volume is deposited before the previously deposited volume has time to go astray. A simpler solution would be to use surfaces with higher energy than the electrodes, as described in the next section.

III.4.1.2 Substrates with higher surface energy compared to electrodes

Printing is more convenient when the surface energy of the electrodes is lower than the surface energy of the substrate, such as in the case of Cr on SiO_2. In those cases, the deposited suspension adheres better to the substrate than to the electrodes, resulting in increased material concentration in the channel region. Simulated and experimental results are presented in Figure 42, with good qualitative agreement.

It was shown that inkjet printing can be used to bridge channel gaps in traditional device architectures by subsequent deposition along the channel (Figure 42b), as well as larger volume deposition covering several adjacent devices. In the latter case, the high substrate surface energy was exploited to "clamp" the deposited volume on top of an array of devices (Figure 42d).

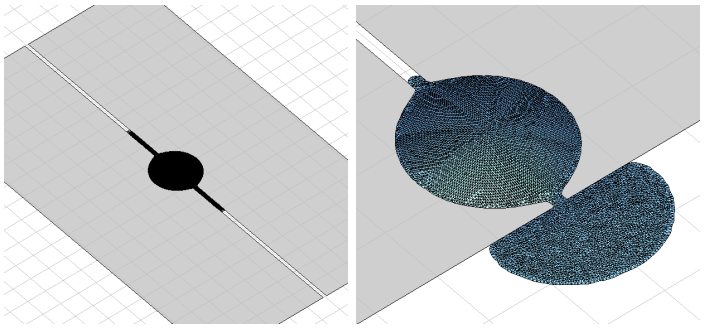

(a) Simulated wetting with droplet volume $\Omega = 60\,\mathrm{pL}$. Channel length is $10\,\mu\mathrm{m}$. **Left**: part of the droplet volume wicks along the channel, but the droplet is stable and successfully bridges the channel gap; **right**: Part of the droplet volume wicks outside the channel (simulation aborted midway to capture the "spill-out" phenomena; the fully equillibrated state is when the droplet is fully outside the device because the simulation does not take evaporation into account).

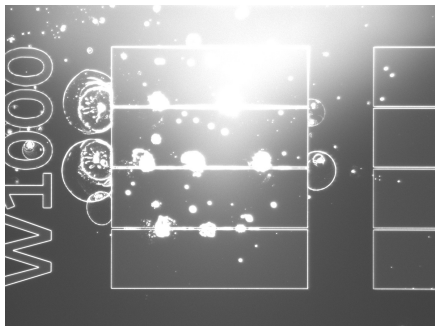

(b) Optical micrograph of GS-MDS-NF printed on Cr/SiO_2. Channel length is $10\,\mu\mathrm{m}$. Both the bridging effect and the spill-out effect are visible.

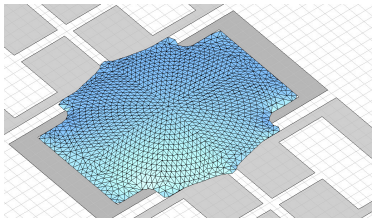

(c) Simulated wetting with droplet volume $\Omega = 25\,\mu\mathrm{L}$. Channel length is $50\,\mu\mathrm{m}$.

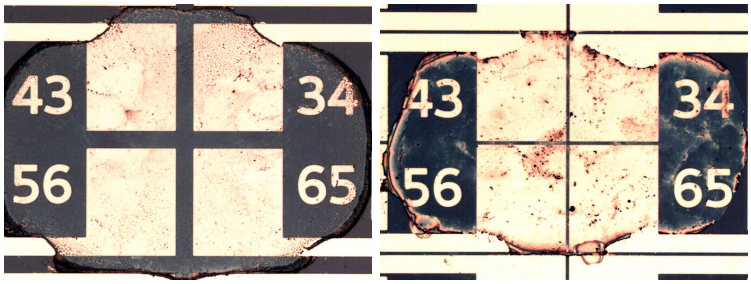

(d) Optical micrograph of about $25\,\mu\mathrm{L}$ of GS-MDS-NF printed on an array of Cr/SiO_2 patterns. Channel lengths are $50\,\mu\mathrm{m}$ (left) and $5\,\mu\mathrm{m}$ (right). Peripheral oxide helps to keep the large droplet on top of the electrodes. The ring-stain of the dry film is similar to drop-casted devices.

Figure 42: Qualitative comparison between simulated wetting and experimental results. All HyDro wetting simulations were run with $\gamma = 30\,\mathrm{mN} \cdot \mathrm{m}^{-1}$, $\theta_c = 20°$ on the pattern and $\theta_c = 1°$ on the substrate.

III.4.2 Conventional devices

Ideally, in the case of suspended MoS_2 nanosheets, printed droplets would evaporate immediately upon impact with the substrate. This way interactions between the current droplet and the previously deposited droplets are eliminated. In the case of solvents with a significant content of water or other high boiling point solvents, the evaporation time is longer than the total printing time of a single feature. Due to the low viscosity and high surface tension of the solution, combined with the long evaporation time, droplets printed along a channel with sufficiently small printing separation combine and form larger, separated droplets rather than dry in place forming a continuous film (Figure 43). Moreover, any subsequent printing continues to reflow into the existing aggregates that were formed in previous prints. As a result, the effective (printed) width in such devices is lower than the actual width of the electrodes. Introducing a thickening agent such as ethylene glycol could potentially alleviate this issue, but in general, introducing contaminants

to an already low-performing material is undesirable.

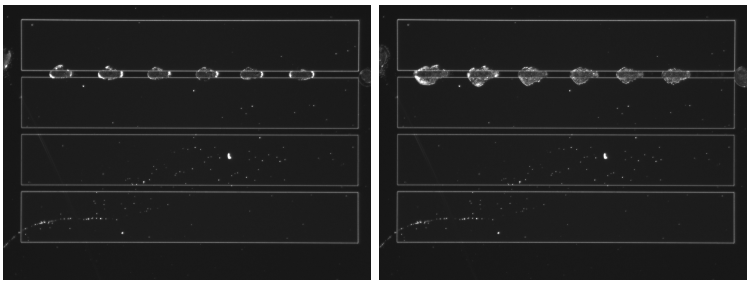

Figure 43: Inkjet printed MoS_2 NF suspension (GS-MDS-NF) on Cr/SiO_2. One layer (left) and two layers (right) printed with 10 μm droplet separation along a 2 mm wide device with $L = 40\,\mu$m channel length. The printed droplets reflowed after printing and formed larger droplets rather than dry in place.

Another approach is printing a high enough volume to coat the device as a whole (Figure 42d), but ring-stain considerations would be similar as in the case of drop-casted devices.

All printed devices described above did not have measurable channel conductance or field effect. This can be attributed to a too low surface density of MoS_2 or to a possible physical gap between the electrodes and the dry film, similar to what was observed in the case of drop-casting.

III.4.3 Circular devices

An obvious ring-stain is formed during the drying process of droplets of nanosheet MoS_2 suspensions. The naturally forming ring-stain can be exploited for bottom contact device fabrication of circular devices. When the surface energy of the insulator is higher than the surface energy of the metal electrodes, the contact line of deposited droplets can be pinned between two concentric electrodes, such that the ring-stain forms a continuous channel between the two electrodes (Figure 44a).

In order to pin a deposited droplet along a circular channel, the diameter of the device must be similar in size to the diameter of the droplet, otherwise the droplet would migrate towards the more favourable oxide surface. While drop-casted circular devices require large patterns, inkjet printed circular devices can have a much smaller footprint, due to the lower deposited volume. The low volumes evaporate significantly faster, which enables rapid subsequent deposition.

Time lapse photos of the drying process revealed that during drying, the contact line of the droplet assumed discrete positions corresponding to the bare SiO_2 concentric strips (Figure 45). At each pinned

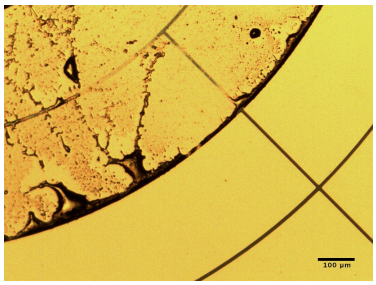

(a) Optical micrograph of a ring-stain "pinned" to the SiO_2 channel gap between concentric metal patterns, formed by multiple drop-casted drops.

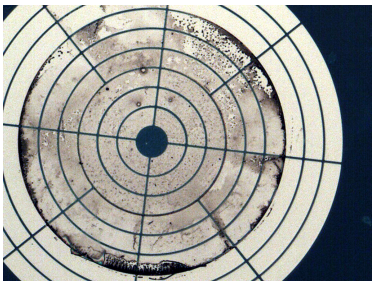

(b) Inkjet printing on Cr contacts with $5\,\mu$m channel length. Much of the suspended MoS_2 settled at the droplet edge (device channel).

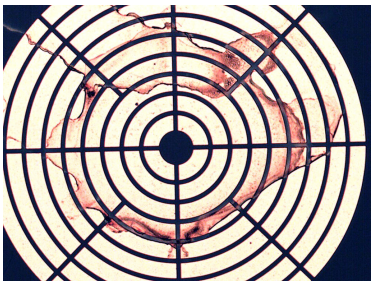

(c) Inkjet printing on Au contacts (Cr adhesion layer) with $10\,\mu$m channel length. Surface energy difference between SiO_2 and Au is too low such that no pinning is observed. Au contacts can therefore be useful for conventional rectangular patterns.

Figure 44: Circular device geometry for pinning deposited droplets at certain diameters.

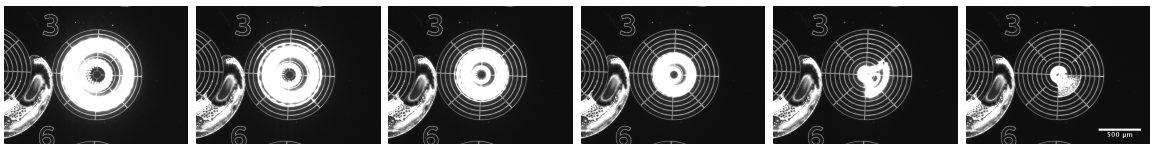

Figure 45: Time lapse of a printed MoS_2 suspension while drying on SiO_2 with Cr electrodes. Well-centred deposition confines the droplet pinning locations to the various channel gaps, taking advantage of the ring-stain effect to encourage deposition there. Scale bar is $500\,\mu$m.

diameter, suspended material is transported towards the contact line and deposited in the channel during the pinning duration. Therefore, a droplet of sufficient volume can be used for forming several channels of concentric devices.

Several observations can be made from SEM images of printed circular devices (Figures 46a, 46b). In Figure 46a, a clear contrast between the deposited film (dark) and the substrate (bright) is visible outside the channel region (on the right of the channel). This indicates that the deposited droplet was pinned to the channel region and the suspended MoS_2 was efficiently transported towards the droplet edge. The channel area appears to be covered by a continuous film with a relatively uniform surface density. The film extends to the left (away from the centre) because the effective deposition area near the contact line is larger than the channel length. The other side of this picture can be seen in Figure 46b, where formation of two regions inside the channel, a ring with a higher surface density and a ring with a lower surface density, can be observed (ring-stain within a ring-stain). As the electrode next to the high density ring is clean of any deposits, it is clear that the contact line of the droplet was pinned precisely along that interface. The thickness of the higher density ring is only $2\,\mu$m, such that it cannot induce bulk conductivity along the $10\,\mu$m channel. The lower density ring, however, may still be thick enough to induce bulk conductivity. While the channels of some devices were conductive, no field effect was observed in any of the circular

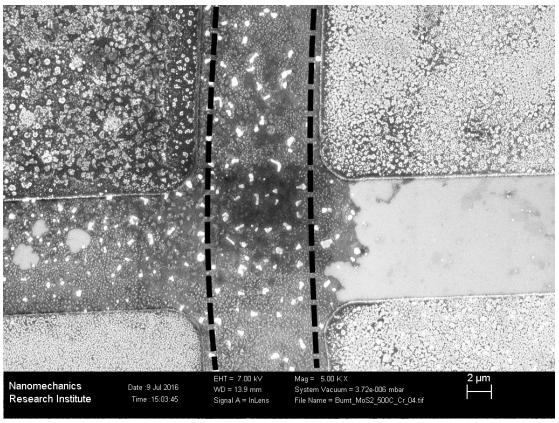

(a) SEM image of the channel area of a circular device (device centre is on the right), clearly showing the dark MoS_2 film on the background of the bright SiO_2 substrate. The channel is marked by dashed lines.

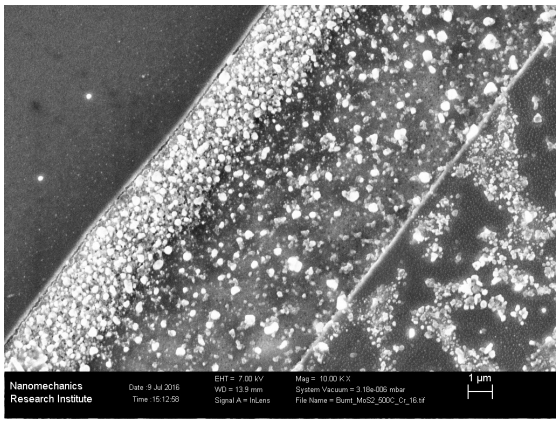

(b) SEM image of the channel area (centre) between two electrodes (left and right), showing non-uniform material density along the channel length.

Figure 46: Ring-stains of drop-casted MoS_2 suspensions on circular patterns on a 50°C hotplate. The SEM images were taken after a 500°C anneal (no other images were available at the time of writing).

devices. The channel thickness in circular devices, which are based on the ring-stain effect, may be quite high. In order to reduce bulk conductance, thinning down of the channel thickness by RIE in SF_6 can be explored in future research.

Finally, both Figure 46a and 46b reveal that the deposited film does not show any step coverage, and Figure 46b reveals that a gap can be formed between the deposited film and the electrode, compromising charge transport between the electrode and the film. This can explain why no current was measured in some devices. While efficient for constraining material deposition along circular trajectories, circular metallic patterns do not result in consistently high quality electrode-film interface. Therefore, in order to use circular devices for prototyping colloidal inks with bottom contact architectures, a consistent method for obtaining high quality contacts needs to be developed in future studies.

III.4.3.1 Instability

Devices comprised of circular patterns were originally hypothesized to have a stabilizing effect on deposited droplets, correcting any off-centred deposition by a net radial force towards the centre. An opposite effect was observed experimentally and confirmed in simulation (Figure 47). Due to an excess of deposited volume and an off-centred initial position, the droplet ended up predominately on the more energy favourable SiO_2 substrate. The same phenomenon was reproduced in simulation for much smaller droplets as well: off-centre radial migration is observed as long as the droplet is large enough to span several channel gap arcs. While HyDro is not a time domain simulation, the iteration parameter has some correlation with time

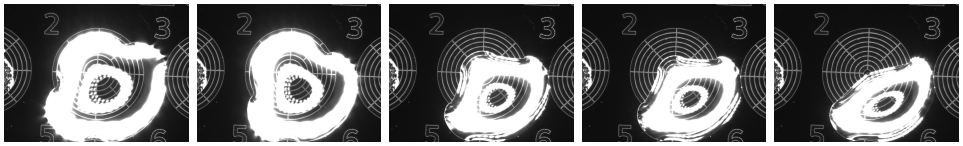

(a) Drying time-lapse of a printed droplet.

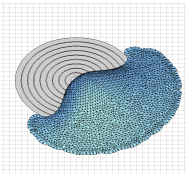

(b) Simulation of (a).

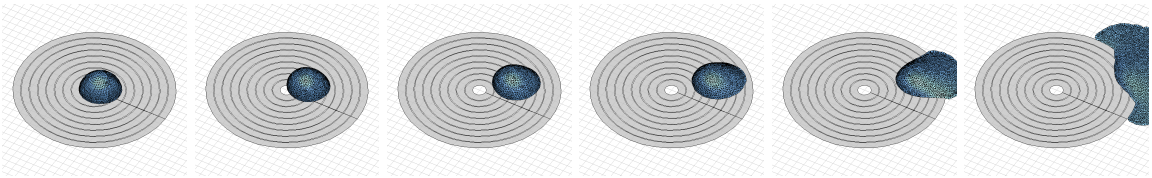

(c) Convergence process of a smaller volume ($\Omega = 3.8\,\mu$L) droplet, at 100, 1000, 1500, 1700, 1900 and 2100 timesteps (from left to right). The droplet "accelerates" away from the centre with increasing number of iterations.

Figure 47: Qualitative comparison between experimental results (a) and simulated wetting (b) for off-centred deposition on circular Cr electrodes pattern with channel length of $5\,\mu$m on SiO_2 surface. HyDro wetting simulations were run with droplet volume $\Omega = 38\,\mu$L, $\gamma = 30\,\mathrm{mN}\cdot\mathrm{m}^{-1}$, $\theta_c = 20°$ on the pattern and $\theta_c = 1°$ on the substrate. Simulated droplet was initially positioned $15\,\mu$m off-centre and the simulation was aborted midway to capture the "escape" phenomena; the fully equilibrated state is when the droplet is fully outside the device. Detailed timestep evolution for a smaller droplet with $\Omega = 3.8\,\mu$L is presented in (c).

evolution, as both converge to the steady-state solution. Interestingly, the simulated "dynamic" contact angle on the pattern is higher than the set $\theta_c = 20°$, suggesting that the alternating surface energy areas contribute to hydrophobicity. Applications of this phenomena could include self-arrangement of printed devices, self-cleaning surfaces, sophisticated flow control in microfluidics and more.

III.5 Discussion

Both top contact and bottom contact devices, either drop-casted or printed, exhibited poor conductivity and no field-effect switching. One possible reason for this could be poor inter-sheet charge transport due to the way the MoS_2 nanosheets are stacked in deposited films. This could explain the high resistance measured for top contact devices even for thick films. In addition, for bottom contact devices, a poor contact between the electrodes and the nanosheet film due to poor step-coverage or a physical gap may hamper conduction, as observed for printed circular devices. Typical thickness for robust electrodes is around 100 nm, which is similar to the mean nanosheet size of both the commercial suspension and the in-house suspension. Therefore, step coverage of bottom contact electrodes may not be attainable.

Several devices, e.g. circular devices, exhibit channel conductivity but no field-effect, possibly due to the thick layer of MoS_2 that was collected in the channel and allowed bulk conductivity to occur. Thinning down of the film thickness in the channel, e.g. via RIE, could be a viable option for future study.

Another contributing factor to the high channel resistance in bottom contact devices is the thin oxide layer that is immediately formed on exposed surfaces, especially chromium [94]. The few-nm thick oxide layer is small enough to transport charge through tunnelling (otherwise bulk conductivity would not be observed), but such transport results in reduced conductivity compared to an direct interface with the metal.

Therefore, top contact architecture with a thin film of tightly packed sheets is desirable. Spray coating of MoS_2 nanosheets could be attempted for forming a high quality thin film in future studies.

Part IV

Conclusions and future work

IV.1 Conclusions

MoS_2 thin-film transistors are difficult to fabricate. Single-sheet devices have high performance but their fabrication yield is low and inconsistent, and solution-processable micro-scale sheets are difficult to exfoliate and to stabilize in suspension. Therefore, nano-scale sheets are commonly used as the base material for solution-processable device fabrication. Nano-scale sheets are easy to exfoliate and stabilize in suspension but it is challenging to form a high quality thin film of tightly stacked nanosheets. To date, no field-effect transistors based on nano-scale sheets with practical performance were reported. In order to address these challenges, several approaches were taken.

To improve film properties via annealing, it was necessary to find the decomposition temperature of MoS_2 nanosheets, which is different from bulk MoS_2. To the best of my knowledge, this research is the first study that explores the decomposition temperature of nanosheet MoS_2. It was shown that the study of thermal stability should be a standard procedure in process development for nanosheet materials, as it reveals crucial limitations on processing. For the first time, a thermal decomposition study was carried out for MoS_2 nanosheets. Low oxidation and decomposition temperatures of nanosheet MoS_2 limited processing to 150-200°C in air and to 300°C in inert atmosphere. Since relaxation of MoS_2 from its metallic 1T phase to the semiconducting 2H phase requires annealing at up to 300°C, attempting a relaxation step in air would result in an oxidized film.

The minimal MoS_2 concentration needed to bridge a channel gap was estimated using continuum percolation simulation, from which the minimum number of deposited layers to obtain a continuous network of nanosheets was calculated. For the first time, percolation simulations with a random particle size distribution, based on a real distribution from DLS measurements, were performed and studied. It was found that the percolation threshold for the nanosheets used is reached at areal coverage of slightly under 60%.

Top-gate and bottom-gate devices were fabricated. It was shown that the colloidal properties of suspended particles play a major role in film uniformity and ring-stain formation during the drying process of droplets. Circular devices were designed especially to collect MoS_2 nanosheets in the channel gap of a device. To the best of my knowledge, this was the first time a circular device was used to exploit the ring-stain effect. Improving the interface between the electrodes and the deposited film in circular devices,

as well as thinning down of the channel thickness, should be studied to reduce the channel resistance and the bulk conductivity.

The availability of commercial MoS_2 inks is extremely low. During this research only one product was commercially available. Recent publications employing larger MoS_2 sheets demonstrated a promising route towards the commercial synthesis of suspensions of large sheets, which would provide higher flexibility to processing efforts for device fabrication. Pre-expansion [24], optimized exfoliation solvents [1] and electrostatic repulsion agents [38] are promising methods to increase the average sheet size, which in turn would reduce the number of inter-sheet transport events and increase channel conductivity. Having more commercial suspensions to choose from would offer higher flexibility for process development.

IV.2 Future work

IV.2.1 Influence of colloidal properties on film formation

The size and concentration of nanosheets in suspension, as well as presence of a modifier such as ethyl cellulose, had observable influence on film uniformity, agglomeration and ring-stain thickness. While experimental results are straightforward to obtain, it is necessary to develop theoretical models in order to be able to make useful predictions with a large range of materials and parameters. An in-depth study of the influence of colloidal properties of the suspended nanosheets on drying dynamics and ring-stain formation in various dispersion mediums is therefore of interest.

IV.2.2 Improving contact between nanosheet films and bottom-contact electrodes

Bottom-contact electrodes offer several advantages. As they are deposited on a clean insulating substrate, any patterning method can be used, in particular photolithography, with which small features can be patterned. The most delicate step – the deposition of the semiconducting thin film – is the last deposition step, which limits its exposure to potentially harsh environments. As shown above, the patterned metal electrodes can be used as surface energy modifiers for circular devices. Therefore, developing processes for improved contact between the nanosheet film and the electrodes would enable the use of the aforementioned advantages. However, the use of gold (with or without an adhesion layer) as an inert bottom contact material may be required to prevent the formation of an oxide layer on the metal surface.

IV.2.3 Spray coated films

While inkjet printing is particularly suitable for depositing the channel material for bottom contact devices, spray coating is useful for large-area coating of a channel material for top contact devices. When the sprayed solvent evaporates fast enough after spraying, no ring-stain effect is observed, which is advantageous for forming uniform films across large areas. Moreover, the fast stream of air may improve the stacking of the nanosheets in the film. Spray coating is therefore a more viable approach for this purpose than drop casting and inkjet printing.

Recently, Coleman *et al.* [1] used spray coating for depositing networks of $\sim 500\,\mathrm{nm}$-wide sheets of WSe_2 as the channel layer in electrolyte-gated TFTs.

Preliminary results of a spray-coated MoS_2 film are presented in Figure 48. Several horizontal slices are presented, demonstrating that a continuous film is formed at the substrate level and that above a

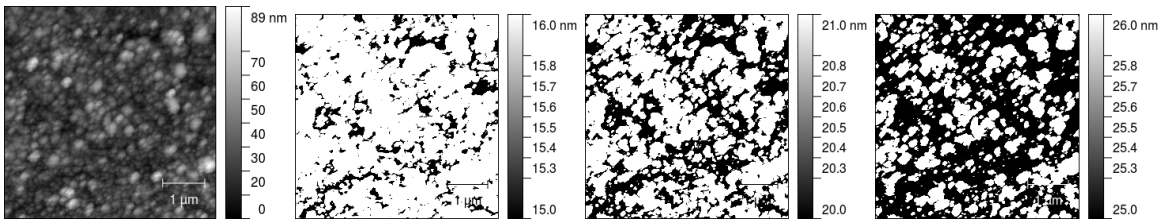

Figure 48: AFM image of spray coated MoS_2 nanosheet suspension on SiO_2 substrate, from left to right: original AFM image with peak height of 90 nm, a horizontal slice in the range $15 \leq z \leq 16$ nm, a horizontal slice in the range $20 \leq z \leq 21$ nm, a horizontal slice in the range $25 \leq z \leq 26$ nm. In the last slice (right), the surface coverage is approximately 60%.

thickness of 25 nm, the projected areal coverage drops below percolation threshold. Although the maximum measured thickness reaches up to 90 nm, the effective film thickness is only 25 nm, limiting the onset of bulk conductivity. This is a promising result for potential top-contact device fabrication and could be studied further.

IV.2.4 Electric properties as a function of film thickness

The absence of a field-effect was observed in both extremely thin films and thick films. An in-depth study of the electric properties of thin MoS_2 nanosheet films as a function of film thickness is of interest. Spray coating, for example, may be a useful method for additive deposition of controllable film thicknesses for such a study. Another approach could be gradual thinning-down of thick MoS_2 films which initially exhibit metallic properties. Thinning down of MoS_2 can be achieved using dry etching.

References

[1] Adam G. Kelly, Toby Hallam, Claudia Backes, Andrew Harvey, Amir Sajad Esmaeily, Ian Godwin, João Coelho, Valeria Nicolosi, Jannika Lauth, Aditya Kulkarni, Sachin Kinge, Laurens D. A. Siebbeles, Georg S. Duesberg, and Jonathan N. Coleman. All-printed thin-film transistors from networks of liquid-exfoliated nanosheets. *Science*, 356(6333):69–73, April 2017.

[2] Kourosh Kalantar-zadeh, Jian Zhen Ou, Torben Daeneke, Michael S. Strano, Martin Pumera, and Sally L. Gras. Two-Dimensional Transition Metal Dichalcogenides in Biosystems. *Advanced Functional Materials*, 25(32):5086–5099, August 2015.

[3] Zhiming M. Wang, editor. *MoS2 - Materials, Physics, and Devices*, volume 21 of *Lecture Notes in Nanoscale Science and Technology*. Springer, 2014.

[4] Jonathan N. Coleman, Mustafa Lotya, Arlene O'Neill, Shane D. Bergin, Paul J. King, Umar Khan, Karen Young, Alexandre Gaucher, Sukanta De, Ronan J. Smith, Igor V. Shvets, Sunil K. Arora, George Stanton, Hye-Young Kim, Kangho Lee, Gyu Tae Kim, Georg S. Duesberg, Toby Hallam, John J. Boland, Jing Jing Wang, John F. Donegan, Jaime C. Grunlan, Gregory Moriarty, Aleksey Shmeliov, Rebecca J. Nicholls, James M. Perkins, Eleanor M. Grieveson, Koenraad Theuwissen, David W. McComb, Peter D. Nellist, and Valeria Nicolosi. Two-Dimensional Nanosheets Produced by Liquid Exfoliation of Layered Materials. *Science*, 331(6017):568–571, February 2011.

[5] Arjan van der Bos, Mark-Jan van der Meulen, Theo Driessen, Marc van den Berg, Hans Reinten, Herman Wijshoff, Michel Versluis, and Detlef Lohse. Velocity Profile inside Piezoacoustic Inkjet Droplets in Flight: Comparison between Experiment and Numerical Simulation. *Physical Review Applied*, 1(1):014004, February 2014.

[6] Brian Derby. Inkjet Printing of Functional and Structural Materials: Fluid Property Requirements, Feature Stability, and Resolution. *Annual Review of Materials Research*, 40(1):395–414, 2010.

[7] QuantumWise. Crystal Structure Prediction Scripter: Phases of TiO2 — QuantumWise 2016.4 documentation, 2016.

[8] Jiantong Li. Percolation thresholds of two-dimensional continuum systems of rectangles. *Physical Review E*, 88(1), 2013.

[9] Graphene Supermarket. Molybdenum Disulfide (MoS2) Pristine Flakes in Solution, 100 ml, 2017.

[10] Qing Hua Wang, Kourosh Kalantar-Zadeh, Andras Kis, Jonathan N. Coleman, and Michael S. Strano. Electronics and optoelectronics of two-dimensional transition metal dichalcogenides. *Nature Nanotechnology*, 7(11):699–712, November 2012.

[11] Andrei Sazonov, Denis Striakhilev, and Arokia Nathan. Low-temperature Amorphous and Nanocrystalline Silicon Materials and Thin-film Transistors. In William S. Wong and Alberto Salleo, editors, *Flexible Electronics*, number 11 in Electronic Materials: Science & Technology, pages 53–73. Springer US, 2009. DOI: 10.1007/978-0-387-74363-9_3.

[12] S.D. Brotherton. *Introduction to Thin Film Transistors - Physics and Technology of TFTs*. Condensed Matter Physics. Springer, 2013.

[13] Helena Gleskova, I.-Chun Cheng, Sigurd Wagner, and Zhigang Suo. Mechanical Theory of the Film-on-Substrate-Foil Structure: Curvature and Overlay Alignment in Amorphous Silicon Thin-Film Devices Fabricated on Free-Standing Foil Substrates. In William S. Wong and Alberto Salleo, editors, *Flexible Electronics*, number 11 in Electronic Materials: Science & Technology, pages 29–51. Springer US, 2009. DOI: 10.1007/978-0-387-74363-9_2.

[14] William S. Wong, Michael L. Chabinyc, Tse-Nga Ng, and Alberto Salleo. Materials and Novel Patterning Methods for Flexible Electronics. In William S. Wong and Alberto Salleo, editors, *Flexible Electronics*, number 11 in Electronic Materials: Science & Technology, pages 143–181. Springer US, 2009. DOI: 10.1007/978-0-387-74363-9_6.

[15] Ana Claudia Arias, J. Devin MacKenzie, Iain McCulloch, Jonathan Rivnay, and Alberto Salleo. Materials and Applications for Large Area Electronics: Solution-Based Approaches. *Chemical Reviews*, 110(1):3–24, January 2010.

[16] Valeria Nicolosi, Manish Chhowalla, Mercouri G. Kanatzidis, Michael S. Strano, and Jonathan N. Coleman. Liquid Exfoliation of Layered Materials. *Science*, 340(6139):1226419, June 2013.

[17] Francesco Bonaccorso, Antonino Bartolotta, Jonathan N. Coleman, and Claudia Backes. 2d-Crystal-Based Functional Inks. *Advanced Materials*, 28(29):6136–6166, August 2016.

[18] Saptarshi Das, Hong-Yan Chen, Ashish Verma Penumatcha, and Joerg Appenzeller. High Performance Multilayer MoS2 Transistors with Scandium Contacts. *Nano Letters*, 13(1):100–105, January 2013.

[19] Song Yu Wang, Tsung Shine Ko, Cheng Ching Huang, Der Yuh Lin, and Ying Sheng Huang. Optical and electrical properties of MoS2 and Fe-doped MoS2. *Japanese Journal of Applied Physics*, 53(4S):04EH07, March 2014.

[20] Yung-Chang Lin, Dumitru O. Dumcenco, Ying-Sheng Huang, and Kazu Suenaga. Atomic mechanism of the semiconducting-to-metallic phase transition in single-layered MoS2. *Nature Nanotechnology*, 9(5):391–396, May 2014.

[21] Jun Suk Kim, Jaesu Kim, Jiong Zhao, Sungho Kim, Jin Hee Lee, Youngjo Jin, Homin Choi, Byoung Hee Moon, Jung Jun Bae, Young Hee Lee, and Seong Chu Lim. Electrical Transport Properties of Polymorphic MoS2. *ACS Nano*, 10(8):7500–7506, August 2016.

[22] Damien Voiry, Anandarup Goswami, Rajesh Kappera, Cecilia de Carvalho Castro e Silva, Daniel Kaplan, Takeshi Fujita, Mingwei Chen, Tewodros Asefa, and Manish Chhowalla. Covalent functionalization of monolayered transition metal dichalcogenides by phase engineering. *Nature Chemistry*, 7(1):45–49, January 2015.

[23] R. S. Czernuszewicz and T. G. Spiro. IR, Raman, and Resonance Raman Spectroscopy. In Edward I. Solomon and A. B. P. Lever, editors, *Inorganic Electronic Structure and Spectroscopy, Volume I: Methodology*, pages 353–442. February 2006.

[24] Jian Zheng, Han Zhang, Shaohua Dong, Yanpeng Liu, Chang Tai Nai, Hyeon Suk Shin, Hu Young Jeong, Bo Liu, and Kian Ping Loh. High yield exfoliation of two-dimensional chalcogenides using sodium naphthalenide. *Nature Communications*, 5:2995, January 2014.

[25] Keng-Ku Liu, Wenjing Zhang, Yi-Hsien Lee, Yu-Chuan Lin, Mu-Tung Chang, Ching-Yuan Su, Chia-Seng Chang, Hai Li, Yumeng Shi, Hua Zhang, Chao-Sung Lai, and Lain-Jong Li. Growth of Large-Area and Highly Crystalline MoS2 Thin Layers on Insulating Substrates. *Nano Letters*, 12(3):1538–1544, March 2012.

[26] B. Radisavljevic, A. Radenovic, J. Brivio, V. Giacometti, and A. Kis. Single-layer MoS2 transistors. *Nature Nanotechnology*, 6(3):147–150, March 2011.

[27] Oriol Lopez-Sanchez, Dominik Lembke, Metin Kayci, Aleksandra Radenovic, and Andras Kis. Ultrasensitive photodetectors based on monolayer MoS2. *Nature Nanotechnology*, 8(7):497–501, July 2013.

[28] M. M. Benameur, B. Radisavljevic, J. S. Héron, S. Sahoo, H. Berger, and A. Kis. Visibility of dichalcogenide nanolayers. *Nanotechnology*, 22(12):125706, 2011.

[29] Jingying Zheng, Xingxu Yan, Zhixing Lu, Hailong Qiu, Guanchen Xu, Xu Zhou, Peng Wang, Xiaoqing Pan, Kaihui Liu, and Liying Jiao. High-Mobility Multilayered MoS2 Flakes with Low Contact Resistance Grown by Chemical Vapor Deposition. *Advanced Materials*, 29(13):n/a–n/a, April 2017.

[30] Stefan Wachter, Dmitry K. Polyushkin, Ole Bethge, and Thomas Mueller. A microprocessor based on a two-dimensional semiconductor. *Nature Communications*, 8:14948, April 2017.

[31] Yu-Chuan Lin, Wenjing Zhang, Jing-Kai Huang, Keng-Ku Liu, Yi-Hsien Lee, Chi-Te Liang, Chih-Wei Chu, and Lain-Jong Li. Wafer-scale MoS 2 thin layers prepared by MoO 3 sulfurization. *Nanoscale*, 4(20):6637–6641, 2012.

[32] Ke-Jing Huang, Ji-Zong Zhang, Gang-Wei Shi, and Yan-Ming Liu. Hydrothermal synthesis of molybdenum disulfide nanosheets as supercapacitors electrode material. *Electrochimica Acta*, 132:397–403, June 2014.

[33] Yagang Yao, Lorenzo Tolentino, Zhongzheng Yang, Xiaojuan Song, Wen Zhang, Yongsheng Chen, and Ching-ping Wong. High-Concentration Aqueous Dispersions of MoS2. *Advanced Functional Materials*, 23(28):3577–3583, July 2013.

[34] Jiantong Li, Maziar M. Naiini, Sam Vaziri, Max C. Lemme, and Mikael Östling. Inkjet Printing of MoS2. *Advanced Functional Materials*, 24(41):6524–6531, November 2014.

[35] Jiantong Li, Max C. Lemme, and Mikael Östling. Inkjet Printing of 2d Layered Materials. *ChemPhysChem*, 15(16):3427–3434, November 2014.

[36] Kirill Arapov, Robert Abbel, Gijsbertus de With, and Heiner Friedrich. Inkjet printing of graphene. *Faraday Discussions*, 173(0):323–336, December 2014.

[37] Yahui Gao, Wen Shi, Wucong Wang, Yuanpeng Leng, and Yaping Zhao. Inkjet Printing Patterns of Highly Conductive Pristine Graphene on Flexible Substrates. *Industrial & Engineering Chemistry Research*, 53(43):16777–16784, October 2014.

[38] Yu-Xiang Chen, Chien-Wei Wu, Ting-Yang Kuo, Yu-Lung Chang, Ming-Hsing Jen, and I.-Wen Peter Chen. Large-Scale Production of Large-Size Atomically Thin Semiconducting Molybdenum Dichalcogenide Sheets in Water and Its Application for Supercapacitor. *Scientific Reports*, 6:26660, May 2016.

[39] Sybille Allard, Michael Forster, Benjamin Souharce, Heiko Thiem, and Ullrich Scherf. Organic Semiconductors for Solution-Processable Field-Effect Transistors (OFETs). *Angewandte Chemie International Edition*, 47(22):4070–4098, May 2008.

[40] Yana Aleeva and Bruno Pignataro. Recent advances in upscalable wet methods and ink formulations for printed electronics. *Journal of Materials Chemistry C*, 2(32):6436–6453, 2014.

[41] Wei Xu, Zhanhao Hu, Huimin Liu, Linfeng Lan, Junbiao Peng, Jian Wang, and Yong Cao. Flexible All-organic, All-solution Processed Thin Film Transistor Array with Ultrashort Channel. *Scientific Reports*, 6:29055, July 2016.

[42] Joseph T. Delaney, Patrick J. Smith, and Ulrich S. Schubert. Inkjet printing of proteins. *Soft Matter*, 5(24):4866–4877, 2009.

[43] Berend-Jan de Gans and Ulrich S. Schubert. Inkjet Printing of Polymer Micro-Arrays and Libraries: Instrumentation, Requirements, and Perspectives. *Macromolecular Rapid Communications*, 24(11):659–666, July 2003.

[44] Maria Prudenziati and Jacob Hormadaly, editors. *Printed Films: Materials Science and Applications in Sensors, Electronics and Photonics*. Elsevier, August 2012. Google-Books-ID: zX9wAgAAQBAJ.

[45] C. E. Mora-Huertas, H. Fessi, and A. Elaissari. Polymer-based nanocapsules for drug delivery. *International Journal of Pharmaceutics*, 385(1–2):113–142, January 2010.

[46] Ronan Daly, Tomás S. Harrington, Graham D. Martin, and Ian M. Hutchings. Inkjet printing for pharmaceutics – A review of research and manufacturing. *International Journal of Pharmaceutics*, 494(2):554–567, October 2015.

[47] A. Capasso, A. E. Del Rio Castillo, H. Sun, A. Ansaldo, V. Pellegrini, and F. Bonaccorso. Inkjet printing of graphene for flexible electronics: An environmentally-friendly approach. *Solid State Communications*, 224:53–63, December 2015.

[48] Yuzhi Li, Linfeng Lan, Peng Xiao, Sheng Sun, Zhenguo Lin, Wei Song, Erlong Song, Peixiong Gao, Weijing Wu, and Junbiao Peng. Coffee-Ring Defined Short Channels for Inkjet-Printed Metal Oxide Thin-Film Transistors. *ACS Applied Materials & Interfaces*, 8(30):19643–19648, August 2016.

[49] In Ho Choi, Young Kwon Kim, Sangmin Lee, Seung Hee Lee, and Joonwon Kim. A Pneumatic Drop-on-Demand Printing System With an Extended Printable Liquid Range. *Journal of Microelectromechanical Systems*, 24(4):768–770, August 2015.

[50] Paul Calvert. Inkjet Printing for Materials and Devices. *Chemistry of Materials*, 13(10):3299–3305, October 2001.

[51] Fujifilm USA. Dimatix Materials Printer DMP-2850, 2016.

[52] David Quéré. Non-sticking drops. *Reports on Progress in Physics*, 68(11):2495, 2005.

[53] Hua Hu and Ronald G. Larson. Marangoni Effect Reverses Coffee-Ring Depositions. *The Journal of Physical Chemistry B*, 110(14):7090–7094, April 2006.

[54] Xiaoying Shen, Chih-Ming Ho, and Tak-Sing Wong. Minimal Size of Coffee Ring Structure. *The Journal of Physical Chemistry B*, 114(16):5269–5274, April 2010.

[55] Berend-Jan de Gans and Ulrich S. Schubert. Inkjet Printing of Well-Defined Polymer Dots and Arrays. *Langmuir*, 20(18):7789–7793, August 2004.

[56] Dan Soltman and Vivek Subramanian. Inkjet-Printed Line Morphologies and Temperature Control of the Coffee Ring Effect. *Langmuir*, 24(5):2224–2231, March 2008.

[57] Saeed Jafari Kang, Vahid Vandadi, James D. Felske, and Hassan Masoud. Alternative mechanism for coffee-ring deposition based on active role of free surface. *Physical Review E*, 94(6):063104, December 2016.

[58] Peter J. Yunker, Tim Still, Matthew A. Lohr, and A. G. Yodh. Suppression of the coffee-ring effect by shape-dependent capillary interactions. *Nature*, 476(7360):308–311, August 2011.

[59] Alexander Kamyshny and Shlomo Magdassi. Inkjet Ink Formulations. In Jan G. Korvink, Patrick J. Smith, and Dong-Youn Shin, editors, *Inkjet-Based Micromanufacturing*, pages 173–189. Wiley-VCH Verlag GmbH & Co. KGaA, 2012. DOI: 10.1002/9783527647101.ch12.

[60] Ian M. Hutchings and Graham D. Martin. *Inkjet Technology for Digital Fabrication*. Wiley, Chichester, West Sussex, United Kingdom, December 2012.

[61] Daryl McManus, Sandra Vranic, Freddie Withers, Veronica Sanchez-Romaguera, Massimo Macucci, Huafeng Yang, Roberto Sorrentino, Khaled Parvez, Seok-Kyun Son, Giuseppe Iannaccone, Kostas Kostarelos, Gianluca Fiori, and Cinzia Casiraghi. Water-based and biocompatible 2d crystal inks for all-inkjet-printed heterostructures. *Nature Nanotechnology*, 12(4):343–350, May 2017.

[62] M. Serdar Onses, Erick Sutanto, Placid M. Ferreira, Andrew G. Alleyne, and John A. Rogers. Mechanisms, Capabilities, and Applications of High-Resolution Electrohydrodynamic Jet Printing. *Small*, 11(34):4237–4266, September 2015.

[63] CERADROP. CERADROP Materials Deposition Digital Printers, 2016.

[64] microdrop Technologies GmbH. Microarray printing, biochip spotting on Autodrop positioning systems, 2016.

[65] MicroFab Technologies. Complete Systems, 2016.

[66] Alexander A. Bessonov, Marina N. Kirikova, Dmitrii I. Petukhov, Mark Allen, Tapani Ryhänen, and Marc J. A. Bailey. Layered memristive and memcapacitive switches for printable electronics. *Nature Materials*, 14(2):199–204, February 2015.

[67] Yeonwoong Jung, Yu Zhou, and Judy J. Cha. Intercalation in two-dimensional transition metal chalcogenides. *INORGANIC CHEMISTRY*, January 2016.

[68] Peter N. Nirmalraj, Tarek Lutz, Shishir Kumar, Georg S. Duesberg, and John J. Boland. Nanoscale Mapping of Electrical Resistivity and Connectivity in Graphene Strips and Networks. *Nano Letters*, 11(1):16–22, January 2011.

[69] Eric Farrell and Jean-Luc Brousseau. Guide for DLS sample preparation v5, January 2014.

[70] Arlene O'Neill, Umar Khan, and Jonathan N Coleman. Preparation of High Concentration Dispersions of Exfoliated MoS2 with Increased Flake Size. *Chemistry of Materials*, 24(12):2414–2421, June 2012.

[71] Claudia Backes, Beata M. Szydłowska, Andrew Harvey, Shengjun Yuan, Victor Vega-Mayoral, Ben R. Davies, Pei-liang Zhao, Damien Hanlon, Elton J. G. Santos, Mikhail I. Katsnelson, Werner J. Blau, Christoph Gadermaier, and Jonathan N. Coleman. Production of Highly Monolayer Enriched Dispersions of Liquid-Exfoliated Nanosheets by Liquid Cascade Centrifugation. *ACS Nano*, 10(1):1589–1601, January 2016.

[72] Peter Cannon. Melting Point and Sublimation of Molybdenum Disulphide. *Nature*, 183(4675):1612–1613, June 1959.

[73] W. H. Qi and M. P. Wang. Size and shape dependent melting temperature of metallic nanoparticles. *Materials Chemistry and Physics*, 88(2–3):280–284, December 2004.

[74] D. Liu, Y. Guo, L. Fang, and J. Robertson. Sulfur vacancies in monolayer MoS2 and its electrical contacts. *Applied Physics Letters*, 103(18):183113, October 2013.

[75] Seoung-Ki Lee, Ho Young Jang, Sukjae Jang, Euiyoung Choi, Byung Hee Hong, Jaichan Lee, Sungho Park, and Jong-Hyun Ahn. All Graphene-Based Thin Film Transistors on Flexible Plastic Substrates. *Nano Letters*, 12(7):3472–3476, July 2012.

[76] Sunkook Kim, Aniruddha Konar, Wan-Sik Hwang, Jong Hak Lee, Jiyoul Lee, Jaehyun Yang, Changhoon Jung, Hyoungsub Kim, Ji-Beom Yoo, Jae-Young Choi, Yong Wan Jin, Sang Yoon Lee,

Debdeep Jena, Woong Choi, and Kinam Kim. High-mobility and low-power thin-film transistors based on multilayer MoS2 crystals. *Nature Communications*, 3:1011, August 2012.

[77] Yuanyue Liu, Paul Stradins, and Su-Huai Wei. Van der Waals metal-semiconductor junction: Weak Fermi level pinning enables effective tuning of Schottky barrier. *Science Advances*, 2(4):e1600069, April 2016.

[78] Raymond T. Tung. The physics and chemistry of the Schottky barrier height. *Applied Physics Reviews*, 1(1):011304, January 2014.

[79] Antoine Kahn. Fermi level, work function and vacuum level. *Materials Horizons*, 3(1):7–10, 2016.

[80] Wenzhong Bao, Xinghan Cai, Dohun Kim, Karthik Sridhara, and Michael S. Fuhrer. High mobility ambipolar MoS2 field-effect transistors: Substrate and dielectric effects. *Applied Physics Letters*, 102(4):042104, January 2013.

[81] F. M. Smits. Measurement of Sheet Resistivities with the Four-Point Probe. *Bell System Technical Journal*, 37(3):711–718, May 1958.

[82] Sonia Vionnet-Menot, Claudio Grimaldi, Thomas Maeder, Sigfrid Strässler, and Peter Ryser. Tunneling-percolation origin of nonuniversality: Theory and experiments. *Physical Review B*, 71(6), 2005.

[83] NumPy developers. NumPy, 2017.

[84] SciPy developers. SciPy.org, 2017.

[85] Pythonware. Python Imaging Library (PIL), 2017.

[86] The Matplotlib development team. Matplotlib: Python plotting, 2017.

[87] W. Liu, J. Kang, W. Cao, D. Sarkar, Y. Khatami, D. Jena, and K. Banerjee. High-performance few-layer-MoS2 field-effect-transistor with record low contact-resistance. In *2013 IEEE International Electron Devices Meeting*, pages 19.4.1–19.4.4, December 2013.

[88] Rajesh Kappera, Damien Voiry, Sibel Ebru Yalcin, Brittany Branch, Gautam Gupta, Aditya D. Mohite, and Manish Chhowalla. Phase-engineered low-resistance contacts for ultrathin MoS2 transistors. *Nature Materials*, 13(12):1128–1134, December 2014.

[89] Benjamin J. Fischer. Particle Convection in an Evaporating Colloidal Droplet. *Langmuir*, 18(1):60–67, January 2002.

[90] Robert D. Deegan. Pattern formation in drying drops. *Physical Review E*, 61(1):475–485, 2000.

[91] 3M United States. Novec™ Electronic Grade Coatings, 2016.

[92] Hiroyuki Matsui, Yuki Noda, and Tatsuo Hasegawa. Hybrid Energy-Minimization Simulation of Equilibrium Droplet Shapes on Hydrophilic/Hydrophobic Patterned Surfaces. *Langmuir*, 28(44):15450–15453, November 2012.

[93] Ibrahim Sadek Khattab, Farzana Bandarkar, Mohammad Amin Abolghassemi Fakhree, and Abolghasem Jouyban. Density, viscosity, and surface tension of water+ethanol mixtures from 293 to 323k. *Korean Journal of Chemical Engineering*, 29(6):812–817, June 2012.

[94] G. Thurner and P.H. Holloway. Oxidation of polycrystalline chromium between 30c and 400c. *Acta Physica Polonica A*, 81(2), 1992.

[95] Hiroshi Fukuoka, Kumi Masuoka, Teruhiko Hanaoka, and Kei Inumaru. New Polymorph of Mo3s4 Prepared using a High-pressure Synthesis Technique: Crystal Structure, Electronic Property, and Band Calculation. *Inorganic Chemistry*, 52(14):7918–7922, July 2013.

[96] M. Potel, P. Gougeon, R. Chevrel, and M. Sergent. Labilité des cations dans les chalcogénures ternaires de molybdène: voies d'accès à de nouvelles synthèses. *Revue de chimie minérale*, 21(4):509–536, 1984.

[97] R. de Jonge, T. J. A. Popma, G. A. Wiegers, and F. Jellinek. Structure and phase transitions of molybdenum(III) sulfide and some related phases. *Journal of Solid State Chemistry*, 2(2):188–192, August 1970.

[98] Diala Salloum, Régis Gautier, Patrick Gougeon, and Michel Potel. Syntheses and structural trends of the InxMo15s19 (0?x?3.7) compounds containing Mo6 and Mo9 clusters. *Journal of Solid State Chemistry*, 177(4–5):1672–1680, April 2004.

[99] William W. Tipton and Richard G. Hennig. A grand canonical genetic algorithm for the prediction of multi-component phase diagrams and testing of empirical potentials. *Journal of Physics: Condensed Matter*, 25(49):495401, 2013.

[100] Jin-Wu Jiang, Harold S. Park, and Timon Rabczuk. Molecular dynamics simulations of single-layer molybdenum disulphide (MoS2): Stillinger-Weber parametrization, mechanical properties, and thermal conductivity. *Journal of Applied Physics*, 114(6):064307, August 2013.

Part V

Appendices

A Graphene Supermarket MoS_2 ink data sheet

The ink used throughout this research was "Molybdenum Disulphide (MoS_2) Pristine Flakes in Solution, 100 ML" from Graphene Supermarket (graphene-supermarket.com) [9]. The method of synthesis was not provided, but based on EDX analysis of the ink, it appears that sodium exfoliation was employed, due to the high sodium peak observed in the samples. According to Graphene Supermarket website, and to the best of my knowledge, the only publication that reported using this product was by Bessonov *et al.* [66].

The MoS_2 sheets are dispersed in 45 vol.% ethanol in water (v/v) with a reported concentration of $18\,\mathrm{mg}\cdot\mathrm{L}^{-1}$. The stated lateral size distribution is 100-400 nm, 1-8 layers thick.[21]

(a) MoS_2 suspension.

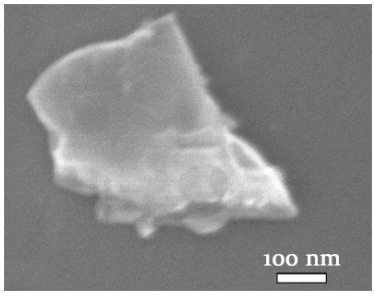

(b) SEM image of a single flake. This example flake appears much thicker than the reported 1-8 layers.

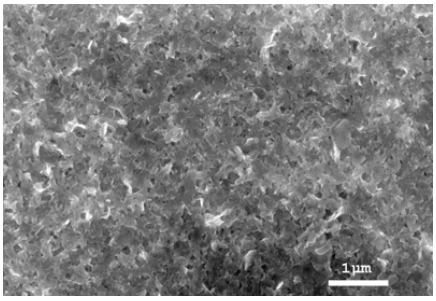

(c) SEM image of MoS_2 film on SiO_2.

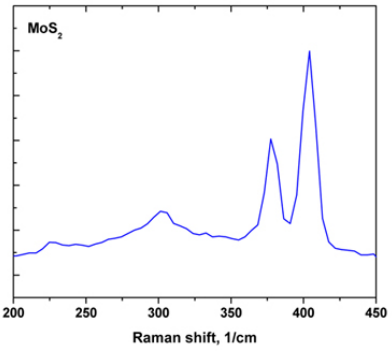

(d) Reported Raman spectrum of the MoS_2 ink.

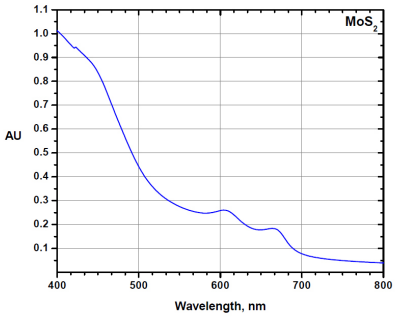

(e) Reported UV-vis absorption spectrum.

Figure 49: Graphene-Supermarket MoS_2 ink official data [9]. Copyright © 2009-2017 Graphene Supermarket.

[21] Based on DLS analysis, the number density of 100-400 nm is in fact negligible.

B Theoretically stable Mo_xS_y crystalline structures

Experimentally, Mo:S ratios of 1:1.27, 1:1.33, 1:1.45 were achieved at elevated temperatures (Figure 50). To evaluate the theoretical feasibility of nanocrystalline structures of other Mo:S ratios, a numerical method for energy minimization was employed.

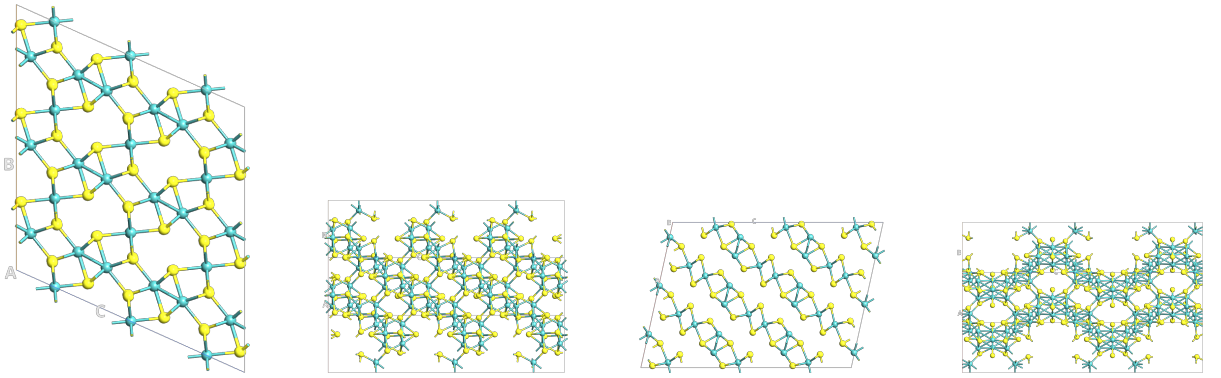

(a) Triclinic Mo_3S_4 (Mo:S $\sim$ 1 : 1.33), obtained at 13GPa, 1450°C. [95]

(b) Rhombohedral Mo_3S_4, obtained at low temperature by oxidation-reduction reactions. [96]

(c) Simple monoclinic $Mo_{2.06}S_3$ (Mo:S $\sim 1:1.45$), obtained by quenching to room temperature from 1300°C. [97]

(d) Hexagonal $Mo_{15}S_{19}$ (Mo:S $\sim$ 1 : 1.27), obtained by oxidation of $In_{3.7}Mo_{15}S_{19}$ at <300°C. [98]

Figure 50: Examples of experimentally stable Mo-S crystalline phases.

Various crystalline structures were generated and optimized using the Crystal Structure Prediction Scripter (CSPS) tool in Virtual NanoLab 2016.3 to predict stable crystal structures of bulk Mo_xS_y structures [7, 99]. The CSPS tool is using genetic algorithm to "evolve" "generations" of structures iteratively until minimal energy is reached. The first generation is a random pool of Mo and S crystals. The energy of the relaxed individuals is used to calculate the total energy. Every generation a "genetic operator" is applied, namely promotion (P), heredity (H), mutation (M) or permutation (X).

B.1 Input to genetic algorithm

1. The optimization runs consisted of unit cells with a formula of the form $(Mo_xS_y)_n$. The x:y ratios used were 1:2, 1:1, 3:2, 2:1, 5:2, 3:1, 4:1, 5:1 and 10:1, with n of 1 and 2.

2. 10 generations with a population size of 50 individuals were used in each generation. The reason only 10 generations were used is that typically the fitness values of the top few structures do not vary significantly beyond 10 generations. This was confirmed by evolving test cases up to 100 generations.

3. The number of directly promoted individuals between generations was set to 20.

4. The weight assigned to the genetic operators H:P:M was 50:20:30.

5. The potential used was a Stillinger-Weber (classical potential) [100].

Full details are provided in the script that was used to produce the data:

```
import numpy as np

# ------------------------------------------------------------
# Calculator
# ------------------------------------------------------------

potentialSet = StillingerWeber_MoS_2013()
calculator = TremoloXCalculator(parameters = potentialSet)
calculator.setVerletListsDelta(0.25*Angstrom)

# ------------------------------------------------------------
# Elements
# ------------------------------------------------------------

S = [Sulfur]; volS = 8.89 # Angstrom**3
Mo = [Molybdenum]; volMo = 18.41 # Angstrom**3

Mo_to_S_ratios = [(1,2), (1,1), (3,2), (2,1), (5,2), (3,1), (4,1), (5,1), (10,1)]
ratio_multipliers = [1,2]
fitness = []; ratio = []

for nMo, nS in Mo_to_S_ratios:
    for mult in ratio_multipliers:
        initial_volume = mult*(nMo*volMo + nS*volS)
        elements = S*nS*mult
        elements.extend(Mo*nMo*mult)
        num_of_atoms_in_unit_cell = mult*(nMo+nS)

        population_filename = "initial_population_(Mo%dS%d)%d_" % (nMo, nS, mult)
        generation_filename = "generation_(Mo%dS%d)%d_" % (nMo, nS, mult)

        # ------------------------------------------------------------
        # Random Number Generator
```

```
# ------------------------------------------------------------

rng = numpy.random.RandomState()

# ------------------------------------------------------------
# Initial Population
# ------------------------------------------------------------

initial_population = generateInitialPopulation(
    elements=elements,
    population_size=50, # 50
    calculator=calculator,
    volume=initial_volume*Angstrom**3,
    max_forces=0.01*eV/Angstrom,
    max_stress=0.1*GPa,
    max_steps=1000, # 1000
    max_step_length=0.2*Angstrom,
    external_pressure=0.0*GPa,
    rng=rng,
    log_filename_prefix=population_filename,
    )

# ------------------------------------------------------------
# Crystal Structure Prediction
# ------------------------------------------------------------

crystal_structure_prediction = CrystalStructurePrediction(
    initial_population,
    number_of_generations=10, #10
    selection_pressure=2.0,
    number_of_elites=50, # 50
    number_to_promote=20, # 20
    heredity_probability=50.0,
    permutation_probability=20.0,
    mutation_probability=30.0,
```

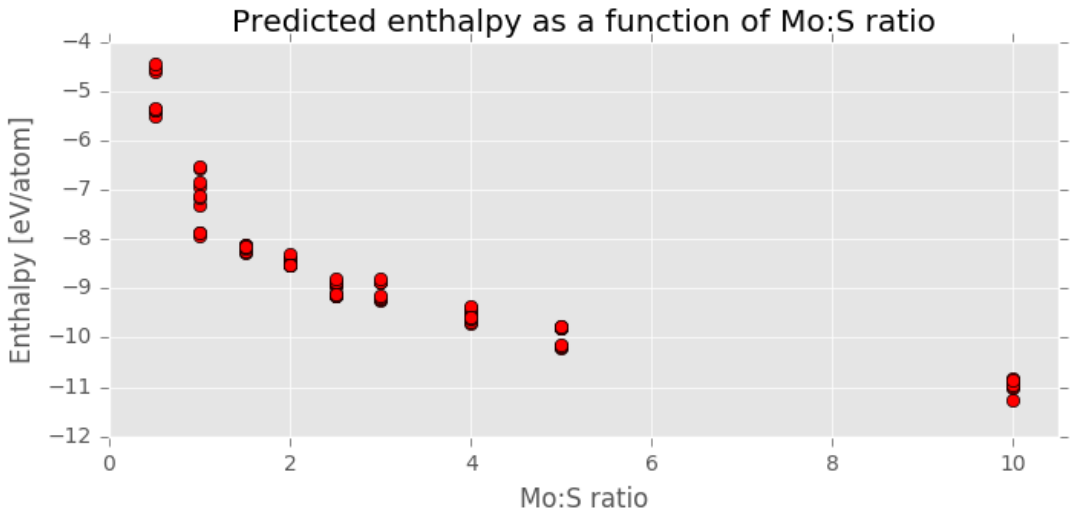

Figure 51: Unit cell enthalpy as a function of Mo:S ratio. Lower enthalpy indicates increased stability. Results obtained by Virtual NanoLab's Crystal Structure Prediction genetic algorithm [7].

```
        sigma_lattice=0.7,
        max_forces=0.01*eV/Angstrom,
        max_stress=0.1*GPa,
        max_steps=1000, #1000
        max_step_length=0.2*Angstrom,
        external_pressure=0.0*GPa,
        rng=rng,
        write_population=True,
        log_filename_prefix=generation_filename,
        )
    first_few_fitnesses = -np.array(crystal_structure_prediction.fitnesses()[0:5])/
                          num_of_atoms_in_unit_cell
    fitness.extend(first_few_fitnesses.tolist())
    ratio.extend([float(nMo)/float(nS)]*len(first_few_fitnesses))
```

B.2 Results

The enthalpies of the top 5 structures with the highest fitness (lowest enthalpy) for each formula were plotted against Mo:S ratio. An obvious trend of increased stability with increased Mo:S ratio was observed.

C Mesh analysis for a network of tiled resistors

A network of $N_i \times N_j$ resistors is solved using mesh analysis, where i is in the direction of the channel width W and j is in the direction of channel length L (Figure 30b). Resistors are placed between each two nearest-neighbour nodes, namely between (i,j) and $(i \pm 1, j)$, and between (i,j) and $(i, j \pm 1)$.

The various contact resistances to the left and right electrodes are modelled by the following set of resistors:

$$\begin{cases} R_{C,\text{Left},i} = R_{\text{SL}}^{i,1} \equiv R_{i,0}^{i,1} \\ R_{C,\text{Right},i} = R_{\text{SR}}^{i,N_j} \equiv R_{i,N_j}^{i,N_j+1} \end{cases}, \quad \forall i \in [1, N_i] \tag{24}$$

and the resistance between each two nearest-neighbour nodes $[(i,j),(i \pm 1, j)]$ and $[(i,j),(i, j \pm 1)]$ is modelled by the following set of resistors:

$$\begin{cases} R_{i,j}^{i+1,j} \equiv R_{i+1,j}^{i,j} \\ R_{i,j}^{i,j+1} \equiv R_{i,j+1}^{i,j} \end{cases}. \tag{25}$$

The set of equations used to solve the resistor network using mesh analysis are given in Table 10.

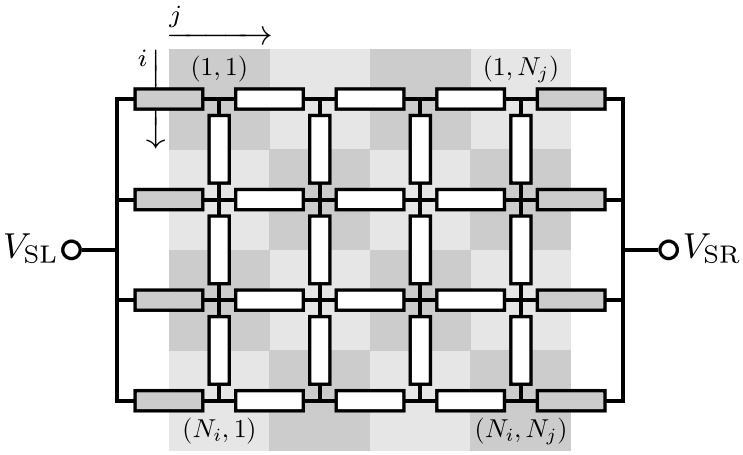

(a) Diagram of the resistor network.

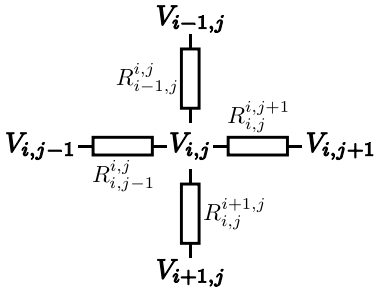

(b) Nearest-neighbour stencil.

Figure 52: Nomenclature of the resistor network (a) and the stencil used to solve the resistor network (b).

Table 10: The set of equation used to construct the linear system of equations for a network of tiled resistors, obtained from mesh analysis (model and stencil presented in Figure 30b).

Node	Original equation (KCL)
(i,j)	$\frac{V_{i,j}-V_{i,j-1}}{R^{i,j}_{i,j-1}} = -\frac{V_{i,j}-V_{i-1,j}}{R^{i,j}_{i-1,j}} + \frac{V_{i,j+1}-V_{i,j}}{R^{i,j+1}_{i,j}} + \frac{V_{i+1,j}-V_{i,j}}{R^{i+1,j}_{i,j}}$
$(1,1)$	$\frac{V_{1,1}-V_{\mathrm{SL}}}{R^{1,1}_{1,0}} = \frac{V_{1,2}-V_{1,1}}{R^{1,2}_{1,1}} + \frac{V_{2,1}-V_{1,1}}{R^{2,1}_{1,1}}$
$(1,N_j)$	$\frac{V_{1,N_j}-V_{1,N_j-1}}{R^{1,N_j}_{1,N_j-1}} = \frac{V_{\mathrm{SR}}-V_{1,N_j}}{R^{1,N_j+1}_{1.N_j}} + \frac{V_{2,N_j}-V_{1,N_j}}{R^{2,N_j}_{1,N_j}}$
$(N_i,1)$	$\frac{V_{N_i1}-V_{\mathrm{SL}}}{R^{N_i,1}_{N_i0}} = -\frac{V_{N_i,1}-V_{N_i-1,1}}{R^{N_i,1}_{N_i-1,1}} + \frac{V_{N_i,2}-V_{N_i,1}}{R^{N_i,2}_{N_i.1}}$
(N_i,N_j)	$\frac{V_{N_i,N_j}-V_{N_i,N_j-1}}{R^{N_i,N_j}_{N_i,N_j-1}} = -\frac{V_{N_i,N_j}-V_{N_i-1,N_j}}{R^{N_i,N_j}_{N_i-1,N_j}} + \frac{V_{\mathrm{SR}}-V_{N_i,N_j}}{R^{N_i,N_j+1}_{N_i.N_j}}$
$(1,j)$	$\frac{V_{1,j}-V_{1,j-1}}{R^{1,j}_{1,j-1}} = \frac{V_{1,j+1}-V_{1,j}}{R^{1,j+1}_{1,j}} + \frac{V_{2,j}-V_{1,j}}{R^{2,j}_{1,j}}$
(N_i,j)	$\frac{V_{N_i,j}-V_{N_i,j-1}}{R^{N_i,j}_{N_i,j-1}} = -\frac{V_{N_i,j}-V_{N_i-1,j}}{R^{N_i,j}_{N_i-1,j}} + \frac{V_{N_i,j+1}-V_{N_i,j}}{R^{N_i,j+1}_{N_i.j}}$
$(i,1)$	$\frac{V_{i,1}-V_{\mathrm{SL}}}{R^{i,1}_{i,0}} = -\frac{V_{i,1}-V_{i-1,1}}{R^{i,1}_{i-1,1}} + \frac{V_{i,2}-V_{i,1}}{R^{i,2}_{i.1}} + \frac{V_{i+1,1}-V_{i,1}}{R^{i+1,1}_{i,1}}$
(i,N_j)	$\frac{V_{i,N_j}-V_{i,N_j-1}}{R^{i,N_j}_{i,N_j-1}} = -\frac{V_{i,N_j}-V_{i-1,N_j}}{R^{i,N_j}_{i-1,N_j}} + \frac{V_{\mathrm{SR}}-V_{i,N_j}}{R^{i,N_j+1}_{i.N_j}} + \frac{V_{i+1,N_j}-V_{i,N_j}}{R^{i+1,N_j}_{i,N_j}}$

(a) Original equation (KCL)

	By nodes (for matrix notation)					
Node	C	W	N	E	S	RHS
(i,j)	$V_{i,j}\left(\frac{1}{R^{i,j}_{i,j-1}} + \frac{1}{R^{i,j}_{i-1,j}} + \frac{1}{R^{i,j+1}_{i,j}} + \frac{1}{R^{i+1,j}_{i,j}}\right)$	$-\frac{V_{i,j-1}}{R^{i,j}_{i,j-1}}$	$-\frac{V_{i-1,j}}{R^{i,j}_{i-1,j}}$	$-\frac{V_{i,j+1}}{R^{i,j+1}_{i,j}}$	$-\frac{V_{i+1,j}}{R^{i+1,j}_{i,j}}$	0
$(1,1)$	$V_{1,1}\left(\frac{1}{R^{1,1}_{1,0}} + \frac{1}{R^{1,2}_{1,1}} + \frac{1}{R^{2,1}_{1,1}}\right)$			$-\frac{V_{1,2}}{R^{1,2}_{1,1}}$	$-\frac{V_{2,1}}{R^{2,1}_{1,1}}$	$\frac{V_{\mathrm{SL}}}{R^{1,1}_{1,0}}$
$(1,N_j)$	$V_{1,N_j}\left(\frac{1}{R^{1,N_j}_{1,N_j-1}} + \frac{1}{R^{1,N_j+1}_{1.N_j}} + \frac{1}{R^{2,N_j}_{1,N_j}}\right)$	$-\frac{V_{1,N_j-1}}{R^{1,N_j}_{1,N_j-1}}$			$-\frac{V_{2,N_j}}{R^{2,N_j}_{1,N_j}}$	$\frac{V_{\mathrm{SR}}}{R^{1,N_j+1}_{1.N_j}}$
$(N_i,1)$	$V_{N_i,1}\left(\frac{1}{R^{N_i,1}_{N_i0}} + \frac{1}{R^{N_i,1}_{N_i-1,1}} + \frac{1}{R^{N_i,2}_{N_i.1}}\right)$		$-\frac{V_{N_i-1,1}}{R^{N_i,1}_{N_i-1,1}}$	$-\frac{V_{N_i,2}}{R^{N_i,2}_{N_i,1}}$		$\frac{V_{\mathrm{SL}}}{R^{N_i,1}_{N_i,0}}$
(N_i,N_j)	$V_{N_i,N_j}\left(\frac{1}{R^{N_i,N_j}_{N_i,N_j-1}} + \frac{1}{R^{N_i,N_j}_{N_i-1,N_j}} + \frac{1}{R^{N_i,N_j+1}_{N_i.N_j}}\right)$	$-\frac{V_{N_i,N_j-1}}{R^{N_i,N_j}_{N_i,N_j-1}}$	$-\frac{V_{N_i-1,N_j}}{R^{N_i,N_j}_{N_i-1,N_j}}$			$\frac{V_{\mathrm{SR}}}{R^{N_i,N_j+1}_{N_i.N_j}}$
$(1,j)$	$V_{1,j}\left(\frac{1}{R^{1,j}_{1,j-1}} + \frac{1}{R^{1,j+1}_{1,j}} + \frac{1}{R^{2,j}_{1,j}}\right)$	$-\frac{V_{1,j-1}}{R^{1,j}_{1,j-1}}$		$-\frac{V_{1,j+1}}{R^{1,j+1}_{1,j}}$	$-\frac{V_{2,j}}{R^{2,j}_{1,j}}$	0
(N_i,j)	$V_{N_i,j}\left(\frac{1}{R^{N_i,j}_{N_i,j-1}} + \frac{1}{R^{N_i,j}_{N_i-1,j}} + \frac{1}{R^{N_i,j+1}_{N_i.j}}\right)$	$-\frac{V_{N_i,j-1}}{R^{N_i,j}_{N_i,j-1}}$	$-\frac{V_{N_i-1,j}}{R^{N_i,j}_{N_i-1,j}}$	$-\frac{V_{N_i,j+1}}{R^{N_i,j+1}_{N_i.j}}$		0
$(i,1)$	$V_{i,j}\left(\frac{1}{R^{i,1}_{i,0}} + \frac{1}{R^{i,1}_{i-1,1}} + \frac{1}{R^{i,2}_{i.1}} + \frac{1}{R^{i+1,1}_{i,1}}\right)$		$-\frac{V_{i-1,1}}{R^{i,1}_{i-1,1}}$	$-\frac{V_{i,2}}{R^{i,2}_{i.1}}$	$-\frac{V_{i+1,1}}{R^{i+1,1}_{i,1}}$	$\frac{V_{\mathrm{SL}}}{R^{i,1}_{i,0}}$
(i,N_j)	$V_{i,N_j}\left(\frac{1}{R^{i,N_j}_{i,N_j-1}} + \frac{1}{R^{i,N_j}_{i-1,N_j}} + \frac{1}{R^{i,N_j+1}_{i.N_j}} + \frac{1}{R^{i+1,N_j}_{i,N_j}}\right)$	$-\frac{V_{i,N_j-1}}{R^{i,N_j}_{i,N_j-1}}$	$-\frac{V_{i-1,N_j}}{R^{i,N_j}_{i-1,N_j}}$		$-\frac{V_{i+1,N_j}}{R^{i+1,N_j}_{i,N_j}}$	$\frac{V_{\mathrm{SR}}}{R^{i,N_j+1}_{i.N_j}}$

(b) By nodes (for matrix notation)